

Surface Hopping Dynamics with Correlated Single-Reference Methods: 9H-Adenine as a Case Study

Felix Plasser,^{*,†} Rachel Crespo-Otero,^{‡,○} Marek Pederzoli,[§] Jiri Pittner,[§] Hans Lischka,^{∇,⊥} and Mario Barbatti^{*,‡}

[†]Interdisciplinary Center for Scientific Computing, Ruprecht-Karls-University, Im Neuenheimer Feld 368, 69120 Heidelberg, Germany

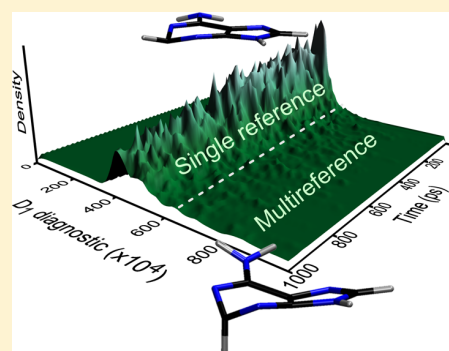
[‡]Max-Planck-Institut für Kohlenforschung, Kaiser-Wilhelm-Platz 1, D-45470 Mülheim an der Ruhr, Germany

[§]J. Heyrovský Institute of Physical Chemistry, Academy of Sciences of the Czech Republic, v.v.i., Dolejškova 3, 18223 Prague 8, Czech Republic

[∇]Department of Chemistry and Biochemistry, Texas Tech University, Lubbock, Texas 79409-1061, United States

[⊥]Institute for Theoretical Chemistry, University of Vienna, Währingerstr. 17, A-1090 Vienna, Austria

ABSTRACT: Surface hopping dynamics methods using the coupled cluster to approximated second order (CC2), the algebraic diagrammatic construction scheme to second order (ADC(2)), and the time-dependent density functional theory (TDDFT) were developed and implemented into the program system Newton-X. These procedures are especially well-suited to simulate nonadiabatic processes involving various excited states of the same multiplicity and the dynamics in the first excited state toward an energetic minimum or up to the region where a crossing with the ground state is found. 9H-adenine in the gas phase was selected as the test case. The results showed that dynamics with ADC(2) is very stable, whereas CC2 dynamics fails within 100 fs, because of numerical instabilities present in the case of quasi-degenerate excited states. ADC(2) dynamics correctly predicts the ultrafast character of the deactivation process. It predicts that C2-puckered conical intersections should be the preferential pathway for internal conversion for low-energy excitation. C6-puckered conical intersection also contributes appreciably to internal conversion, becoming as important as C2-puckered for high-energy excitations. In any case, H-elimination plays only a minor role. TDDFT based on a long-range corrected functional fails to predict the ultrafast deactivation. In the comparison with several other methods previously used for dynamics simulations of adenine, ADC(2) has the best performance, providing the most consistent results so far.



1. INTRODUCTION

Nonadiabatic dynamics has become a central method for the prediction of excited-state properties and the assignment of features in time-resolved spectra. However, the large computational cost of such simulations has led to the development of semiclassical independent-trajectory methods such as surface hopping,¹ as well as to the reduction of statistical ensembles² and the use of cost-effective low-level electronic structure methods.³

For many problems in photochemistry and photophysics, temporal evolution involves nonadiabatic relaxation through the manifold of excited electronic states of the same multiplicity until the minimum of the first excited state is reached (Kasha's rule) or until a region of crossing to the ground state of that multiplicity is found. For this early dynamics, static electron correlation of the ground state is often of minor importance for the description of the potential energy surfaces, compared with dynamic electron correlation. This motivates the search for single-reference methods that can be efficiently coupled to on-the-fly schemes for dynamics simulations. Time-dependent

density functional theory (TDDFT) has been the method of choice for several groups recently,⁴ and many successful cases have been published.^{4c} (For a critical review on the applicability of different methods, see ref 3.) Sharing this motivation, in this work, we report the implementation of surface hopping dynamics based on different single-reference electronic structure methods. Specifically, we consider the second-order approximate coupled cluster (CC2)⁵ and the algebraic diagrammatic construction to second order (ADC(2))⁶ methods, which, in combination with the resolution of the identity (RI) approximation, can provide accurate potential energy surfaces at a computational cost that is feasible for on-the-fly dynamics simulations. While these two methods are very similar, from a methodological point of view, ADC(2) possesses the distinct advantage of being derived from a Hermitian eigenvalue problem, which increases the numerical stability of this method in the case of quasi-degenerate excited

Received: December 27, 2013

Published: February 28, 2014

states, as well as generally reducing the computational effort required for the computation of molecular properties and gradients. Surface hopping dynamics with CC2 and ADC(2) was implemented in an interface between the Netwon-X⁷ and Turbomole⁸ programs. In addition, we also present a new interface between Newton-X and Gaussian 09,⁹ which extends the range of methods available to surface hopping dynamics to TDDFT with long-range corrected functionals¹⁰ and Tamm-Dancoff approximation (TDA)¹¹ based either on restricted or unrestricted DFT.

Analytic nonadiabatic coupling vectors at the CC level have been considered only rarely in the literature,¹² and no implementation for either CC2 or ADC(2) is available. For this reason, and for the purpose of computational efficiency, we follow a different approach based on wave function overlaps of approximate configuration interaction with single excitations (CIS) wave functions. These overlaps may be used subsequently in connection with two algorithms for the propagation of the wave function: the standard adiabatic one,¹³ and a locally-diabatic approach,¹⁴ which was shown to be particularly stable in the case of highly peaked nonadiabatic couplings.¹⁵ The procedures developed here certainly follow a pragmatic strategy, which, however, is expected to provide good results in cases where the ground-state wave function is well-described by a single determinant and the excited states by single excitations. In such circumstances, the changes in the character of the electronic wave function and nonadiabatic interactions will be computed fairly well. It should be kept in mind, at this point, that computational efficiency is a major criterion since, in the on-the-fly approach of surface hopping, excited-state energies and nonadiabatic interactions must be computed at each time step, leading to an extremely large computational effort.

We selected 9H-adenine in the gas phase to test these implementations. The advantage of working with this molecule for testing new methods is that results from dynamics simulations at several theoretical levels are available, including ab initio¹⁶ and semiempirical¹⁷ multireference configuration interaction (MRCI), semiempirical configuration interaction (CI) with floating-occupation molecular orbitals,¹⁸ TDDFT with several functionals,^{3,19} and time-dependent density functional tight binding (TD-DFTB).²⁰ Diverse dynamics methods have been used as well, including not only surface hopping,^{3,16–18,20b} but also Ehrenfest dynamics^{20a} and quantum wavepacket propagation.¹⁹ Moreover, several experimental time-resolved spectra are also available in the gas phase.²¹

There is still another reason that makes it interesting to readdress the dynamics of 9H-adenine in the gas phase: although there is no doubt that 9H-adenine excited at the maximum of the first band returns to the ground state via internal conversion within ~ 1 ps, there is no agreement about which reaction pathway is used. Simulations based on ab initio methods predicted that internal conversion occurs in a region of the seam of conical intersections characterized by puckering of the pyrimidine ring at the C2 atom (Figure 1).¹⁶ However, other simulations based on semiempirical methods predicted that internal conversion happens at a C6-puckered region of the crossing seam.^{17,18} Finally, other authors have suggested that the experiments indicate that H elimination from a NH bond is the actual way for internal conversion, even at low excitation energies.^{21d}

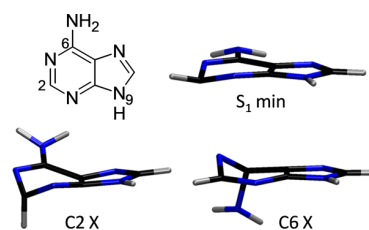


Figure 1. 9H-adenine structures of the S_1 minimum and of the C2 and C6 S_1/S_0 conical intersections (X).

2. COMPUTATIONAL DETAILS

Nonadiabatic dynamics was simulated with the fewest-switches surface hopping^{1b} corrected for decoherence effects ($\alpha = 0.1$ hartree).²² Trajectories ran for a maximum of 1000 fs or until a S_1-S_0 energy gap smaller than 0.1 eV was reached. Integration was done with a time step of 0.5 fs for the classical equations and a time step of 0.025 fs for the quantum equations, using interpolated quantities between classical steps. The number of trajectories and the initial states are discussed later.

Electronic structure calculations were performed with CC2,⁵ ADC(2),⁶ and TDDFT.²³ CC2 is a simplification of the coupled-cluster singles and doubles (CCSD), which truncates the doubles equations such that excitation energies of singly excited states remain correct through second order in the fluctuation potential. Replacing double substitution amplitudes in the CC2 Jacobian \mathbf{A}^{CC2} (a matrix in the space of single and double orbital substitutions) by their first-order approximations produces the Jacobian of the CIS(D_∞) approximation.²⁴ The ADC(2) method, which was originally derived using diagrammatic perturbation theory,^{6a} may be expressed by the symmetric Jacobian $\mathbf{A}^{\text{ADC}(2)} = 1/2(\mathbf{A}^{\text{CIS}(D_\infty)} + \mathbf{A}^{\text{CIS}(D_\infty)\dagger})$ where \dagger indicates the conjugate transpose of \mathbf{A} . Excited-state energies of either of these approximations correspond to the eigenvalues of the respective Jacobian, while the contribution of each determinant to the excitation is associated to the eigenvectors.

Nonadiabatic interactions are computed during the dynamics by considering the numerical approximation proposed by Hammes-Schiffer and Tully.¹³ In this approach, the inner product between the nonadiabatic coupling \mathbf{F}_{kl} and the classical velocity \mathbf{v} (both vectors in nuclear coordinate space) computed at time t is given by¹⁵

$$\mathbf{F}_{kl} \cdot \mathbf{v} \approx \frac{1}{4\Delta t} [3S_{kl}(t) - 3S_{lk}(t) - S_{kl}(t - \Delta t) + S_{lk}(t - \Delta t)] \quad (1)$$

where $S_{kl}(t)$ is the overlap integral of electronic wave functions ϕ_n for states k and l ,

$$S_{kl}(t) = \langle \phi_k(t - \Delta t) | \phi_l(t) \rangle \quad (2)$$

and Δt is the integration time step. For TDDFT, this approximation has been successfully applied by several authors.²⁵ The wave function is written as a formal configuration interaction with single excitations (CIS) wave function:²⁶

$$|\phi_n\rangle = \sum_{ia} \sqrt{\frac{\epsilon_i - \epsilon_a}{E_n}} X_{ia}^n |\Phi_{ia}\rangle \quad (3)$$

where $|\Phi_{ia}\rangle$ is a Slater determinant corresponding to an excitation from Kohn–Sham orbitals i to a with corresponding orbital energies ϵ_i and ϵ_a . E_n is the excitation energy for state n .

Table 1. Characterization of the First Absorption Band of 9H-Adenine

	RI-CC2		RI-ADC(2)		TD- ω B97XD		Experiment ^a	
	ΔE (eV)	f	ΔE (eV)	f	ΔE (eV)	f	ΔE (eV)	f
$n-\pi^*$	5.08	0.021	5.00	0.026	5.33	0.001		
$\pi-\pi^*$	5.13	-0.034	5.06	0.169	5.33	0.280	5.16 ± 0.07^b	0.24 ^c
$\pi-\pi^*$	5.16	0.300	5.07	0.101	5.46	0.012		
$\pi-3s$	5.39	0.013	5.39	0.010	5.88	0.006		
band maximum	4.95		4.87		5.09		$5.07,^d 4.92^c$	
fw $_{\text{hm}}/\sigma^{\text{maxe}}$	0.57	0.534	0.62	0.497	0.59	0.501	0.55 ^e	0.463 ^c

^aExperimental results obtained in vapor. ^bData taken from ref 32. ^cData taken from ref 33a. ^dData taken from ref 33b. ^efw $_{\text{hm}}$ represents the full width at half maximum; σ^{max} is defined as the maximum of the absorption cross section (in $\text{\AA}^2 \text{ molecule}^{-1}$).

X_{ia}^n is the time-dependent linear-response pseudo-eigenvector for the same determinant for state n . In the construction of the wave function, the Y_{ia}^n components of the pseudo-eigenvector are neglected and X_{ia}^n are orthogonalized, implying that the nonadiabatic couplings are computed within an approach equivalent to the Tamm–Dancoff approximation.

Similarly, for CC2, an approximate wave function is constructed as

$$|\phi_n\rangle = \sum_{ia} R_{ia}^n |\Phi_{ia}\rangle \quad (4)$$

$$\langle \phi_n | = \sum_{ia} L_{ia}^n \langle \Phi_{ia} | \quad (5)$$

where R_{ia}^n and L_{ia}^n are the single substitution parts of the right and left Jacobian eigenvectors. For ADC(2), the same expression is used with $L_{ia}^n = R_{ia}^n$. From these CIS wave functions built at two sequential time steps, the wave function overlaps (eq 2) are computed as described in refs 25c and 27.

To arrive at eqs 4 and 5, several approximations that rely on the predominance of single excitations in the wave function are introduced. These approximations allow for an efficient computation of the overlap matrix elements. First, doubles amplitudes are neglected, because they are never explicitly stored in the Turbomole implementation^{5b} of CC2 and ADC(2), which exploits the diagonality of the double/double blocks of the Jacobian to reformulate the eigenvalue problem in the single-substitution space only. For simplicity reasons, the singles amplitudes are used to construct a formal CIS wave function, rather than an actual CC wave function. Per default, these truncated wave functions are reorthonormalized (see ref 12c with regard to challenges in normalizing the original CC wave functions). In addition, in the case of CC2, where right and left eigenvectors are different (forming a biorthogonal system) due to the nonsymmetry of the Jacobian, we compute the overlap of the right vectors of the respective current time step with the left vectors from the previous one. These approximations allow us to compute the overlaps at a reasonable effort (~20% of the total computation time for one single step). By contrast, one would expect the exact overlaps of CC wave functions to scale exponentially with system size, and, to our knowledge, such calculations have never been attempted.

A ground-state harmonic-oscillator Wigner distribution for the nuclei was used to simulate the absorption spectrum with the Nuclear Ensemble (NE) approach.²⁸ The parameters for the spectrum simulations were $N_p = 500$ (number of ensemble points), $N_{\text{fs}} = 6$ (number of excited states), and $\delta = 0.1$ eV (Gaussian line broadening). Initial conditions for dynamics

were obtained from the absorption spectrum in restricted spectral domains, as explained later in section 3.2.

Turbomole was used for CC2 and ADC(2) calculations, and Gaussian 09 was used for TDDFT. Newton-X interfaced to these programs was used for dynamics simulations. In the cases of TDDFT, trajectories were computed with the long-range and dispersion corrected ω B97XD functional.^{10,29} To the best of our knowledge, this is the first study using long-range corrected functionals in combination with surface hopping dynamics. The aug-cc-pVDZ basis set³⁰ was adopted for all calculations.

For comparison, nonadiabatic coupling vectors were computed at the multireference configuration interaction level with single excitations (MR-CIS) using the aug-cc-pVDZ basis set, based on a complete active reference space of 10 electrons in 8 orbitals (3π , $2n$, $3\pi^*$). These orbitals were generated using a complete active space self-consistent field calculation in the same active space. These computations were performed with the Columbus program package.³¹

3. RESULTS

3.1. Vertical Excitations and S_1 Minimum. The vertical excitation energies into the lowest singlet states of 9H-adenine are given in Table 1. The lowest excitation is into the $n-\pi^*$ state, which is closely followed by two $\pi-\pi^*$ states and then by the Rydberg $\pi-3s$. The experimental value for the vertical excitation was proposed in ref 32, based on vapor spectra of adenine reported in ref 33. It was estimated by adding the deviation between the computed vertical excitation and the simulated band maximum to the experimental band maximum.³² The comparison of the computational values with the experimental result for the $\pi-\pi^*$ states is excellent for all methods. The CC2 energies fall within the experimental error bar, while the ADC(2) result is lower than the experiment by 0.1 eV. CC2 results with aug-cc-pVTZ basis set reported in ref 34 are ~0.1 eV larger than those in Table 1. It may also be noted that the hierarchically superior EOM-CCSD(T) method puts the dark $n-\pi^*$ states somewhat above the $\pi-\pi^*$ states, changing the state ordering.³⁵ With TDDFT, the vertical excitations of adenine are rather sensitive to the functional, as we have discussed previously.³ Specifically, for ω B97XD, the vertical excitation energy is 0.17 eV higher than the experimental value. For all methods, there are substantial Rydberg contributions to the $\pi-\pi^*$ states. The combined oscillator strengths of the $\pi-\pi^*$ states are slightly larger than the experimental value. The negative oscillator strength in CC2 reflects the imaginary root arising from the quasi-degeneracy of the states.³⁴

Because of the close energy spacing between the $\pi-\pi^*$ states, mixing between them is quite strong, resulting in significant

discrepancies for the oscillator strengths of the adiabatic S_1 and S_2 states between the different methods presented in Table 1. For comparison to the experiments, however, the quantity that matters is the total oscillator strength of the two $\pi-\pi^*$ states, rather than their individual values. Furthermore, these values are also strongly geometry-dependent. These conditions pose challenges for a proper choice of initial states. Our solution to this problem is described in section 3.2: the initial state is probabilistically chosen according to the oscillator strength at the respective geometry. In other words, the states with strong oscillator strengths are chosen irrespective of the adiabatic ordering.

CC2 and ADC(2) predict the S_1 minimum of adenine with an envelope conformation (2E) puckered at C2 (Figure 1). The minimum is of $n-\pi^*$ nature, but is strongly mixed with $\pi-\pi^*$ character. According to the experiments conducted in water,³⁶ the weak luminescence of adenine (quantum yield 2.6×10^{-4}) is peaked at 3.86 eV with a shoulder at 3.00 eV. Our investigations in the gas phase did not show any evidence of an energy minimum with a gap as large as 3.86 eV to the ground state. However, both methods show the existence of a flat region on the S_1 surface ($n-\pi^*$) with a barrierless connection to the S_1 minimum (see also ref 37). This flat region corresponds to planar geometries, and it is 3.7 eV (3.6 eV) above the ground state, according to CC2 (ADC(2)). This could imply that either CC2 and ADC(2) do not properly describe a small barrier separating the flat region from the puckered minimum or that this small barrier is ultimately caused by interaction of 9H-adenine with water. In any case, the correspondence between CC2 and ADC(2) emission energies (3.10 and 2.96 eV, Table 2) and the experimental shoulder at

Table 2. Characterization of the S_1 Minimum Optimized with CC2, ADC(2), and TD- ω B97XD (aug-cc-pVDZ) in Terms of the Vertical Excitation Energy (ΔE), Adiabatic Excitation Energy (ΔE_a), and Cremer–Pople Parameters

	CC2	ADC(2)	TD- ω B97XD	experiment
ΔE (eV)	3.10	2.96	3.98	3.86, 3.00 ^a
ΔE_a (eV)	4.42	4.29	4.68	4.40–4.47 ^b
ϕ (°)	246	246		
θ (°)	121	121		
Q (Å)	0.26	0.27	0.00	
Conform.	2E	2E	planar	

^aFluorescence band maximum and shoulder in water (pH 7.3); data taken from ref 36. ^bR2PI band origin (gas phase); data taken from ref 38.

3.00 eV is once more remarkable. The adiabatic excitation energy is 4.42 eV at CC2 and 4.29 eV at ADC(2). These values are also in good agreement with the resonant two-photon ionization (R2PI) measurements of adenine vapor, which established the band origin to be in the 4.40–4.47 eV region.³⁸ In comparison, CASSCF optimization of 9H-adenine shows two minima: one planar and one puckered.³⁹ The energy barrier connecting them (starting from the highest minimum) is only 0.12 eV at CASPT2 level, using the CASSCF geometries. It is not clear at this point whether the inclusion of dynamic electron correlation in the optimization would eliminate or enhance this barrier.

TD- ω B97XD predicts the existence of a planar S_1 minimum with $n-\pi^*$ character and an emission energy of 3.98 eV. Every attempt of optimizing a puckered minimum ends up back at

that planar minimum. This situation is similar to that observed with other functionals³ and, curiously, it is exactly the opposite of the CC2 and ADC(2) results discussed above, where a puckered minimum was found, but not a planar one.

3.2. Absorption Spectrum and Initial Conditions. The absorption spectrum of 9H-adenine was simulated using the NE approach, which provides intensities and band widths in absolute units (although without vibrational resolution).²⁸ The results are shown in the top portion of Figure 2, together with

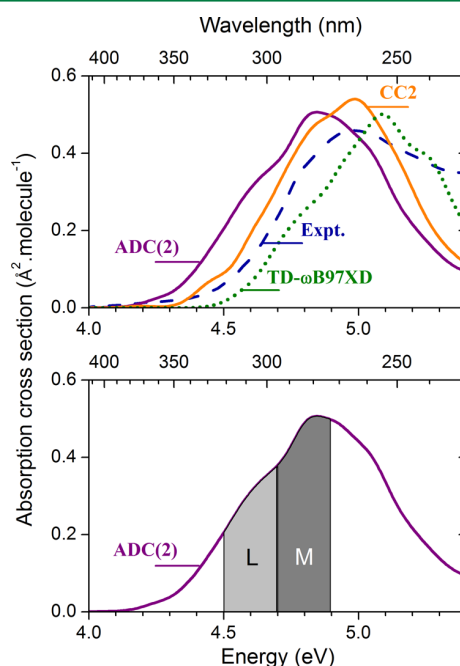


Figure 2. Absorption spectrum of 9H-adenine. Top panel shows results for CC2, ADC(2) and TD- ω B97XD simulations (experimental results obtained in vapor).^{33a} Bottom panel presents the ADC(2) spectrum, showing the L (4.6 ± 0.1 eV) and M (4.8 ± 0.1 eV) domains from where initial conditions for dynamics were selected.

the experimental results from ref 33a (see ref 40, too). The CC2 band maximum (4.95 eV, Table 1) is in excellent agreement with the vapor spectrum measured by Clark et al.^{33a} (4.92 eV). The ADC(2) maximum (4.87 eV) is slightly red-shifted, when the same experiments are compared to each other. The TD- ω B97XD maximum is blue-shifted by 0.17 eV, which, remarkably, is the same shift observed in the vertical excitation. The experimental and simulated full widths at the half-maximum (fwhm) agree within 0.05 eV. The simulated maximum of the absorption cross section is larger than the experimental measurement by $0.07 \text{ \AA}^2 \text{ molecule}^{-1}$ for CC2, $0.03 \text{ \AA}^2 \text{ molecule}^{-1}$ for ADC(2), and $0.04 \text{ \AA}^2 \text{ molecule}^{-1}$ for TD- ω B97XD (see Table 1).

For ADC(2), initial conditions for dynamics were sampled from two domains in the simulated spectra: L (low) and M (medium). The L-domain is defined as residing in the 4.6 ± 0.1 eV range, whereas the M-domain is defined as residing in the 4.8 ± 0.1 eV range (bottom panel of Figure 2). From the initial $N_p \times N_v = 500 \times 6 = 3000$ spectral points used to build the spectrum, 218 points are in the L-domain and 407 points are in the M-domain. Each point corresponds to a set of random nuclear geometry and velocity given by the Wigner distribution. The M-domain was selected to approximately emulate the

experimental pump at 251.3 nm (4.93 eV),^{21e} corresponding to the band maximum. The L-domain was selected to emulate the pump at 265.1 nm (4.68 eV),^{21e} which is the middle of the low-energy side of the absorption band.

To select initial conditions from each of these domains, the photoexcitation probability is computed for each point in the domain. This probability is given by the oscillator strength of the point normalized by the maximum oscillator strength in the ensemble. Then, a stochastic algorithm selects points within the domain according to this probability. After this screening, 61 points were selected in the L-domain (Table 3): 45 correspond

Table 3. Number of Spectral Points and of Initial Conditions in the L- and M-Domains for ADC(2) Simulations

domain (eV)		S ₁	S ₂	S ₃	S ₄	total
4.6 ± 0.1 (L)	spectrum	45	13	3	0	61
	trajectories	38	12	0	0	50
4.8 ± 0.1 (M)	spectrum	34	75	10	1	120
	trajectories	14	32	4	0	50

to excitations into S₁, 13 into S₂, and 3 into S₃. As we limited our simulations to 50 trajectories in each domain, to keep the same proportion of points being excited into each state, 38 trajectories were started in S₁, 12 in S₂ state and none in S₃. With the same selection procedure for the M-domain, we started 14 trajectories in S₁, 32 in S₂, and 4 in S₃.

3.3. Dynamics. 3.3.1. *Suitability of ADC(2) and CC2 for Dynamics.* Dynamics with CC2 was tested with a set of 10 trajectories initiated in the 4.7 ± 0.1 eV domain. All of them failed due to numerical problems within the first 100 fs. This happened because of the nonsymmetric CC2 Jacobian, which

tends to produce imaginary eigenvalues (energies) near degenerated excited states.²⁴

ADC(2) does not show this problem because it has a symmetric Jacobian, whose eigenvalues are always strictly real. Dynamics with this method was perfectly stable and trajectories ran until one of the termination criteria was achieved. In terms of computational time, 2000 steps for 1 ps trajectory computed with RI-ADC(2)/aug-cc-pVDZ, 3 excited states, required ~24 days running on 4 cores of a 2.7 GHz Xeon processor. This computational demand may, in principle, be alleviated by restricting the virtual space as discussed in ref 41, but this feature was not tested in this work.

The reliability of ADC(2) calculations may be estimated by computing the D_1 and D_2 diagnostics.⁴² The D_1 diagnostic^{42a} measures the interaction between the Hartree–Fock (HF) reference state and singly-excited determinants. High D_1 values indicate multireference character of the ground state. The D_2 diagnostic^{42b} measures the interaction between the HF reference and doubly-excited determinants, thus, high values indicate large contributions of double excitations for the excited state in question.

The initially recommended values for D_1 (MP2) and D_2 (CCSD) are $D_1 < 0.04$ and $D_2 < 0.17$.⁴² Even though adenine has D_1 (MP2) and D_2 (ADC(2)) above the recommended thresholds already in the ground-state minimum (0.042 and 0.26, respectively), all our tests indicated that ADC(2) provides a good description of the lowest electronic states of adenine. This seems to imply that the recommended values, obtained for MP2 and CCSD ground-state calculations on a benchmark of small molecules (no aromatic systems included), establish a safety margin that is too narrow to account for molecules such as 9H-adenine. In fact, based on the evaluation of excited states computed with CC2 for a set of

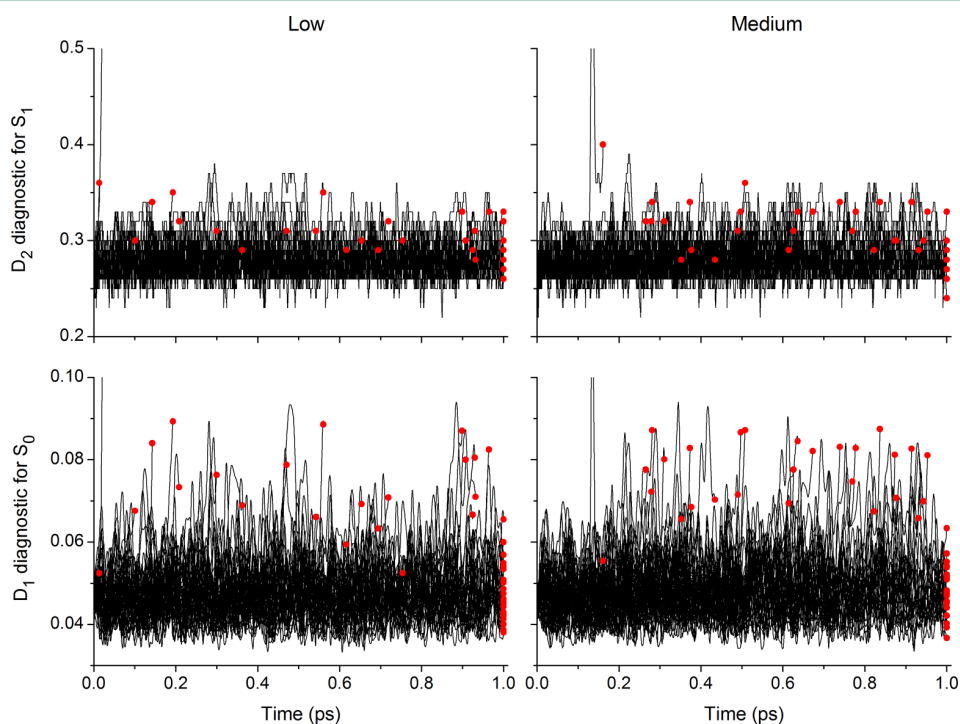


Figure 3. D_1 (MP2) diagnostic for the ground state and D_2 (ADC(2)) diagnostic for S₁ along the dynamics. Dots indicate the values at the last point of each trajectory.

molecules, Köhn and Hättig concluded that D_1 values up to 0.15 and D_2 values up to 0.25 are still acceptable.⁴³

D_1 (MP2) and D_2 (ADC(2)) diagnostics along the dynamics are shown in Figure 3 for all trajectories. Most of time, D_1 is between 0.04 and 0.06. Intersections with the ground state are found with D_1 between 0.06 and 0.09, reflecting the strong multireference character of the ground state in such cases, as expected. D_2 for S_1 is mostly between 0.25 and 0.35. Intersections with the ground state are found for D_2 in the upper region of this domain, indicating some contribution from double excitations near the crossing.

The exceptional numerical stability of the ADC(2) method manifested itself in the fact that, if the termination criteria are not applied, trajectories continue running with formal negative excitation energies (response state lower than the closed shell) after S_1 – S_0 crossings. However, note that the ADC(2) method is not able to treat this area of low S_1 – S_0 gaps properly. In this area, there should be strong mixing between the closed shell and the excited configurations, which is absent in the single reference treatment. Thus, ADC(2) cannot be expected to be able to properly represent the two-dimensional (2D) branching space for S_1 – S_0 crossings, just as this is the case for CIS and TDDFT (in its linear response formalism based on the adiabatic approximation).⁴⁴ Therefore, we want to stress that ADC(2) cannot describe the details of the deactivation process to the ground state. If information about the precise deactivation geometry is required or if the dynamics is to be continued in the S_0 state (as is the case, for example, when computing isomerization quantum yields), then ADC(2) is certainly not the method of choice and we suggest using one of the multireference methods, which are already available within Newton-X. However, if, as in the present case of adenine, we are interested in excited-state lifetimes or in the general deactivation pathways used, we can simulate the dynamics until a small energy gap to the ground state is reached. This provides approximately a lower limit for the excited-state lifetime and reliable distribution of excited-state pathways. Even more, if a fluorescent species is considered or if the primary interest lies in processes happening within the excited state manifold, ADC(2) (and, similarly, TDDFT with a properly chosen functional) may indeed be the efficient and reliable method of choice.

3.3.2. Numerical Test of the Coupling Elements. Before presenting the results of the dynamics simulations, we will discuss the reliability of the coupling elements as computed with the methodology described above. Unfortunately, no analytic coupling terms are available at the ADC(2) level. Therefore, we resort to MR-CI, for which analytical coupling vectors are implemented.⁴⁵ Specifically, we use MR-CIS out of a CAS(10,8) reference space, using the same aug-cc-pVDZ basis set used for the ADC(2) calculations. When performing this comparison, one should remember that differences will not only be derived from the approximations in the ADC(2) coupling elements, but also simply from differences in the wave function descriptions of the ADC(2) and MR-CIS methods. For this reason, a systematic evaluation is difficult and we will limit ourselves to the discussion of one exemplary trajectory (see Figure 4). This trajectory was chosen as a rather challenging case, showing two surface hops within a time window of 10 fs.

In the original ADC(2) trajectory (Figure 4, open circles (○)) there was a surface hop from S_1 to S_2 at 143.0 fs after photoexcitation, quickly followed by a second hop to S_1 at 148.5 fs. The first hop was initiated by a small decrease in the

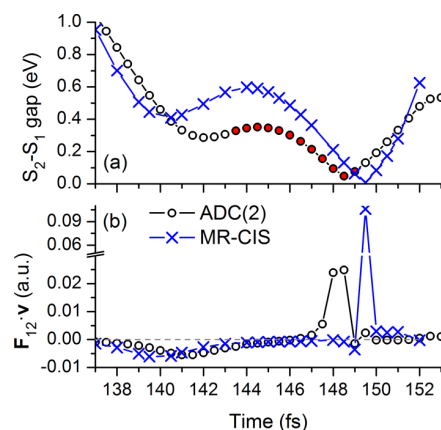


Figure 4. Comparison of the ADC(2) and MR-CIS methods for adenine, using a given ADC(2) trajectory: (a) energy gap between the first two excited states (solid red circles (●) mark times when the system is in the S_2 state) and (b) nonadiabatic coupling elements.

S_2 – S_1 energy gap (0.287 eV), accompanied by a modest $F_{12}\cdot v$ coupling element (as defined in eq 1) spread out over a few femtoseconds, reaching a maximum of -0.0055 a.u. at 141.5 fs. In the case of the second hop, the energy gap was significantly reduced (0.048 eV), which coincided with a strong positive coupling reaching up to 0.025 a.u., lasting for only two time steps.

To evaluate the reliability of these outcomes, we recomputed the same trajectory at the MR-CIS level. For this purpose, nonadiabatic coupling vectors F_{12} were evaluated at the geometries determined from ADC(2) and the $F_{12}\cdot v$ terms were explicitly computed with respect to the instantaneous velocities also derived from the ADC(2) trajectory. The results are presented as blue crosses (×) in Figure 4. The overall trends are very similar to ADC(2): In the first part, there is a lowering of the S_2 – S_1 gap, accompanied by a moderate coupling (reaching up to -0.0061 a.u., already at 139.5 fs). In the second part, there is a more weakly avoided crossing with a positive $F_{12}\cdot v$ element. As opposed to the ADC(2) calculations, the trajectory reaches a point, which is very close to the MR-CIS crossing seam (with an energy gap of 0.007 eV at 149.0 fs). This is accompanied by a highly peaked coupling element at the same time step (reaching a value of 0.106 a.u.).

In summary, one can say that the approximate ADC(2) couplings reproduced the results obtained with analytical MR-CIS coupling vectors in a semiquantitative way. Using the current implementation, even phase changes in the coupling elements can be readily identified, thus providing a good description of cases where multiple nonadiabatic events occur in close succession. Differences between the coupling elements (Figure 4b) correlate with energetic differences (Figure 4a), showing that these are, for the most part, derived from general differences between the ADC(2) and MR-CIS methods, rather than specifically from our approximation protocol.

3.3.3. Results of the ADC(2) Dynamics. Surface hopping trajectories were computed for a maximum of 1000 fs or until a S_1 – S_0 energy gap smaller than 0.1 eV was reached. Initially, 24% of the trajectories are in S_2 in the L-domain and 72% are in either S_2 or S_3 in the M-domain (see Table 3). This highly excited population deactivates to S_1 within 60 fs in the L-domain and 54 fs in the M-domain. After that, small population

fluctuations between S_1 and S_2 are observed along the dynamics.

In the cases that a small energy gap to the ground state was reached, we assumed that internal conversion to the ground state took place. The fraction of trajectories returning to the ground state within 1 ps, according to this criterion, is given in

Table 4. Fraction of Trajectories Returning to the Ground State within 1 ps

	Fraction of Trajectories	
	L-domain	M-domain
S_1	0.61	0.64
S_2	0.17	0.55
S_3		0.50
total	0.50 ± 0.12	0.57 ± 0.12
expt ^a	0.62 ± 0.02	0.68 ± 0.02

^aData taken from ref 21e.

Table 4. The margins of error for the deactivation yields were computed using the expression⁴⁶

$$\varepsilon = Z \sqrt{\frac{p(1-p)}{N}} \quad (6)$$

where p is the deactivation probability, N is the number of trajectories, and $Z = 1.6449$ for a 90% confidence interval.

Half of trajectories in the L-domain returned to the ground state. In the M-domain, 57% returned to the ground state. Assuming a simple exponential decay, we can use the experimental lifetimes^{21e} after pumping at 265.1 nm (L) and 251.3 nm (M) to estimate that 62% and 68% of the population, respectively, should be in the ground state within 1 ps. This means that ADC(2) estimates of the deactivation are somewhat smaller than the experimental values.

With 50 trajectories, the margin of error in the estimate of the deactivation is $\pm 12\%$ for a 90% confidence level. This implies, first, that the increase of the deactivation from L to M is not statistically significant. Second, the small level of deactivation predicted by ADC(2) compared with the experiment, although still within the limit of the statistical error, may indicate that ADC(2) is, in fact, overestimating the excited-state lifetime.

The distribution of trajectories in the space of the Cremer–Pople parameters⁴⁷ (Q , θ , and ϕ) is shown in Figure 5. There is no substantial distinction between trajectories in the L- and M-domains. Averaging over all time steps and trajectories, the degree of puckering (Q) in the pyrimidine ring is 0.22 Å for both domains, which is slightly smaller than the 0.27 Å observed at the S_1 minimum (see Table 2). The Q -distribution is very asymmetric, with almost no geometries near 0 Å (planar pyrimidine ring), and a long tail extending to Q as large as 0.7 Å. Intersections to the ground state are reached for $Q = 0.5 \pm 0.1$ Å.

The type of puckering deformation in the pyrimidine ring is given by the parameters θ and ϕ .⁴⁸ Trajectories cluster in two regions of this space corresponding to the 2E (envelope conformation with C2 above the ring plane) and E_2 (envelope with C2 below the plane). Crossings to the ground state are found not only at these C2-puckered regions, but also at C6-puckered regions (for instance, around $\theta = \phi = 120^\circ$). These deformations are related to the two types of puckered conical intersections shown in Figure 1.

The fractions of C2-puckered, C6-puckered, and N–H stretched geometries used for internal conversion to the ground state are given in Table 5. For the L-domain, internal conversion happens mainly through C2 deformations, but also C6 deformations play a considerable role. The importance of internal conversion through C6 increases in the M-domain, practically equaling C2, reflecting the larger amount of available energy. In both domains, N–H elimination is much more rare.

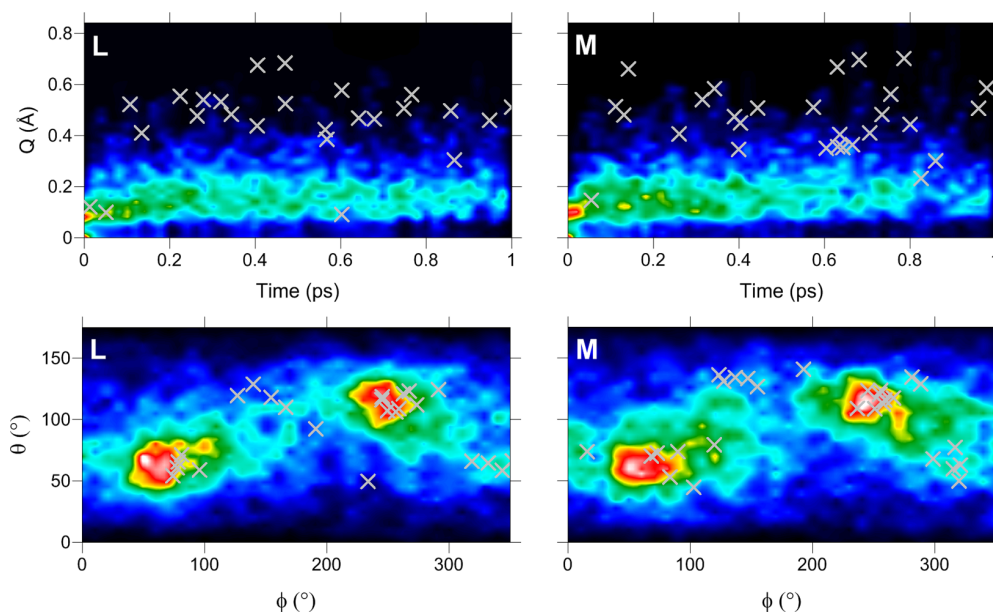


Figure 5. Distribution of Cremer–Pople parameters during the dynamics. Red regions indicate larger densities than black regions. The crosses indicate the smallest energy gap to the ground state ($\Delta E_{12} < 0.1$ eV) when trajectories are stopped.

Table 5. Fraction of Trajectories Returning to the Ground State in Each of the Three Main Deactivation Channels

	Fraction of Trajectories	
	L-domain	M-domain
C2	0.52	0.54
C6	0.36	0.43
H-elimin.	0.12	0.03

To help rationalize these results, ADC(2) energy profiles were computed with linear interpolation of internal coordinates (LIIC) between the S_0 minimum and the S_1 minimum, and then between the S_1 minimum and the conical intersections (Figure 6). Although LIIC tends to overestimate reaction

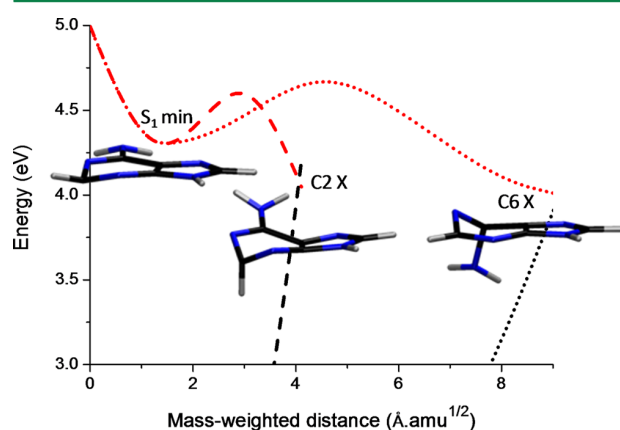


Figure 6. LIIC energy profiles of the ground and first excited states from the S_0 minimum to the S_1 minimum and then to the C2 and C6 conical intersections (X) computed with ADC(2).

barriers, it usually reflects the general features of the reaction paths well, especially when computed with natural internal coordinates,⁴⁹ as done here. The reaction barrier to move from the S_1 minimum to the C2 conical intersection is slightly smaller than that to move to the C6 intersection by 0.08 eV. Moreover, the barrier to C2 is much closer to the S_1 minimum than the barrier to C6. Thus, energetic factors (barrier height) and, especially, entropic factors (barrier distance) favor adenine to move toward C2 intersection rather than to C6 intersection. This is an indication that the slight predominance of C2 deformations (Table 5) may persist, even for a more statistically significant ensemble of data.

3.3.4. Comparison among Methods. In a previous work,³ we reported dynamics simulations of 9H-adenine with several different methods, including ab initio and semiempirical versions of multireference configuration interaction (MR-CIS and OM2/MRCI, respectively), and TDDFT with several functionals. The predicted S_0 populations at 1 ps for the M-domain are shown in Figure 7, together with the experimental result from ref 21e. We found out that excited-state lifetimes and distribution of reaction pathways could be significantly different among the methods, because of the quality of the potential energy surfaces.

The ultrafast deactivation of adenine is predicted to occur at deactivation rates comparable to experiment at ADC(2), OM2/MRCI, and MR-CIS levels, although MR-CIS overshoots the rate somewhat. No matter the functional, the deactivation level predicted by TDDFT is far too low, even taking into account

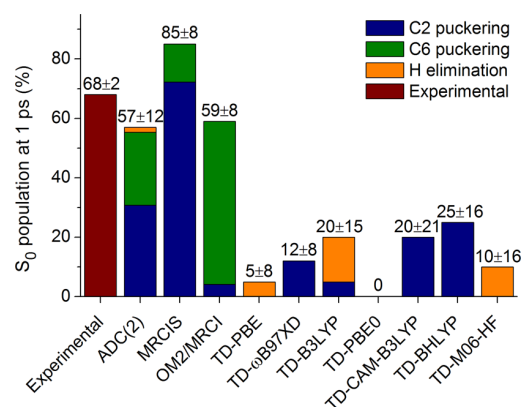


Figure 7. Comparison of the present ADC(2) results for deactivation within 1 ps with the experimental^{21e} and diverse computational³ results. The TD- ω B97XD result is also reported here for the first time. Margins of error estimated for a 90% confidence level.

the large margins of errors that are due to the small trajectory samples. With OM2/MRCI, deactivation occurs mostly at C6 deformed geometries, whereas with MR-CIS, it occurs mostly at C2 deformed ones. With ADC(2), deactivation occurs mainly at C2 deformation, but with considerable contribution of C6. In ref 3, it has been shown that better balanced active and reference spaces increase the participation of C6 deformed geometries in MR-CIS dynamics, bringing it closer to the ADC(2) result.

TDDFT with the ω B97XD functional, which is reported here for the first time, followed the same pattern that has been observed with other functionals discussed in ref 3. Fifty (50) trajectories—30 starting in S_2 and 20 in S_3 —were simulated, sampling the entire first spectral band. The deactivation level was very small and only 6 trajectories (12%) returned to ground state within 1 ps. For all 6 of these trajectories, C2 deformations are responsible for the energy crossing, which is also consistent with the previous TDDFT results for other functionals. As we have discussed in ref 3, the failure of TDDFT to describe the excited-state dynamics of adenine is related to the DFT overstabilization of the ground-state potential energy along planar distortions, compared to out-of-plane distortions. This effect creates a bias toward motion with small degree of puckering, delaying the time to reach the conical intersections.

Even though ADC(2) and OM2/MRCI predict similar S_0 populations (Figure 7), potential energy profiles computed at these and higher levels of theory³ indicate that ADC(2) results should provide the best results. Compared with CC2 and CASPT2 profiles (see Figure 4 of ref 3), OM2/MRCI clearly underestimates the reaction barrier between the S_1 minimum and the C6-puckered conical intersection. This not only explains the high number of hops at C6-puckered geometries, but also indicates that OM2/MRCI may be predicting the right excited-state lifetime in part for the wrong reason. ADC(2), in turn, has potential energy profiles that compare very well to the high-level calculations (compare Figure 6 with Figure 4 of ref 3).

One question that remains is why the S_0 population predicted by ADC(2) ($57 \pm 12\%$) is smaller (at a significance level of 0.1) than the experimental result ($68 \pm 2\%$). Although we would need better statistical samples to clarify this point, we want to briefly discuss possible reasons for this

discrepancy. This, of course, could be an indication of a methodological shortcoming, e.g., that ADC(2) is not properly describing the potential energy surface of the lowest excited state of adenine. We may also point out that other elements may partially account for the divergence. First, the simulations included only the 9H tautomer, whereas the experiment may have appreciable amounts of the 7H tautomer. Another source of divergence is that, while the simulations are really providing the S_0 population at 1 ps (or with the present methodology at least an upper bound to it), the experimental value corresponds to the fitting of the transient absorption spectrum, which includes information of the ionization process during the probing.^{21f,32}

4. CONCLUSIONS

Nonadiabatic surface hopping dynamics was implemented based on on-the-fly electronic structure calculations with the CC2 and ADC(2) methods available in the Turbomole program. The implementation of surface hopping based on TDDFT available in Gaussian 09 also is reported. For all cases, nonadiabatic couplings are based on overlaps of formal CIS wave functions. In practical terms, dynamics can be performed only with ADC(2) and TDDFT, which do not suffer from the instabilities near degenerate excited states observed in methods with nonsymmetrical Jacobians.

As a common limitation of a single-reference method, internal conversion to the ground state cannot be simulated with ADC(2), although it is possible to follow the nonadiabatic dynamics involving several excited states until the minimum of the first excited state or a crossing to the ground state is reached. The method is also of limited utility when states with strong double-excitation character are in play. On the other hand, ADC(2) dynamics (and, in a similar sense, TDDFT with a proper functional) should be particularly suitable when dynamical processes occurring within the excited-state manifold are of interest (e.g., exciton dynamics,⁵⁰ energy or electron transfer,¹⁵ excimer formation,⁵¹ and excited-state proton transfer⁵²).

9H-Adenine in the gas phase, for which experimental data and simulated dynamics at various levels are available, was taken as a test case. The deactivation to the ground state predicted by ADC(2) is qualitatively correct, but somewhat smaller than the experimental result. As the present example of adenine shows, the ADC(2) method has been proven to be a very viable candidate in performing photodynamics simulations under the conditions discussed above. The present TDDFT results failed to predict the ultrafast deactivation of 9H-adenine, which is consistent with previous TDDFT simulations.³

A long-standing problem in dynamics of 9H-adenine is the role of each region of the intersection seam for internal conversion. ADC(2) dynamics predicted that conical intersections with C2 deformations are the main deactivation channel in the dynamics starting in the low-energy region of the spectrum. Intersections with C6 deformations are relevant as well, and its importance tends to increase for absorption in the high-energy part of the spectrum. Intersections due to H elimination play only a minor role.

Based on these results for adenine, we conclude that surface hopping with ADC(2) has a great potential as a single-reference method to provide high-level information on nonadiabatic processes involving multiple excited states. However, it will require more investigations to prove the generally excellent performance of ADC(2).

AUTHOR INFORMATION

Corresponding Authors

*E-mail: felix.plasser@iwr.uni-heidelberg.de (F.P.).

*E-mail: barbatti@kofo.mpg.de (M.B.).

Present Address

[○]Department of Chemistry, University of Bath, Claverton Down, BA2 7AY—Bath, U.K.

Notes

The authors declare no competing financial interest.

ACKNOWLEDGMENTS

F.P. is a recipient of a fellowship for postdoctoral researchers by the Alexander von Humboldt foundation. J.P. and M.P. acknowledge the support by the Grant Agency of Czech Republic (Project No. 208/12/0559). Support by the National Science Foundation (under Project No. CHE-1213263) and by the Robert A. Welch Foundation (under Grant No. D-0005) is also acknowledged. Computer time at the Vienna Scientific Cluster (Project No. 70019) is gratefully acknowledged.

REFERENCES

- (1) (a) Barbatti, M. Nonadiabatic dynamics with trajectory surface hopping method. *WIREs: Comput. Mol. Sci.* **2011**, *1*, 620–633. (b) Tully, J. C. Molecular-Dynamics with Electronic-Transitions. *J. Chem. Phys.* **1990**, *93*, 1061–1071.
- (2) Nelson, T.; Fernandez-Alberti, S.; Chernyak, V.; Roitberg, A. E.; Tretiak, S. Nonadiabatic excited-state molecular dynamics: Numerical tests of convergence and parameters. *J. Chem. Phys.* **2012**, *136*, 054108.
- (3) Barbatti, M.; Lan, Z.; Crespo-Otero, R.; Szymczak, J. J.; Lischka, H.; Thiel, W. Critical appraisal of excited state nonadiabatic dynamics simulations of 9H-adenine. *J. Chem. Phys.* **2012**, *137*, 22A503.
- (4) (a) Bonačić-Koutecký, V.; Mitrić, R. Theoretical exploration of ultrafast dynamics in atomic clusters: Analysis and control. *Chem. Rev.* **2005**, *105*, 11–65. (b) Tapavicz, E.; Meyer, A. M.; Furche, F. Unravelling the details of vitamin D photosynthesis by non-adiabatic molecular dynamics simulations. *Phys. Chem. Chem. Phys.* **2011**, *13*, 20986–20998. (c) Curchod, B. F. E.; Rothlisberger, U.; Tavernelli, I. Trajectory-Based Nonadiabatic Dynamics with Time-Dependent Density Functional Theory. *ChemPhysChem* **2013**, *14*, 1314–1340.
- (5) (a) Christiansen, O.; Koch, H.; Jorgensen, P. The 2nd-Order Approximate Coupled-Cluster Singles and Doubles Model CC2. *Chem. Phys. Lett.* **1995**, *243*, 409–418. (b) Hättig, C.; Weigend, F. CC2 excitation energy calculations on large molecules using the resolution of the identity approximation. *J. Chem. Phys.* **2000**, *113*, 5154–5161. (c) Hättig, C.; Köhn, A. Transition moments and excited-state first-order properties in the coupled-cluster model CC2 using the resolution-of-the-identity approximation. *J. Chem. Phys.* **2002**, *117*, 6939–6951.
- (6) (a) Schirmer, J. Beyond the random-phase approximation: A new approximation scheme for the polarization propagator. *Phys. Rev. A* **1982**, *26*, 2395–2416. (b) Trofimov, A. B.; Schirmer, J. An efficient polarization propagator approach to valence electron excitation spectra. *J. Phys. B: At., Mol. Opt. Phys.* **1995**, *28*, 2299–2324.
- (7) (a) Barbatti, M.; Granucci, G.; Ruckebauer, M.; Plasser, F.; Crespo-Otero, R.; Pittner, J.; Persico, M.; Lischka, H. *NEWTON-X: A package for Newtonian dynamics close to the crossing seam*. Available via the Internet at www.newtonx.org, 2013. (b) Barbatti, M.; Ruckebauer, M.; Plasser, F.; Pittner, J.; Granucci, G.; Persico, M.; Lischka, H. *Newton-X: A surface-hopping program for nonadiabatic molecular dynamics*. *WIREs: Comput. Mol. Sci.* **2014**, *4*, 26–33.
- (8) Ahlrichs, R.; Bär, M.; Häser, M.; Horn, H.; Kölmel, C. Electronic-Structure Calculations on Workstation Computers—The Program System Turbomole. *Chem. Phys. Lett.* **1989**, *162*, 165–169.
- (9) Frisch, M. J.; Trucks, G. W.; Schlegel, H. B.; Scuseria, G. E.; Robb, M. A.; Cheeseman, J. R.; Scalmani, G.; Barone, V.; Mennucci, B.; Petersson, G. A.; Nakatsuji, H.; Caricato, M.; Li, X.; Hratchian, H.

- P.; Izmaylov, A. F.; Bloino, J.; Zheng, G.; Sonnenberg, J. L.; Hada, M.; Ehara, M.; Toyota, K.; Fukuda, R.; Hasegawa, J.; Ishida, M.; Nakajima, T.; Honda, Y.; Kitao, O.; Nakai, H.; Vreven, T.; Montgomery, J. J., A.; Peralta, J. E.; Ogliaro, F.; Bearpark, M.; Heyd, J. J.; Brothers, E.; Kudin, K. N.; Staroverov, V. N.; Kobayashi, R.; Normand, J.; Raghavachari, K.; Rendell, A.; Burant, J. C.; Iyengar, S. S.; Tomasi, J.; Cossi, M.; Rega, N.; Millam, N. J.; Klene, M.; Knox, J. E.; Cross, J. B.; Bakken, V.; Adamo, C.; Jaramillo, J.; Gomperts, R.; Stratmann, R. E.; Yazyev, O.; Austin, A. J.; Cammi, R.; Pomelli, C.; Ochterski, J. W.; Martin, R. L.; Morokuma, K.; Zakrzewski, V. G.; Voth, G. A.; Salvador, P.; Dannenberg, J. J.; Dapprich, S.; Daniels, A. D.; Farkas, Ö.; Foresman, J. B.; Ortiz, J. V.; Cioslowski, J.; Fox, D. J. *Gaussian 09, Revision D.01*; Gaussian, Inc.: Wallingford, CT, 2013.
- (10) Chai, J.-D.; Head-Gordon, M. Systematic optimization of long-range corrected hybrid density functionals. *J. Chem. Phys.* **2008**, *128*, 084106.
- (11) Hirata, S.; Head-Gordon, M. Time-dependent density functional theory within the Tamm–Dancoff approximation. *Chem. Phys. Lett.* **1999**, *314*, 291–299.
- (12) (a) Christiansen, O. First-order nonadiabatic coupling matrix elements using coupled cluster methods. I. Theory. *J. Chem. Phys.* **1999**, *110*, 711–723. (b) Ichino, T.; Gauss, J.; Stanton, J. F. Quasidiabatic states described by coupled-cluster theory. *J. Chem. Phys.* **2009**, *130*, 174105. (c) Tajti, A.; Szalay, P. G. Analytic evaluation of the nonadiabatic coupling vector between excited states using equation-of-motion coupled-cluster theory. *J. Chem. Phys.* **2009**, *131*, 124104.
- (13) Hammes-Schiffer, S.; Tully, J. C. Proton-Transfer in Solution—Molecular-Dynamics with Quantum Transitions. *J. Chem. Phys.* **1994**, *101*, 4657–4667.
- (14) Granucci, G.; Persico, M.; Toniolo, A. Direct semiclassical simulation of photochemical processes with semiempirical wave functions. *J. Chem. Phys.* **2001**, *114*, 10608.
- (15) Plasser, F.; Granucci, G.; Pittner, J.; Barbatti, M.; Persico, M.; Lischka, H. Surface hopping dynamics using a locally diabatic formalism: Charge transfer in the ethylene dimer cation and excited state dynamics in the 2-pyridone dimer. *J. Chem. Phys.* **2012**, *137*, 22A514.
- (16) Barbatti, M.; Lischka, H. Nonadiabatic Deactivation of 9H-Adenine: A Comprehensive Picture Based on Mixed Quantum-Classical Dynamics. *J. Am. Chem. Soc.* **2008**, *130*, 6831–6839.
- (17) Fabiano, E.; Thiel, W. Nonradiative deexcitation dynamics of 9H-adenine: An OM2 surface hopping study. *J. Phys. Chem. A* **2008**, *112*, 6859–6863.
- (18) Alexandrova, A. N.; Tully, J. C.; Granucci, G. Photochemistry of DNA Fragments via Semiclassical Nonadiabatic Dynamics. *J. Phys. Chem. B* **2010**, *114*, 12116–12128.
- (19) Picconi, D.; Avila Ferrer, F. J.; Improta, R.; Lami, A.; Santoro, F. Quantum-classical effective-modes dynamics of the $\pi\pi^* \rightarrow n\pi^*$ decay in 9H-adenine. A quadratic vibronic coupling model. *Faraday Discuss.* **2013**, *163*, 223–242.
- (20) (a) Lei, Y.; Yuan, S.; Dou, Y.; Wang, Y.; Wen, Z. Detailed Dynamics of the Nonradiative Deactivation of Adenine: A Semiclassical Dynamics Study. *J. Phys. Chem. A* **2008**, *112*, 8497–8504. (b) Mitrić, R.; Werner, U.; Wohlgemuth, M.; Seifert, G.; Bonacić-Koutecký, V. Nonadiabatic Dynamics within Time-Dependent Density Functional Tight Binding Method. *J. Phys. Chem. A* **2009**, *113*, 12700–12705.
- (21) (a) Kang, H.; Jung, B.; Kim, S. K. Mechanism for ultrafast internal conversion of adenine. *J. Chem. Phys.* **2003**, *118*, 6717–6719. (b) Ullrich, S.; Schultz, T.; Zgierski, M. Z.; Stolow, A. Direct observation of electronic relaxation dynamics in adenine via time-resolved photoelectron spectroscopy. *J. Am. Chem. Soc.* **2004**, *126*, 2262–2263. (c) Canuel, C.; Mons, M.; Piuzzi, F.; Tardivel, B.; Dimicoli, I.; Elhanine, M. Excited states dynamics of DNA and RNA bases: Characterization of a stepwise deactivation pathway in the gas phase. *J. Chem. Phys.* **2005**, *122*, 074316. (d) Satzger, H.; Townsend, D.; Zgierski, M. Z.; Patchkovskii, S.; Ullrich, S.; Stolow, A. Primary processes underlying the photostability of isolated DNA bases: Adenine. *Proc. Natl. Acad. Sci. U.S.A.* **2006**, *103*, 10196–10201. (e) Evans, N. L.; Ullrich, S. Wavelength Dependence of Electronic Relaxation in Isolated Adenine Using UV Femtosecond Time-Resolved Photoelectron Spectroscopy. *J. Phys. Chem. A* **2010**, *114*, 11225–11230. (f) Kotur, M.; Weinacht, T. C.; Congyi, Z.; Matsika, S. Following Ultrafast Radiationless Relaxation Dynamics With Strong Field Dissociative Ionization: A Comparison Between Adenine, Uracil, and Cytosine. *IEEE J. Sel. Top. Quant.* **2012**, *18*, 187–194.
- (22) Granucci, G.; Persico, M. Critical appraisal of the fewest switches algorithm for surface hopping. *J. Chem. Phys.* **2007**, *126*, 134114.
- (23) Casida, M. E.; Huix-Rotllant, M. Progress in Time-Dependent Density-Functional Theory. *Annu. Rev. Phys. Chem.* **2012**, *63*, 287–323.
- (24) Hättig, C., Structure Optimizations for Excited States with Correlated Second-Order Methods: CC2 and ADC(2). In *Advances in Quantum Chemistry*, Vol. 50; Jensen, H. J. Å., Ed.; Academic Press: New York, 2005; pp 37–60.
- (25) (a) Tapavicza, E.; Tavernelli, I.; Rothlisberger, U. Trajectory surface hopping within linear response time-dependent density-functional theory. *Phys. Rev. Lett.* **2007**, *98*, 023001. (b) Mitrić, R.; Werner, U.; Bonacić-Koutecký, V. Nonadiabatic dynamics and simulation of time resolved photoelectron spectra within time-dependent density functional theory: Ultrafast photoswitching in benzylideneaniline. *J. Chem. Phys.* **2008**, *129*, 9. (c) Barbatti, M.; Pittner, J.; Pederzoli, M.; Werner, U.; Mitrić, R.; Bonacić-Koutecký, V.; Lischka, H. Non-adiabatic dynamics of pyrrole: Dependence of deactivation mechanisms on the excitation energy. *Chem. Phys.* **2010**, *375*, 26–34.
- (26) Casida, M., Time-dependent density functional response theory for molecules. In *Recent advances in density functional methods, Part I*; Chong, D., Ed.; World Scientific: Singapore, 1995; pp 155–192.
- (27) Pittner, J.; Lischka, H.; Barbatti, M. Optimization of mixed quantum-classical dynamics: Time-derivative coupling terms and selected couplings. *Chem. Phys.* **2009**, *356*, 147–152.
- (28) Crespo-Otero, R.; Barbatti, M. Spectrum simulation and decomposition with nuclear ensemble: formal derivation and application to benzene, furan and 2-phenylfuran. *Theor. Chem. Acc.* **2012**, *131*, 1237.
- (29) Chai, J.-D.; Head-Gordon, M. Long-range corrected hybrid density functionals with damped atom–atom dispersion corrections. *Phys. Chem. Chem. Phys.* **2008**, *10*, 6615–6620.
- (30) Dunning, T. H. Gaussian-Basis Sets for Use in Correlated Molecular Calculations. 1. The Atoms Boron through Neon and Hydrogen. *J. Chem. Phys.* **1989**, *90*, 1007–1023.
- (31) (a) Lischka, H.; Müller, T.; Szalay, P. G.; Shavitt, I.; Pitzer, R. M.; Shepard, R. COLUMBUS—A program system for advanced multireference theory calculations. *Wiley Interdiscip. Rev.—Comput. Mol. Sci.* **2011**, *1*, 191–199. (b) Lischka, H.; Shepard, R.; Shavitt, I.; Pitzer, R. M.; Dallos, M.; Müller, T.; Szalay, P. G.; Brown, F. B.; Ahlrichs, R.; Böhm, H. J.; Chang, A.; Comeau, D. C.; Gdanitz, R.; Dachsel, H.; Ehrhardt, C.; Ernzerhof, M.; Höchtl, P.; Irle, S.; Kedziora, G.; Kovar, T.; Parasuk, V.; Pepper, M. J. M.; Scharf, P.; Schiffer, H.; Schindler, M.; Schüler, M.; Seth, M.; Stahlberg, E. A.; Zhao, J.-G.; Yabushita, S.; Zhang, Z.; Barbatti, M.; Matsika, S.; Schuurmann, M.; Yarkony, D. R.; Brozell, S. R.; Beck, E. V.; Blaudeau, J.-P.; Ruckebauer, M.; Sellner, B.; Plasser, F.; Szymczak, J. J. COLUMBUS, An Ab Initio Electronic Structure Program, Release 7.0. Available via the Internet at www.univie.ac.at/columbus, 2012.
- (32) Barbatti, M.; Ullrich, S. Ionization potentials of adenine along the internal conversion pathways. *Phys. Chem. Chem. Phys.* **2011**, *13*, 15492–15500.
- (33) (a) Clark, L. B.; Peschel, G. G.; Tinoco, I. Vapor Spectra and Heats of Vaporization of Some Purine and Pyrimidine Bases. *J. Phys. Chem.* **1965**, *69*, 3615–3618. (b) Li, L.; Lubman, D. M. Ultraviolet Visible Absorption-Spectra of Biological Molecules in the Gas-Phase Using Pulsed Laser-Induced Volatilization Enhancement in a Diode-Array Spectrophotometer. *Anal. Chem.* **1987**, *59*, 2538–2541.

- (34) Fleig, T.; Knecht, S.; Hättig, C. Quantum-chemical investigation of the structures and electronic spectra of the nucleic acid bases at the coupled cluster CC2 level. *J. Phys. Chem. A* **2007**, *111*, 5482–5491.
- (35) Szalay, P. G.; Watson, T.; Perera, A.; Lotrich, V. F.; Bartlett, R. J. Benchmark Studies on the Building Blocks of DNA. I. Superiority of Coupled Cluster Methods in Describing the Excited States of Nucleobases in the Franck–Condon Region. *J. Phys. Chem. A* **2012**, *116*, 6702–6710.
- (36) Daniels, M.; Hauswirth, W. Fluorescence of the Purine and Pyrimidine Bases of the Nucleic Acids in Neutral Aqueous Solution at 300°K. *Science* **1971**, *171*, 675–677.
- (37) Engler, G.; Seefeld, K.; Schmitt, M.; Tatchen, J.; Grotkopp, O.; Muller, T. J. J.; Kleineremanns, K. Acetylation makes the difference: A joint experimental and theoretical study on low-lying electronically excited states of 9H-adenine and 9-acetyladenine. *Phys. Chem. Chem. Phys.* **2013**, *15*, 1025–1031.
- (38) Nir, E.; Plutzer, C.; Kleineremanns, K.; de Vries, M. Properties of isolated DNA bases, base pairs and nucleosides examined by laser spectroscopy. *Eur. Phys. J. D* **2002**, *20*, 317–329.
- (39) Serrano-Andrés, L.; Merchán, M.; Borin, A. C. A three-state model for the photophysics of adenine. *Chem.—Eur. J.* **2006**, *12*, 6559–6571.
- (40) Middleton, C. T.; de La Harpe, K.; Su, C.; Law, Y. K.; Crespo-Hernandez, C. E.; Kohler, B. DNA Excited-State Dynamics: From Single Bases to the Double Helix. *Annu. Rev. Phys. Chem.* **2009**, *60*, 217–239.
- (41) Send, R.; Kaila, V. R. I.; Sundholm, D. Reduction of the virtual space for coupled-cluster excitation energies of large molecules and embedded systems. *J. Chem. Phys.* **2011**, *134*, 214114.
- (42) (a) Janssen, C. L.; Nielsen, I. M. B. New diagnostics for coupled-cluster and Møller–Plesset perturbation theory. *Chem. Phys. Lett.* **1998**, *290*, 423–430. (b) Nielsen, I. M. B.; Janssen, C. L. Double-substitution-based diagnostics for coupled-cluster and Møller–Plesset perturbation theory. *Chem. Phys. Lett.* **1999**, *310*, 568–576.
- (43) Köhn, A.; Hättig, C. Analytic gradients for excited states in the coupled-cluster model CC2 employing the resolution-of-the-identity approximation. *J. Chem. Phys.* **2003**, *119*, 5021–5036.
- (44) Levine, B. G.; Ko, C.; Quenneville, J.; Martínez, T. J. Conical intersections and double excitations in time-dependent density functional theory. *Mol. Phys.* **2006**, *104*, 1039–1051.
- (45) Lischka, H.; Dallos, M.; Szalay, P. G.; Yarkony, D. R.; Shepard, R. Analytic evaluation of nonadiabatic coupling terms at the MR-CI level. I. Formalism. *J. Chem. Phys.* **2004**, *120*, 7322–7329.
- (46) Devore, J. L. *Probability & Statistics for Engineering and the Sciences*, 8th Edition; Cengage Learning: Stamford, CT, 2012; p 768.
- (47) Cremer, D.; Pople, J. A. General Definition of Ring Puckering Coordinates. *J. Am. Chem. Soc.* **1975**, *97*, 1354–1358.
- (48) Boeyens, J. C. A. The conformation of six-membered rings. *J. Chem. Crystallogr.* **1978**, *8*, 317–320.
- (49) Fogarasi, G.; Zhou, X. F.; Taylor, P. W.; Pulay, P. The Calculation of Abinitio Molecular Geometries—Efficient Optimization by Natural Internal Coordinates and Empirical Correction by Offset Forces. *J. Am. Chem. Soc.* **1992**, *114*, 8191–8201.
- (50) Bittner, E. R. Frenkel exciton model of ultrafast excited state dynamics in AT DNA double helices. *J. Photochem. Photobiol. A* **2007**, *190*, 328–334.
- (51) Plasser, F.; Lischka, H. Electronic excitation and structural relaxation of the adenine dinucleotide in gas phase and solution. *Photochem. Photobiol. Sci.* **2013**, *12*, 1440–1452.
- (52) Plasser, F.; Barbatti, M.; Aquino, A. J. A.; Lischka, H. Excited-State Diproton Transfer in [2,2'-Bipyridyl]-3,3'-diol: The Mechanism Is Sequential, Not Concerted. *J. Phys. Chem. A* **2009**, *113*, 8490–8499.

A new approach to molecular dynamics with non-adiabatic and spin-orbit effects with applications to QM/MM simulations of thiophene and selenophene

Marek Pederzoli^{1,2,a)} and Jiří Pittner^{1,b)}

¹*J. Heyrovský Institute of Physical Chemistry, Academy of Sciences of the Czech Republic, v.v.i., Dolejškova 3, 18223 Prague 8, Czech Republic*

²*Faculty of Science, Department of Physical and Macromolecular Chemistry, Charles University in Prague, Hlavova 8, 12840 Prague 2, Czech Republic*

(Received 25 November 2016; accepted 23 February 2017; published online 16 March 2017)

We present surface hopping dynamics on potential energy surfaces resulting from the spin-orbit splitting, i.e., surfaces corresponding to the eigenstates of the total electronic Hamiltonian including the spin-orbit coupling. In this approach, difficulties arise because of random phases of degenerate eigenvectors and possibility of crossings of the resulting mixed states. Our implementation solves these problems and allows propagation of the coefficients both in the representation of the spin free Hamiltonian and directly in the “diagonal representation” of the mixed states. We also provide a detailed discussion of the state crossing and point out several peculiarities that were not mentioned in the previous literature. We also incorporate the effect of the environment via the quantum mechanics/molecular mechanics approach. As a test case, we apply our methodology to deactivation of thiophene and selenophene in the gas phase, ethanol solution, and bulk liquid phase. First, 100 trajectories without spin-orbit coupling have been calculated for thiophene starting both in S_1 and S_2 states. A subset of 32 initial conditions starting in the S_2 state was then used for gas phase simulations with spin-orbit coupling utilizing the 3-step integrator of SHARC, our implementation of the 3-step propagator in Newton-X and two new “one-step” approaches. Subsequently, we carried out simulations in ethanol solution and bulk liquid phase for both thiophene and selenophene. For both molecules, the deactivation of the S_2 state proceeds via the ring opening pathway. The total population of triplet states reaches around 15% and 40% after 80 fs for thiophene and selenophene, respectively. However, it only begins growing after the ring opening is initiated; hence, the triplet states do not directly contribute to the deactivation mechanism. For thiophene, the resulting deactivation lifetime of the S_2 state was 68 fs in the gas phase, 76 fs in ethanol solution, and 78 fs in the liquid phase, in a good agreement with the experimental value of 80 fs (liquid phase). For selenophene, the obtained S_2 lifetime was 60 fs in the gas phase and 62 fs for both ethanol solution and liquid phase. The higher rate of intersystem crossing to the triplet states in selenophene is likely the reason for the lower fluorescence observed in selenium containing polymer compounds. *Published by AIP Publishing.* [<http://dx.doi.org/10.1063/1.4978289>]

I. INTRODUCTION

The usefulness of molecular dynamics (MD) simulations at the present time can hardly be overestimated. It can provide accurate information about the relationships between the macroscopic properties of a system and the underlying interactions among the constituent atoms and molecules. It has proved extremely valuable for elucidating the dynamics of a very wide range of elementary chemical processes including photochemistry at various time scales, material properties, and protein and nucleic acids dynamics.¹ The ever-increasing power of computers makes it possible to calculate ever more accurate results about larger and larger systems.

When performing MD simulations of photochemical processes, the situation is complicated by the presence of

conical intersections and avoided crossings between excited states, which enable non-radiative transitions between different potential energy surfaces and are thus essential for understanding photochemical processes.² Moreover, non-radiative transitions between states of different spin multiplicities, called inter-system crossings (ISCs), play also an important role in some photochemical reactions. They are forbidden in the non-relativistic limit, but occur when the spin-orbit coupling (SOC) becomes non-negligible. This is generally the case when heavy atoms are involved (and spin is not any more a good quantum number), but ISC can actually become the dominant process after excitation also in light-atom molecules.²

Surface hopping molecular dynamics³ is a widely used semi-classical approach to incorporate non-adiabatic effects into MD simulations, where the motion of the nuclei was represented by classical trajectories computed by numerical integration of Newton's equations while the time evolution of the population of each electronic state is treated

^{a)}Electronic mail: marek.pederzoli@jh-inst.cas.cz

^{b)}Author to whom correspondence should be addressed. Electronic mail: jiri.pittner@jh-inst.cas.cz

separately. Transition probability between each pair of states is computed and a stochastic algorithm is used to decide whether a transition (“hop”) will occur. If a hop occurs, the classical trajectory will be propagated on a different potential energy surface in the following time steps. Statistical analysis over a large set of independent trajectories then yields the approximate time-dependent quantum populations as a fraction of trajectories in each state along the trajectories.

In order to allow intersystem crossings in surface hopping molecular dynamics, we need to take spin-orbit couplings into account. Various approaches to this problem have been developed in the recent years.^{4–13} In the most commonly used approach,^{4–10} each spin multiplet is considered as a single electronic state. It was, however, recently shown by Granucci *et al.*¹⁴ that this approach is incorrect and that the multiplet components must be treated separately. A suitable approach is to diagonalize the Hamiltonian including the spin-orbit couplings and perform dynamics on resulting potential energy surfaces as introduced by Gonzalez and co-workers.¹⁵ This approach requires calculation of the derivative of the matrix of eigenvectors U (see Sec. II for details) and poses many difficulties with proper phase alignment of the U matrices in the consecutive MD steps. Several papers have been using this approach, but the problems were difficult to solve and the authors suggested to avoid the need for phase alignment altogether using the so-called 3-step propagator approach, where the coefficients are transformed to the molecular Coulomb Hamiltonian (MCH) representation, propagated, and transformed back to the diagonal representation.¹⁶

In this paper, we present a more general implementation that handles the problems with the phase alignment and allows propagation not only in the MCH representation, but also directly in the representation where the Hamiltonian is locally diagonal, using the explicit U derivative. Additionally, we show that the 3-step propagator actually does need phase adjustment for the case of (almost) degenerate eigenvalues, which applies to the systems with small spin-orbit splitting.

First, we test our implementation on a simple two-state model system where we reproduce results obtained using SHARC code. We also use an extended version of this model to illustrate the necessity for phase control in the 3-step propagator. Then, we proceed to the real photochemical applications and simulate the ultrafast deactivation of thiophene and selenophene in gas phase and in solution.

Thiophene and selenophene (see Figure 1 for the structures) are both important heterocyclic molecules that are widely used as building blocks for a large variety of polymers, organic dyes, pharmaceuticals, and other compounds.^{17,18} Both these molecules have been quite extensively studied both experimentally (see, for example, Refs. 19–22 and references

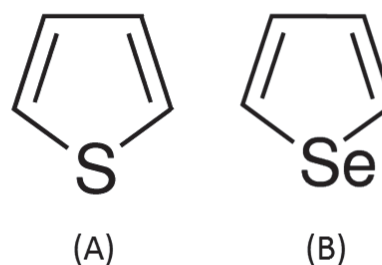


FIG. 1. Molecular structures of thiophene (a) and selenophene (b).

within) and theoretically.^{21–35} It has been suggested that the deactivation of thiophene is ultrafast in the order of 100 fs with possible involvement of ISCs.³⁶ Cui and Fang³² have simulated ultrafast deactivation of thiophene after S_1 excitation at the complete active space self-consistent field (CASSCF) level. Very recently, similar results have been obtained by dynamics at time-dependent density functional theory (TD-DFT),³⁷ and ADC(2)³⁸ levels for both S_1 and S_2 states but neither of these works investigated the effect of spin-orbit coupling nor the solvent effects.

For selenophene, involvement of ISCs may be even more pronounced due to higher spin-orbit coupling.³⁹ Recently it has been claimed responsible for lower fluorescence in selenium containing polymer compounds.^{40,41} Moreover, due to the relatively small number of atoms, these molecules are excellent candidates for the application of our methodology from the computational point of view.

II. THEORY

We consider the total molecular Hamiltonian to be the sum of molecular Coulomb Hamiltonian (MCH) and spin-orbit (SO) Hamiltonian,

$$H^{\text{tot}} = H^{\text{MCH}} + H^{\text{SO}}, \quad (1)$$

where the Breit-Pauli SO Hamiltonian is

$$H^{\text{SO}} = \frac{1}{2m^2c^2} \left[\sum_i \sum_C \frac{Z_C e^2}{r_{iC}^3} \hat{\mathbf{l}}_{iC} \cdot \hat{\mathbf{s}}_i - \sum_{ij} \frac{e^2}{r_{ij}^3} \hat{\mathbf{l}}_{ij} \cdot (\hat{\mathbf{s}}_i + 2\hat{\mathbf{s}}_j) \right]. \quad (2)$$

We compute and diagonalize H^{SO} matrix in a subset of eigenstates of H^{MCH} (all multiplet components of different M_S have to be considered). In the present work, we have interfaced Newton-X^{42,43} with Molpro,⁴⁴ where the SO matrix elements for CASSCF wave function are implemented by means of an effective one-electron Fock approach, which computes directly the two-electron contributions without storing the integrals.⁴⁵

The trajectories can be propagated on surfaces corresponding to eigenstates of H^{MCH} using the Tully’s fewest switches approach. When working in the MCH basis ϕ_j , propagation of the wave function coefficients becomes

$$\frac{dc_k(t)}{dt} = \sum_j \left[\underbrace{-i(E_j^{\text{MCH}} \delta_{kj} + \langle \phi_k | H^{\text{SO}} | \phi_j \rangle)}_{H_{kj}^{\text{tot}}(R(t))} - \underbrace{\dot{\mathbf{R}}(t) \cdot \langle \phi_k | \nabla_R | \phi_j \rangle}_{K_{kj}(R(t))} \right] c_j(t) \quad (3)$$

or in matrix form

$$\dot{\mathbf{c}} = -(\mathbf{iH}^{\text{tot}} + \dot{\mathbf{R}} \cdot \mathbf{K}) \mathbf{c}. \quad (4)$$

Note that every component of a triplet state has its own coefficient $c_i(t)$, due to their SO energy splitting.

However, this has two disadvantages: First, the SO coupling elements are not localized like NAD couplings, contradicting the fewest switches idea. Second, the sum of transition probabilities to $2S+1$ components of the multiplets is not invariant with respect to a rotation in laboratory frame.¹⁴ As a solution to both problems, Gonzalez *et al.*^{15,16} proposed to perform a transformation from the MCH basis to eigenfunctions of H^{tot} .

Transformation from the MCH basis ϕ_j to the “diagonal basis” of H^{tot} eigenfunctions ψ_i can be written as

$$\langle \psi_j | H^{\text{tot}} | \psi_i \rangle = E_i^{\text{tot}} \delta_{ij}; \quad |\psi_i\rangle = \sum_j U_{ji} |\phi_j\rangle. \quad (5)$$

The time-dependent coefficients are then transformed to the “diagonal basis” as

$$\bar{c}_i = \sum_j U_{ji}^* c_j. \quad (6)$$

In matrix form, we can conveniently write

$$\mathbf{H}^{\text{tot}} \mathbf{U} = \mathbf{U} \bar{\mathbf{H}}^{\text{tot}} \equiv \mathbf{U} \mathbf{E}^{\text{tot}}, \quad \bar{\mathbf{c}} = \mathbf{U}^\dagger \mathbf{c}, \quad \mathbf{c} = \mathbf{U} \bar{\mathbf{c}}. \quad (7)$$

Propagation of the \bar{c} coefficients in the “diagonal basis” is then

$$\frac{d}{dt} \bar{\mathbf{c}} = \mathbf{U}^\dagger \frac{d\mathbf{c}}{dt} + \frac{d\mathbf{U}^\dagger}{dt} \mathbf{U} \bar{\mathbf{c}} = \mathbf{U}^\dagger \frac{d\mathbf{c}}{dt} - \mathbf{U}^\dagger \frac{d\mathbf{U}}{dt} \bar{\mathbf{c}}, \quad (8)$$

$$\frac{d}{dt} \bar{\mathbf{c}} = -\mathbf{U}^\dagger (\mathbf{iH}^{\text{tot}} + \dot{\mathbf{R}} \cdot \mathbf{K}) \mathbf{U} \bar{\mathbf{c}} - \mathbf{U}^\dagger \frac{d\mathbf{U}}{dt} \bar{\mathbf{c}}, \quad (9)$$

$$\frac{d}{dt} \bar{\mathbf{c}} = -(\mathbf{iE}^{\text{tot}} + \dot{\mathbf{R}} \cdot \bar{\mathbf{K}} + \mathbf{U}^\dagger \frac{d\mathbf{U}}{dt}) \bar{\mathbf{c}} \equiv \mathbf{A} \bar{\mathbf{c}}, \quad (10)$$

where $\bar{\mathbf{K}} = \mathbf{U}^\dagger \mathbf{K} \mathbf{U}$ are transformed SO couplings and we introduced the “propagator matrix,”

$$\mathbf{A} = -(\mathbf{iE}^{\text{tot}} + \dot{\mathbf{R}} \cdot \bar{\mathbf{K}} + \mathbf{U}^\dagger \frac{d\mathbf{U}}{dt}). \quad (11)$$

For a short time step Δt , when \mathbf{A} can be considered constant, the coefficients can be propagated as

$$\bar{\mathbf{c}}(t + \Delta t) = \exp[\mathbf{A} \Delta t] \bar{\mathbf{c}}(t). \quad (12)$$

The above equation contains a term $d\mathbf{U}/dt$ which can cause numerical problems due to arbitrary phases and unitary rotations among degenerate eigenvalues. Gonzalez *et al.*¹⁶ proposed to eliminate the explicit use of $d\mathbf{U}/dt$ using a “3 step propagator” technique:

1. transform $\bar{\mathbf{c}}(t) \rightarrow \mathbf{c}(t)$;
2. propagate in the MCH basis $\mathbf{c}(t) \rightarrow \mathbf{c}(t + \Delta t)$;
3. transform $\mathbf{c}(t + \Delta t) \rightarrow \bar{\mathbf{c}}(t + \Delta t)$.

The corresponding propagation equation is

$$\begin{aligned} \bar{\mathbf{c}}(t + \Delta t) &= \mathbf{U}^\dagger(t + \Delta t) \exp[-(\mathbf{iH}^{\text{tot}} + \dot{\mathbf{R}} \cdot \mathbf{K}) \Delta t] \mathbf{U}(t) \bar{\mathbf{c}}(t) \\ &\equiv \bar{\mathbf{P}}(t + \Delta t, t) \bar{\mathbf{c}}(t). \end{aligned} \quad (13)$$

Notice that Δt here must be much smaller than the nuclear trajectory propagation time step, typically 0.01 fs; the propagation is computed repeatedly and \mathbf{H}^{tot} , etc., are interpolated

between values at neighboring geometries. Note also that the transformation matrix \mathbf{U} is different in each time step and chosen to diagonalize the total Hamiltonian.

If we alleviate this condition and employ a general transformation matrix $\tilde{\mathbf{U}}$ to obtain

$$\tilde{c}_i(t) = \sum_j \tilde{U}_{ji}^*(t) c_j(t), \quad (14)$$

where the coefficients $\tilde{c}_i(t)$ may be in any representation, we can follow the same procedure as in Equations (8)–(10) to obtain

$$\frac{d}{dt} \tilde{\mathbf{c}} = -(\mathbf{i}\tilde{\mathbf{H}} + \dot{\mathbf{R}} \cdot \tilde{\mathbf{K}} + \tilde{\mathbf{U}}^\dagger \frac{d\tilde{\mathbf{U}}}{dt}) \tilde{\mathbf{c}}, \quad (15)$$

where $\tilde{\mathbf{K}} = \tilde{\mathbf{U}}^\dagger \mathbf{K} \tilde{\mathbf{U}}$ are the transformed NAD couplings and $\tilde{\mathbf{H}} = \tilde{\mathbf{U}}^\dagger \mathbf{H} \tilde{\mathbf{U}}$ is the transformed Hamiltonian (not necessarily diagonal). This equation is thus a generalization of (10) to arbitrary time-dependent basis given by the transformation matrix $\tilde{\mathbf{U}}$.

We have implemented and tested two different approaches based on this general choice of $\tilde{\mathbf{U}}$. In our first approach, we take $\tilde{\mathbf{U}}$ to be “locally constant,” i.e., the same at the beginning and at the end of the current time step. To achieve this, in each time step, we set

$$\tilde{\mathbf{U}}(t - \Delta t) = \mathbf{U}(t), \quad (16)$$

$$\tilde{\mathbf{U}}(t) = \mathbf{U}(t), \quad (17)$$

which automatically leads to

$$\frac{d\tilde{\mathbf{U}}}{dt} = 0. \quad (18)$$

At the beginning of each time step, we transform the “old” coefficients to the new basis given by $\tilde{\mathbf{U}}(t - \Delta t) = \tilde{\mathbf{U}}(t)$,

$$\begin{aligned} \tilde{\mathbf{c}}(t - \Delta t) &= \tilde{\mathbf{U}}^\dagger(t - \Delta t) \mathbf{c}(t - \Delta t) \\ &= \tilde{\mathbf{U}}^\dagger(t - \Delta t) \mathbf{U}(t - \Delta t) \bar{\mathbf{c}}(t - \Delta t) \\ &= \mathbf{U}(t)^\dagger \mathbf{U}(t - \Delta t) \bar{\mathbf{c}}(t - \Delta t) \end{aligned} \quad (19)$$

and propagate them using (15). This procedure is repeated in each time step.

The second approach consists of removal of the redundant degrees of freedom before computing the finite difference of the \mathbf{U} matrix explicitly (considering now a time step from t to $t + \Delta t$),

$$\frac{d\mathbf{U}}{dt}(t + \Delta t/2) = \frac{\mathbf{U}(t + \Delta t) - \mathbf{U}'(t)}{\Delta t} \neq \frac{\mathbf{U}(t + \Delta t) - \mathbf{U}(t)}{\Delta t}, \quad (20)$$

where the transformation $\mathbf{U}(t) \rightarrow \mathbf{U}'(t)$ aligns all phases and rotations among degenerate groups of eigenvectors to yield closest overlap with $\mathbf{U}(t)$,

$$\mathbf{S}' = \mathbf{U}'(t)^\dagger \mathbf{U}(t + \Delta t). \quad (21)$$

First, we compute the overlap

$$\mathbf{S} = \mathbf{U}(t)^\dagger \mathbf{U}(t + \Delta t) \quad (22)$$

and zero all matrix elements corresponding to non-degenerate states (threshold 0.0001 a.u.), so that \mathbf{S} becomes block-diagonal. The resulting transformation $\mathbf{U}(t) \rightarrow \mathbf{U}'(t)$ will thus affect only the redundant degrees of freedom (change of phases and mixing of degenerate states).

Then the singular value decomposition (SVD) of \mathcal{S} is computed,

$$\mathcal{S} = \mathbf{u}\mathbf{w}\mathbf{v}^\dagger. \quad (23)$$

For $\Delta t \rightarrow 0$, only redundant degrees of freedom remain and thus $\mathbf{w} \rightarrow 1$.

Using the SVD (23) and definition of the overlap (22),

$$\mathbf{u}^\dagger \mathbf{U}(t)^\dagger \mathbf{U}(t + \Delta t) \mathbf{v} = \mathbf{w} \rightarrow 1 = \mathbf{v}^\dagger \mathbf{v} \quad (24)$$

and thus

$$\mathbf{v} \mathbf{u}^\dagger \mathbf{U}(t)^\dagger \mathbf{U}(t + \Delta t) \rightarrow 1. \quad (25)$$

We define the transform $\mathbf{U}(t) \rightarrow \mathbf{U}'(t)$ by the requirement $\mathcal{S}' \rightarrow 1$ which gives the target transformation

$$\mathbf{U}'(t) = (\mathbf{v}\mathbf{u}^\dagger \mathbf{U}(t)^\dagger)^\dagger = \mathbf{U}(t)\mathbf{u}\mathbf{v}^\dagger. \quad (26)$$

The modified $\mathbf{U}'(t)$ matrix is then employed in the calculation of the finite difference (20). It is important to note, however, that the modified $\mathbf{U}'(t)$ matrix no longer diagonalizes $\mathbf{H}^{\text{tot}}(t)$; hence, it cannot be used in (10), but the more general equation (15) has to be employed, after setting the $\tilde{\mathbf{U}}$ matrices as

$$\tilde{\mathbf{U}}(t) = \mathbf{U}'(t), \quad (27)$$

$$\tilde{\mathbf{U}}(t + \Delta t) = \mathbf{U}(t + \Delta t). \quad (28)$$

Moreover, the expansion coefficients from the previous step have to be transformed to the current step as

$$\begin{aligned} \tilde{\mathbf{c}}(t) &= \tilde{\mathbf{U}}^\dagger(t) \mathbf{c}(t) \\ &= \tilde{\mathbf{U}}^\dagger(t) \mathbf{U}(t) \bar{\mathbf{c}}(t) \\ &= \mathbf{U}^\dagger(t) \mathbf{U}(t) \bar{\mathbf{c}}(t). \end{aligned} \quad (29)$$

For propagation of the nuclear trajectory, one needs the gradients of the eigenvalues E_i^{tot} of the H^{tot} matrix,

$$\nabla_R E_i^{\text{tot}} = \nabla_R \langle \psi_i | H^{\text{tot}} | \psi_i \rangle = \langle \psi_i | \nabla_R H^{\text{tot}} | \psi_i \rangle \quad (30)$$

$$\begin{aligned} &= \sum_{kl} U_{ki}^* U_{li} \langle \phi_k | \nabla_R H^{\text{tot}} | \phi_l \rangle = \sum_{kl} U_{ki}^* U_{li} \langle \phi_k | \nabla_R \\ &\quad \times (H^{\text{MCH}} + H^{\text{SO}}) | \phi_l \rangle. \end{aligned} \quad (31)$$

Since matrix elements of $\nabla_R H^{\text{SO}}$ are not available in any present program, we neglect them (which was done in the work of Gonzalez *et al.*¹⁶ as well). Then one can further simplify the gradient expression (31),

$$\begin{aligned} \langle \phi_k | \nabla_R H^{\text{MCH}} | \phi_l \rangle &= \nabla_R \langle \phi_k | H^{\text{MCH}} | \phi_l \rangle - \langle \nabla_R \phi_k | H^{\text{MCH}} | \phi_l \rangle \\ &\quad - \langle \phi_k | H^{\text{MCH}} | \nabla_R \phi_l \rangle \end{aligned} \quad (32)$$

$$\begin{aligned} &= \nabla_R \langle \phi_k | H^{\text{MCH}} | \phi_l \rangle - E_l^{\text{MCH}} \langle \nabla_R \phi_k | \phi_l \rangle \\ &\quad - E_k^{\text{MCH}} \langle \phi_k | \nabla_R \phi_l \rangle \end{aligned} \quad (33)$$

$$= \delta_{kl} \nabla_R E_k^{\text{MCH}} + (E_l^{\text{MCH}} - E_k^{\text{MCH}}) K_{kl}. \quad (34)$$

All gradients in the MCH basis as well as NAD couplings thus contribute to the final gradient in the ‘‘diagonal basis,’’

$$\nabla_R E_i^{\text{tot}} = \sum_{kl} U_{ki}^* \left[\delta_{kl} \nabla_R E_k^{\text{MCH}} + (E_l^{\text{MCH}} - E_k^{\text{MCH}}) K_{kl} \right] U_{li}. \quad (35)$$

The NAD couplings thus contribute twofold—to the \mathbf{c} propagation and to the gradients. If only time-derivative couplings are available, contribution to the gradients has to be neglected.

For the surface hopping, one also has to compute the hopping probabilities. The ‘‘classical’’ Tully’s formula when applied to the diagonal basis requires $d\mathbf{U}/dt$ explicitly; it is preferable to use the formula derived first by Granucci *et al.*⁴⁶ and also employed by Gonzalez *et al.*,¹⁶

$$\begin{aligned} p(k \rightarrow j) &= \left(\max \left\{ 1 - \frac{|\bar{c}_j(t + \Delta t)|^2}{|\bar{c}_k(t)|^2}, 0 \right\} \right) \\ &\quad \times \frac{\Re \left[\bar{c}_j(t + \Delta t) \bar{P}_{jk}^* \bar{c}_k^*(t) \right]}{|\bar{c}_k(t)|^2 - \Re \left[\bar{c}_k(t + \Delta t) \bar{P}_{kk}^* \bar{c}_k^*(t) \right]}, \end{aligned} \quad (36)$$

where \bar{P}_{jk} are matrix elements of the coefficient propagator in the diagonal basis

$$\bar{\mathbf{c}}(t + \Delta t) = \bar{\mathbf{P}}(t + \Delta t, t) \bar{\mathbf{c}}(t) \quad (37)$$

and negative $p(k \rightarrow j)$ probabilities as well as $p(k \rightarrow k)$ are set to zero.

Then the usual Tully’s stochastic hop procedure is employed: a uniform random number r from the interval $0 \leq r \leq 1$ is selected and the hop to state j is performed if

$$\sum_{i=1}^{j-1} p(k \rightarrow i) < r \leq \sum_{i=1}^j p(k \rightarrow i). \quad (38)$$

A. Treatment of the crossings of states of different multiplicities in the surface hopping dynamics

Potential energy surfaces of states with different multiplicities may freely cross in $(n - 1)$ -dimensional crossing seams. This does not cause any problems in the MCH representation where the states may be stored in constant order determined by S , M_s , and n (canonical ordering). In diagonal representation, however, the states are ordered only by energy and the coefficients of the states need to be treated within the surface hopping scheme in order to avoid unphysical, non-continuous changes in the populations.

We have implemented several methods for detection of the state crossings in the diagonal representation, which are briefly discussed here and in more detail in the [supplementary material](#). Our preferred approach is to transform the coefficients and coupling terms of the time step $t - \Delta t$ to the new basis given by $\mathbf{U}(t)$, using Equation (19) or $\tilde{\mathbf{U}}$ using Equation (29). These transformations automatically handle the swaps of states without any numerical thresholds and hence are the default choice in our implementation.

The 3-step propagator computes the time evolution of the coefficients in the MCH representation, which does not require state swapping, as long as canonical ordering is used. The state swapping is handled automatically by the 3-step process; the coefficients are first transformed to the MCH representation where the coefficients are propagated and then transformed back to the diagonal representation, possibly with a new order of the states.

B. Necessity of phase alignment in the 3-step integrator approach

On the first glance, the 3-step propagator thus does not need any phase alignment of the \mathbf{U} matrix whatsoever. This

was also claimed in Ref. 16; however, in our opinion, it is still preferable to perform the phase adjustment for the case of (almost) degenerate eigenvalues, which occurs when SO coupling is small. The eigenvectors corresponding to the degenerate eigenvalue may arbitrarily mix among themselves, which leads to random fluctuations in the populations of the components of multiplets; only the total population of the whole multiplet would remain continuous. A rigorously correct treatment of the degenerate components of multiplets would require to include spin-spin coupling, which we did not attempt; however, these non-continuous population transfers may result in unnecessary hops, which goes against the spirit of the fewest switches approach and would cause numerical problems if the derivatives of the coefficients need to be calculated.

The SHARC code actually does implement the phase alignment by default, but we believe that it needs to be generalized especially if states of higher multiplicity than triplets are involved.

In our opinion, the correct alignment procedure should take into account that in the presence of near-degeneracies the overlap $S = U(t)^\dagger U(t + \Delta t)$ is close to a block-diagonal matrix when the order of eigenvectors is the same and has a “block-permutation” form, when the order is different, rather than having diagonal or permutation matrix form.

As discussed earlier, in the 3-step propagator, the state reordering is resolved automatically. When going back to diagonal representation after propagation, the states are reordered and if the active state was reordered as well, it will most likely result in an indirectly induced hop. Lack of such induced hops actually means that normal hop would have happened if the surfaces did not cross, which should be logged and considered in the analysis. It is also possible to implement an approach where the states are not sorted by energy, but remain in their original order. This approach was also implemented to Newton-X; it does not exhibit noncontinuous changes of coefficients nor crossing-induced hops, both of which complicate analysis of the trajectories. On the other hand, the order of states may not be well defined, when the states mix, and thus it is safer to remove the discontinuities in the post-processing of the trajectories.

C. The quantum mechanics/molecular mechanics (QM/MM) approach

QM/MM, or more generally hybrid gradient, MD methods allow treating different parts of the system at different levels of theory, allowing efficient simulation of larger systems. There is a vast amount of literature reviewing these methods; especially we can refer to Refs. 47–50. Here we will briefly describe the main points of the implementation of QM/MM in Newton-X (a detailed treatment of the hybrid gradient MD in Newton-X can be found in Ref. 50).

The atoms of the whole system are divided into disjoint regions. In case of QM/MM, there are two regions: The QM region is treated with quantum chemical methods, while the MM part is described using a force field. The implementation follows the subtractive scheme, where total energies, and consequently gradients, are given by

$$E_{\text{QM/MM}}^{\text{System}} = E_{\text{QMmethod}}^{\text{QMregion}} + E_{\text{MMmethod}}^{\text{System}} - E_{\text{MMmethod}}^{\text{QMregion}}, \quad (39)$$

where the third term ensures that no interaction will be double counted.⁴⁷ The implementation allows both the electrostatic embedding (where the electrostatic interactions between the regions are included into the QM Hamiltonian via point charges) and the mechanical embedding (where the Coulomb interaction is calculated using the classical force field). For the simulations including spin-orbit coupling using the interface with Molpro, only the mechanical embedding is implemented at the moment.

III. COMPUTATIONAL DETAILS

A. Static calculations for thiophene and selenophene

We employed the state-averaged CASSCF method, using the active space of 8 electrons in 7 orbitals with three singlet and three triplet states optimized with equal weights in the state-averaging procedure. Although Stenrup³¹ states that this active space may lead to symmetry breaking problems, since it does not contain orbitals needed to describe breaking of both C–S bonds on an equal footing, in our MD simulations we did not experience these problems. During MD propagation, the molecule is never exactly symmetric and one C–S bond is always longer and weaker, and the CAS(8,7) space thus contains orbitals needed to break this particular bond. More details about the CASSCF calculations can be found in the [supplementary material](#). All the CASSCF calculations have been done using Molpro.⁴⁴

As a trade-off between accuracy and computational cost, we have selected the 6-31G* basis set. In the following, we present the justification of this choice by a comparison with other basis sets on geometry optimizations, vertical excitation energy calculations, potential energy curves, and spectra.

Geometry optimizations of the ground state have been performed using the following basis sets: 6-31G*, 6-31G[*S only] (6-31G* for S, 6-31G for the rest), TZVP, and TZVPP. The main geometry parameters are summarized in Table I. For single point calculations of vertical excitation energies and spin-orbit couplings, apart from the aforementioned basis sets, three additional basis sets have been benchmarked: AVTZ, AVQZ, and ATZVPP. The vertical excitation energies are compared in Table II.

Potential energy curves have been calculated to investigate the potential energy surfaces along the ring opening pathway;

TABLE I. Ground state optimized-geometry parameters: X stands for S or Se, distances are in Å, angles in degrees.

	Thiophene			Selenophene	
	6-31G*	TZVP	TZVPP	6-31G[*S only]	6-31G*
r(X1)	1.763	1.749	1.721	1.768	1.956
r(X1')	1.733	1.721	1.749	1.735	1.868
r(C12)	1.361	1.355	1.340	1.366	1.363
r(C1'2')	1.361	1.340	1.355	1.366	1.361
r(C22')	1.438	1.435	1.435	1.438	1.440
$\theta_1(\text{C1'XC1})$	90.874	91.035	91.043	90.886	86.431
$\theta_2(\text{XC1C2})$	111.339	111.043	112.445	111.258	109.632
$\theta_2'(\text{XC1'C2'})$	112.271	112.450	111.042	112.308	112.65
$\theta_3(\text{C1C2C2'})$	112.719	112.590	112.883	112.763	115.734
$\theta_3'(\text{C2C2'C1'})$	112.798	112.882	112.587	112.785	115.552

TABLE II. Vertical excitation energies of the spin-orbit states of thiophene in eV.

State	631G[*S only]	631G*	AVQZ	AVTZ	ATZVPP	TZVP	TZVPP
2	3.6748	3.7459	4.9072	4.9205	5.1529	4.3416	4.3385
3	3.6748	3.7459	4.9072	4.9205	5.1529	4.3416	4.3385
4	3.6748	3.7459	4.9072	4.9205	5.1529	4.3417	4.3385
5	5.0626	5.0972	4.9633	4.9786	5.2137	5.5755	5.5738
6	5.0626	5.0972	5.2288	5.2449	5.4598	5.5755	5.5738
7	5.0626	5.0972	5.2288	5.2449	5.4598	5.5755	5.5738
8	6.0840	6.1400	5.2288	5.2449	5.4598	5.9088	5.9102
9	6.0842	6.1402	5.3130	5.3275	5.5621	5.9088	5.9102
10	6.0842	6.1402	5.6034	5.6411	5.8565	5.9088	5.9102
11	6.2387	6.3211	5.6034	5.6411	5.8565	6.1058	6.1079
12	6.4441	6.4539	5.6034	5.6411	5.8565	6.1058	6.1079
13	6.4442	6.4539	5.6153	5.6562	5.9406	6.1058	6.1079
14	6.4442	6.4539	5.9648	5.9957	5.9482	6.3264	6.3279
15	6.5842	6.6197	5.9648	5.9957	5.9482	6.4143	6.4163
16	6.7256	6.7367	5.9648	5.9957	5.9482	7.0613	7.0583

these curves have been calculated by linear interpolation of internal coordinates (LIIC) procedure, interpolating between the ground state geometry: the 2^1A_1 minimum, $1^1B_1/1^1A_1$ conical intersection, and 1^1B_1 to a ring opened geometry of 1^1B_1 minimum. All these geometries were taken from Ref. 34. In total, 40 geometries were generated for the curve. The following basis sets have been tested: 6-31G, 6-31G*, 6-31G[*S only], AVDZ, ATZVP, AQZVP, TZVP, TZVPP, and TZVPP with an additional optimized Rydberg function, cc-pVTZ, and aug-cc-pVDZ and aug-cc-pVTZ. Figure 2 shows the curves obtained for the 6-31G* basis set used for the MD simulations.

Absorption spectra have been calculated using the line broadening method^{43,51} based on 500 single point calculations on geometries sampled from the Wigner distribution of the vibrational ground state. The spectrum employing the 6-31G* basis set is in sufficient qualitative agreement with the experimental spectrum and can be found in the [supplementary material](#).

B. Surface hopping dynamics

For both thiophene and selenophene, the energies, gradients, and non-adiabatic and spin-orbit couplings have been

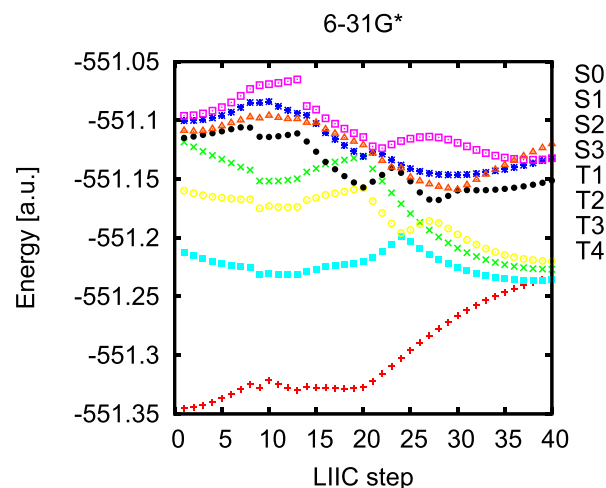


FIG. 2. LIIC curve along the ring opening pathway.

calculated on the state-averaged CASSCF level in Molpro,⁴⁴ using the active space of 8 electrons in 7 orbitals. The SO matrix elements are calculated by Molpro using an effective one-electron Fock approach as detailed in Ref. 45. The initial geometries and momenta were selected from a Wigner distribution of the quantum harmonic oscillator in the ground state.⁵² The normal modes were calculated in Turbomole⁵³ employing the def2-TZVPP basis and b3-lyp functional,⁵⁴ using the geometry optimized at the same level. The trajectories were started in the S_1 and S_2 states of these geometries. The trajectories were computed using a development version of the Newton-X code^{42,43} and the SHARC code⁵⁵ for comparison.

The time step for the dynamics simulations was 0.5 fs, while the electronic Schrödinger equation was integrated with a time step of 0.025 fs, employing the unitary propagator algorithm and using linearly interpolated Hamiltonian in the sub-steps.

For thiophene, we first computed 100 trajectories starting both in S_1 and S_2 states using singlet states only. Then four groups of 32 trajectories have been calculated for both selenophene and thiophene in the S_2 state using the 3-step approach in SHARC and three approaches in Newton-X: 3-step, explicit derivative approach using SVD, and the approach with locally constant U matrix.

The initial conditions for the hybrid gradient calculations have been prepared following a variation of the protocol suggested in Ref. 56. For the simulations in ethanol, the initial conditions from the Wigner distribution were solvated in a spherical cluster containing 500 ethanol molecules using the Packmol program.⁵⁷ The system was equilibrated at constant temperature of 298 K for 100 ps using the Tinker program,⁵⁸ with the QM part frozen. The equilibration was continued in Newton-X to further relax the spherical boundary. Before running the QM/MM trajectories, the QM atoms were supplemented with the matching Wigner distribution of velocities. For simulations of liquid thiophene and selenophene, general Amber force field (GAFF)⁵⁹ has been used and the MM energies and gradients were calculated by Gromacs.⁶⁰ The initial structures were generated similarly as for the

simulation in ethanol, but this time cubical periodic box of 300 MM molecules has been used. Four sets of 32–64 trajectories have been carried out for both thiophene and selenophene in ethanol solution and bulk liquid.

IV. RESULTS AND DISCUSSIONS

A. Assessment on model systems

We employed a simple model system proposed in Ref. 16; a one-dimensional system consisting of two harmonic oscillators coupled by a constant off-diagonal term (in atomic units),

$$\mathbf{H}^{\text{model}}(x) = \begin{pmatrix} 0.1x^2 & \xi \\ \xi & 0.1(x-2)^2 \end{pmatrix}. \quad (40)$$

The potential energy surfaces of such a system are shown in Figure 3. We investigate the change of the populations of the states during a single pass through the crossing region for various values of ξ . The population transferred should be proportional to ξ^2 according to the Landau-Zener theory.⁶¹ In Figure 3 of Ref. 16, it is shown that the 3-step integrator is superior, the approach without any phase correction fails completely, and for the 1-step approach with phase correction described in Ref. 16, very small time step is needed and even then it fails for small values of ξ .

To compare our implementation with SHARC, we realized the model as a system with two particles, one fixed at the origin and the other starting at $x = 10$ with zero initial velocity. In this way, we could run the simulation in Newton-X as well as in SHARC without any code modifications, using the input interface for potential energy surfaces in analytical form.

The comparison is shown in Figure 4. All three implementations in Newton-X exactly reproduce the populations obtained by SHARC (for the low values of ξ , the SHARC calculations are missing, because the SHARC interface allows only 6 decimal places for the value of couplings in atomic units).

To illustrate the need for phase adjustment in the 3-step approach, we extended the previously mentioned model with more states, adding an artificial multiplet consisting of four degenerate states of constant energy. These states have been assigned different starting populations, but, for simplicity, have

zero couplings with all other states. This simple model emulates a situation where there is a populated multiplet in a system with small SO coupling. If the phases of the multiplet are not controlled, even using the 3-step integrator, there can be oscillations of the populations. In SHARC implementation, the phases of the eigenvectors in the U matrix are controlled, but the procedure does not always correctly align the degenerate blocks, which leads to occasional oscillations and might lead to unexpected problems as explained in Section II. In Newton-X implementation, the degenerate blocks are aligned, and thus the population of the multiplet stays constant as shown in Figure 5.

B. Molecular dynamics of thiophene

1. Molecular dynamics without SO couplings

To investigate the effect of spin-orbit coupling on thiophene deactivation, we first investigated the dynamics on singlets only. We carried out on-the-fly surface hopping dynamics including 3 states at CAS(9,7) level, 100 trajectories starting in the S_1 state, and 100 trajectories starting in the S_2 state.

Figure 6 shows the adiabatic populations.

Only part of the trajectories that started in the S_1 state exhibit slow non-adiabatic decay, while for the trajectories starting in the S_2 state, we see ultrafast deactivation to the ground state via the S_1 state. This is in contrast with recent works^{37,38} employing a larger basis set, where the S_1 state also undergoes ultrafast decay. The $S_2(^1\pi, \pi^*)$ state first decays to the $S_1(^1\pi, \sigma^*)$ state via a first conical intersection and from the $S_1(^1\pi, \sigma^*)$ that decays to the ground state S_0 . Using 6-31G* basis the states are slightly shifted in energy and the S_1 trajectories do not have enough energy to reach the conical intersection to the $(^1\pi, \sigma^*)$ state. The potential energies averaged over the trajectories can be found in Figure S3 of the supplementary material.

The deactivation proceeds via ring opening pathway in all trajectories that reached the S_0 state. The time dependence of the C–S distance is plotted in Figure 7(a) (the dissociation is equally likely to happen for both C–S bonds, only the one that reaches the largest value during the trajectory is plotted). The CCC dihedral angles are shown in Figure 7(b) and indicate that the molecule first stays planar as the C–S bond is elongated, and then the rest of the ring opening happens out of plane.

The excited state lifetime was obtained by fitting the sum of S_2 and S_1 populations with the function $f(t) = e^{-(t-t_0)/\tau}$,

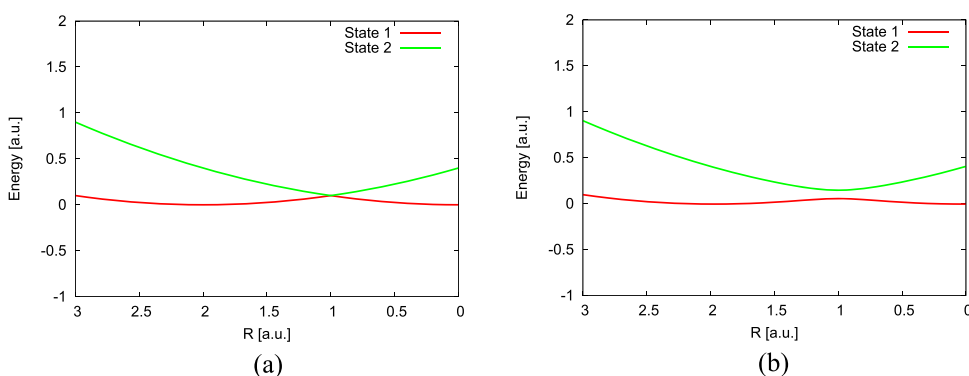


FIG. 3. Potential energy surfaces in the model system for $\xi = 0$ (a) and $\xi = 10\,000\text{ cm}^{-1}$ (b).

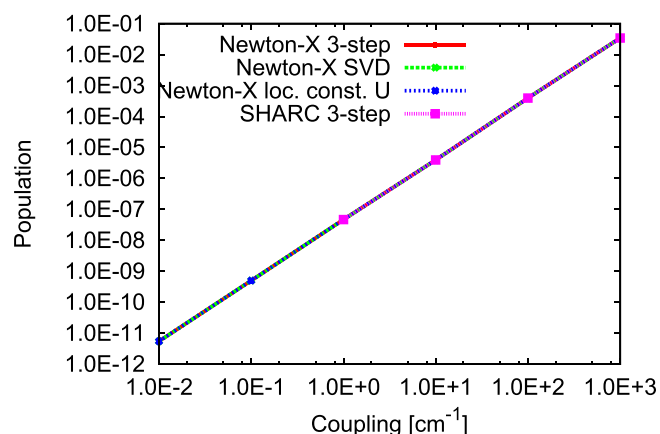


FIG. 4. Population transfer during transition of the crossing in the model system for various values of the coupling.

where t_d is the onset of the non-adiabatic events and τ is the time-constant for the exponential decay. The lifetime is obtained as $\tau + t_d$ and yields 68 fs, which is in qualitative agreement with the most recent experimental value of 80 fs²² (liquid phase) and in good agreement with the value of 73 fs obtained for the S_2 state using MD at ADC(2) level.³⁸

2. Molecular dynamics with SO couplings

We carried out surface hopping simulation of thiophene including both non-adiabatic and spin-orbit couplings. A total of 12 spin-orbit states, originating from 3 singlet and 3 triplet states, have been included in the simulations. Four sets of trajectories were calculated using (i) 3-step in Newton-X,

(ii) 3-step integrator in SHARC, (iii) explicit U derivative approach, and (iv) approach with locally constant U matrices; see Section II for more details about these methods. For each set, 32 trajectories starting in S_2 have been calculated using a subset of initial conditions used for the trajectories without spin-orbit couplings.

The evolutions of the populations of the states are given in Figure 8. It can be seen that the population of triplet states is very low, especially in the beginning of the trajectory. Although the intersystem crossing can occasionally occur ultrafast (within 100 fs), for the light elements like sulphur, it is by far not the dominant process and it can be expected that its influence on the reaction mechanism will be small. The differences among Newton-X populations are small. When same random numbers are used in the surface hopping routine, the MCH populations are exactly reproduced. The SHARC implementation also yields very similar results. The different treatment of phases normally does not influence the MCH populations. When same random numbers and same settings for the rescaling of the velocities after the hoppings are used, the codes give almost identical results, with the only minor differences being that Newton-X is calculating the spin-orbit coupling from the Cartesian components with full precision given by Molpro, while SHARC code is reading the SO matrix which is given with a fixed precision of 0.01 cm^{-1} and that Newton-X uses in the propagation quantities interpolated to the middle of the substep as opposed to the beginning of the substep, as used in SHARC.

The trajectories including the spin-orbit couplings also proceed via the ring opening mechanism virtually indistinguishable from the one in Figure 7.

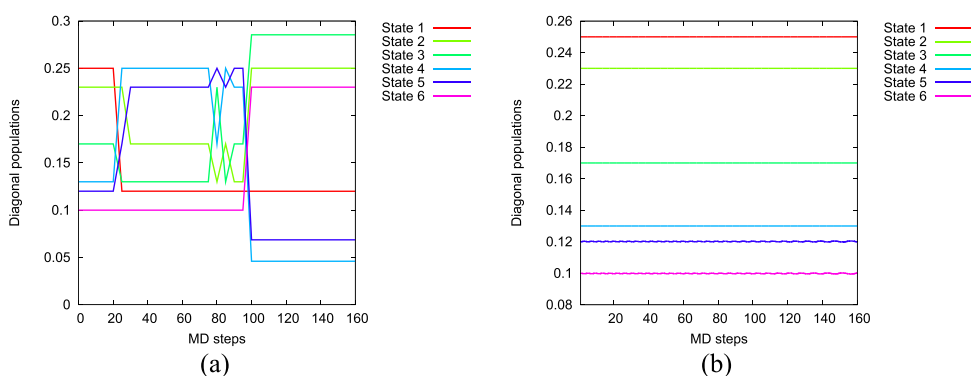


FIG. 5. Populations in the model system containing a multiplet without alignment in SHARC (a) and with alignment in Newton-X (b).

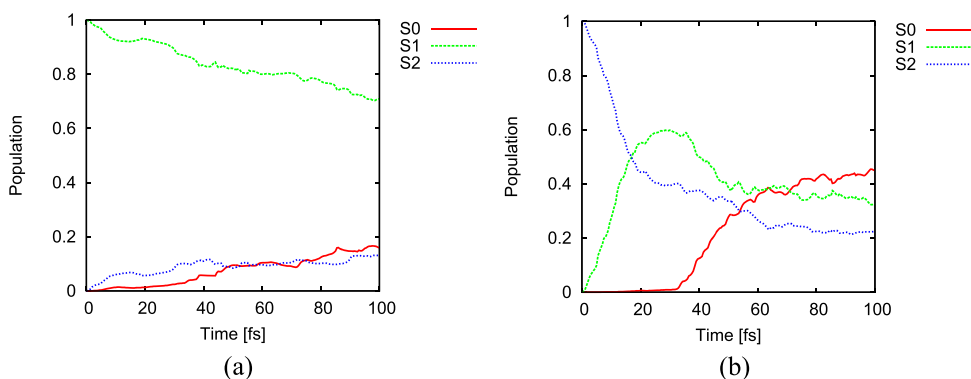


FIG. 6. Populations' evolution of average adiabatic population of trajectories starting in S_1 (a) and S_2 (b).

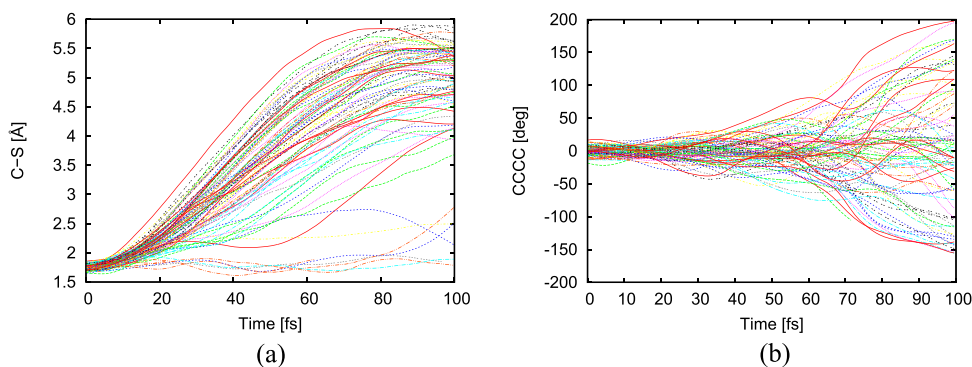


FIG. 7. Evolution of geometrical parameters describing the ring opening: C-S distance (a) and CCCC dihedral angle (b).

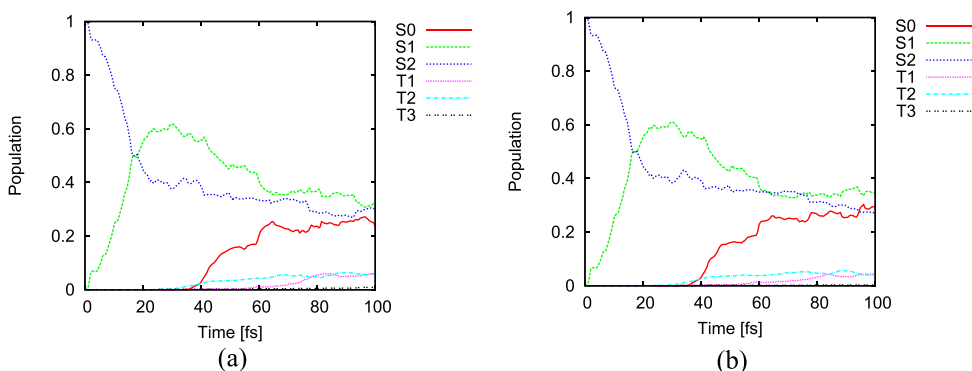


FIG. 8. Evolution of average adiabatic population of trajectories starting in the S₂ state calculated in Newton-X (a) using 3 different implementations with identical results and by 3-step integrator in SHARC (b).

Since the overall effect of spin-orbit couplings is relatively small, it is no surprise that all the implementations produce equivalent results. The excited states lifetime calculated analogously to the trajectories without spin-orbit couplings is 68 fs; there is no statistically significant difference compared to trajectories without spin-orbit coupling included.

3. QM/MM molecular dynamics with SO coupling

Interaction with the solvent may be responsible for part of the small discrepancy between theoretical and experimental lifetimes; hence, we decided to employ the QM/MM approach to incorporate the solvent into our simulations. We carried out simulations in ethanol and in bulk liquid phase, using 500 ethanol and 500 thiophene molecules in the MM region, respectively. More details about the composition of the systems and initial condition for these simulations are given in Sec. III.

The average adiabatic populations are shown in Figure 9.

The deactivation rate is slightly slower in solvent. The effective lifetime of the S₂ state deactivation is 76 fs for thiophene in ethanol, and 78 fs for simulation in liquid phase.

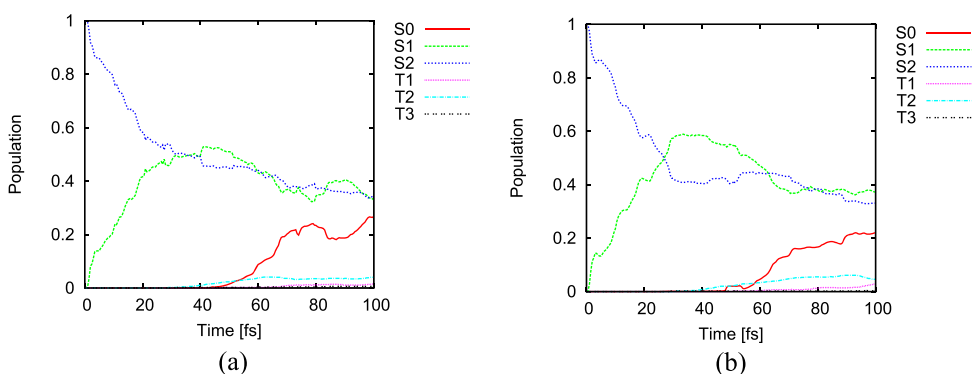


FIG. 9. Evolution of average adiabatic population of trajectories of thiophene starting in the S₂ in ethanol (a) and bulk liquid phase (b).

Incorporation of the solvent effects has brought the theoretical results closer to the experimental value of 80 fs.²²

The mechanism of the ring opening remains largely unchanged, and the out of plane motion is slightly reduced, as may be expected, as the motion of the thiophene molecule in the QM region is partially sterically hindered by the surrounding molecules.

C. Molecular dynamics of selenophene

1. Molecular dynamics with SO couplings

Substitution of sulphur by selenium was shown to lead to a higher rate of intersystem crossing in conjugated polymers;^{40,41} hence, we decided to study also the selenophene molecule using the same methodology we used for thiophene. Indeed, the obtained populations of the triplet states are considerably larger compared to thiophene, as seen in Figure 10. All three triplet states become populated, as they become almost degenerate with the single states for the ring-opened geometries. The obtained lifetime of the S₂ state is 60 fs, shorter than 68 fs obtained for thiophene.

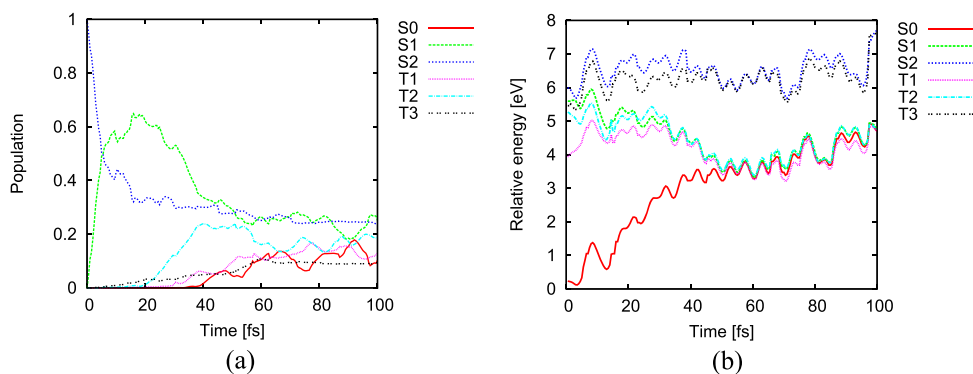


FIG. 10. Evolution of average adiabatic population for an ensemble of trajectories (a) and energies obtained for an example trajectory (b) of selenophene in the gas phase, starting in the S_2 state.

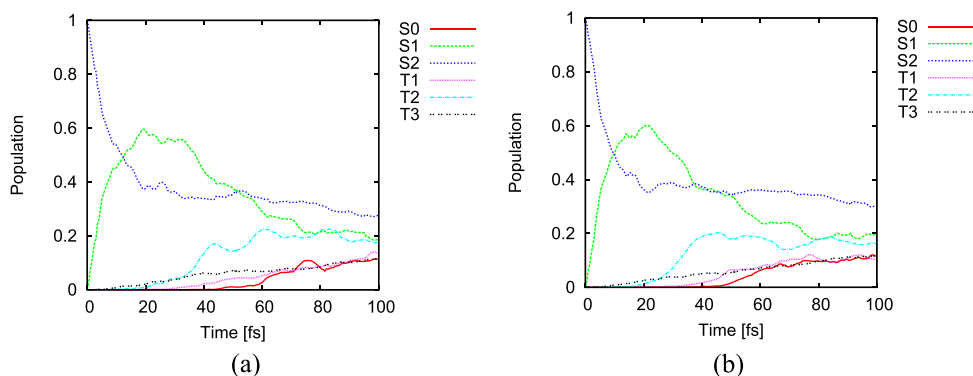


FIG. 11. Evolution of average adiabatic population of trajectories of thiophene starting in the S_2 in ethanol (a) and bulk liquid phase (b).

We observed about fivefold larger values of the SO coupling matrix elements in selenophene trajectories compared to thiophene, as illustrated in Figure S4 of the [supplementary material](#). To determine whether the larger population transfer to the triplet states is truly due to stronger spin-orbit coupling rather than due to a different electronic structure and slope of the potential energy surfaces, we carried out additional trajectories of thiophene with SO coupling matrix elements artificially scaled by a factor of five. In these trajectories, as shown in Figure S5 of the [supplementary material](#), we see similar population transfer as in selenophene. We can hence conclude that the transfer of population to the triplet states is mainly due to larger SO couplings. The mechanism of the deactivation proceeds via ring-opening pathway, very similar to the one found for thiophene shown in Figure 7. Even with larger spin-orbit coupling in selenophene, the differences between the tested methods and their implementations in SHARC and Newton-X remain negligible, as can be seen in Figure S6 of the [supplementary material](#).

2. QM/MM molecular dynamics with SO couplings

Similarly to thiophene, we have carried out QM/MM simulations for selenophene in ethanol and for bulk selenophene liquid. Figure 11 shows the average adiabatic populations. The effective lifetime of the S_2 state deactivation is 62 fs for both the ethanol solution and for the bulk liquid phase, only slightly slower than in the gas phase.

V. CONCLUSIONS

We have implemented surface hopping dynamics on surfaces resulting from the spin-orbit splitting of MCH states. Our implementation allows propagation of the coefficients both in

the representation of spin free Hamiltonian using the 3-step integrator approach as well as directly in the representation of the mixed states. The propagation in the representation of the mixed states requires calculation of the time derivative of the eigenvectors of the total Hamiltonian with the SO coupling. To this end, we have implemented two distinct approaches. The first approach uses singular value decomposition to align the phases of the eigenvectors and calculate the derivative explicitly using finite difference, and the other approach involves transformation of the basis in such a way that the eigenvectors are locally constant, forcing the derivative to be zero. To compare the various approaches, we tested them on a simple analytical model, where the implemented methods reproduced the dependence of the population transfer on coupling terms predicted by Landau-Zener theory.

For dynamics in the representation of the mixed states, it is important to properly treat the crossings of states with different multiplicities. We discuss this issue in general for various implementations of MD with SO coupling, as this topic was not addressed in sufficient detail in the previous literature. For the 3-step integrator, we have shown that phase alignment is required to prevent fluctuations in the population of degenerate states (components of triplets or higher multiplets when SO coupling is small).

We have applied these methods to deactivation of thiophene and selenophene after excitation to S_2 state in the gas phase and in liquid phase employing the QM/MM approach.

For thiophene, the effect of spin-orbit coupling is relatively small. The calculated lifetime of the S_2 state was 68 fs in the gas phase, regardless whether SO coupling is taken into account or not. The deactivation proceeds via the ring opening channel and involves an out of plane movement of the molecular chain. QM/MM simulations in the liquid phase

yield the deactivation slightly slower, as the ring-opening is slowed down by the surrounding molecules. The obtained lifetime of S_2 state deactivation is 76 fs and 78 fs for ethanol and bulk thiophene, respectively, very close to the experimental value of 80 fs.

For selenophene, the deactivation of the S_2 state is slightly faster with an effective lifetime of 60 fs in the gas phase. Even though the mechanism of the deactivation is the same as for thiophene, i.e., the ultrafast ring opening involving only the singlet states, the population of the triplet states after the ring openings rises quickly, reaching a total of about 40% after 80 fs, about three times larger than in case of thiophene, confirming that inter-system crossings may be a primary cause for lower fluorescence of polymer compounds when sulphur is substituted by selenium.

SUPPLEMENTARY MATERIAL

See [supplementary material](#) for (i) a discussion about the treatment of crossings of states of different multiplicities in various implementations of surface hopping with spin-orbit couplings, (ii) details of the CASSCF calculation, (iii) the simulated absorption spectrum, (iv) potential energy surfaces of thiophene averaged over the trajectories starting in S_1 and S_2 states, (v) evolution of the norm of the spin-orbit coupling matrix elements, (vi) populations in additional trajectories for thiophene with increased values of spin-orbit coupling, and (vii) comparison of adiabatic populations obtained using the SVD approach in Newton-X, the 3-step approach in SHARC.

ACKNOWLEDGMENTS

This work has been supported by the Czech Science Foundation (Project No. 208/12/0559) and by the Charles University in Prague (Project GA UK No. 364715).

- ¹*Modern Methods for Multidimensional Dynamics Computations in Chemistry*, edited by D. L. Thompson (World Scientific, Singapore, 1998).
- ²N. J. Turro, J. C. Scaiano, and V. Ramamurthy, *Modern Molecular Photochemistry of Organic Molecules* (University Science Books, Sausalito, 2010).
- ³M. Barbatti, *Wiley Interdiscip. Rev.: Comput. Mol. Sci.* **1**, 620 (2011).
- ⁴B. Fu, B. C. Shepler, and J. M. Bowman, *J. Am. Chem. Soc.* **133**, 7957 (2011).
- ⁵B. Han and Y. Zheng, *J. Comput. Chem.* **32**, 3520 (2011).
- ⁶E. Abrahamsson, S. Andersson, N. Marković, and G. Nyman, *J. Phys. Chem. A* **113**, 14824 (2009).
- ⁷B. Li and K.-L. Han, *J. Phys. Chem. A* **113**, 10189 (2009).
- ⁸W. Hu, G. Lendvay, B. Maiti, and G. C. Schatz, *J. Phys. Chem. A* **112**, 2093 (2008).
- ⁹T. Takayanagi, *J. Phys. Chem. A* **106**, 4914 (2002).
- ¹⁰Y. Amatatsu, K. Morokuma, and S. Yabushita, *J. Chem. Phys.* **94**, 4858 (1991).
- ¹¹B. F. E. Curchod, C. Rauer, P. Marquetand, L. Gonzalez, and T. J. Martinez, *J. Chem. Phys.* **144**, 101102 (2016).
- ¹²D. A. Fedorov, S. R. Pruitt, K. Keipert, M. S. Gordon, and S. A. Varganov, *J. Phys. Chem. A* **120**, 2911 (2016).
- ¹³R. R. Zaari and S. A. Varganov, *J. Phys. Chem. A* **119**, 1332 (2015).
- ¹⁴G. Granucci, M. Persico, and G. Spighi, *J. Chem. Phys.* **137**, 22A501 (2012).
- ¹⁵M. Richter, P. Marquetand, J. Gonzalez-Vazquez, I. Sola, and L. Gonzalez, *J. Chem. Theory Comput.* **7**, 1253 (2011).
- ¹⁶S. Mai, P. Marquetand, and L. Gonzalez, *Int. J. Quantum Chem.* **115**, 1215 (2015).
- ¹⁷I. Perepichka and D. Perepichka, *Handbook of Thiophene-Based Materials: Applications in Organic Electronics and Photonics* (Wiley, New York, 2009), Vol. 2.
- ¹⁸J. Swanston, *Ullmann's Encyclopedia of Industrial Chemistry* (Wiley-VCH Verlag GmbH & Co. KGaA, Weinheim, 2000).
- ¹⁹F. P. Hochgesang, *Chemistry of Heterocyclic Compounds* (John Wiley & Sons, Inc., New York, 2008), pp. 81–142.
- ²⁰T. Kupka, R. Wrzalik, G. Pasterna, and K. Pasterny, *J. Mol. Struct.* **616**, 17 (2002).
- ²¹H. Köppel, E. V. Gromov, and A. B. Trofimov, *Chem. Phys.* **304**, 35 (2004).
- ²²M. H. Palmer, I. C. Walker, and M. F. Guest, *Chem. Phys.* **241**, 275 (1999).
- ²³M. F. L. Serrano-Andrés, M. Merchán, and B. O. Roos, *Chem. Phys. Lett.* **211**, 125 (1993).
- ²⁴M. Kleinschmidt, J. Tatchen, and C. M. Marian, *J. Chem. Phys.* **124**, 124101 (2006).
- ²⁵S. Salzmann, M. Kleinschmidt, J. Tatchen, R. Weinkauff, and C. M. Marian, *Phys. Chem. Chem. Phys.* **10**, 380 (2008).
- ²⁶A. B. Trofimov, I. L. Zaitseva, T. E. Moskovskaya, and N. M. Vitkovskaya, *Chem. Heterocycl. Compd.* **44**, 1101 (2008).
- ²⁷J. Wan, M. Hada, M. Ehara, and H. Nakatsuji, *J. Chem. Phys.* **114**, 842 (2001).
- ²⁸R. Omidyan, M. Salehi, and Z. Heidari, *Photochem. Photobiol. Sci.* **14**, 2261 (2015).
- ²⁹D. M. P. Holland, A. B. Trofimov, E. A. Seddon, E. V. Gromov, T. Korona, N. de Oliveira, L. E. Archer, D. Joyeuxf, and L. Nahon, *Phys. Chem. Chem. Phys.* **16**, 21629 (2014).
- ³⁰M. Vinodkumar, H. Desai, and P. C. Vinodkumar, *RSC Adv.* **5**, 24564 (2015).
- ³¹M. Stenrup, *Chem. Phys.* **397**, 18 (2012).
- ³²G. Cui and W. Fang, *J. Phys. Chem. A* **115**, 11544 (2011).
- ³³N. Gavrilov, S. Salzmann, and C. M. Marian, *Chem. Phys.* **349**, 269 (2008).
- ³⁴X.-F. Wu, X. Zheng, H.-G. Wang, Y.-Y. Zhao, X. Guan, D. L. Phillips, X. Chen, and W. Fang, *J. Chem. Phys.* **133**, 134507 (2010).
- ³⁵I. Powis, I. L. Zaytseva, A. B. Trofimov, J. Schirmer, D. M. P. Holland, A. W. Potts, and L. Karlsson, *J. Phys. B: At., Mol. Opt. Phys.* **40**, 2019 (2007).
- ³⁶R. Weinkauff, L. Lehr, E. W. Schlag, S. Salzmann, and C. M. Marian, *Phys. Chem. Chem. Phys.* **10**, 393 (2008).
- ³⁷D. Fazzi, M. Barbatti, and W. Thiel, *Phys. Chem. Chem. Phys.* **17**, 7787 (2015).
- ³⁸A. Prlj, B. F. E. Curchod, and C. Corminboeuf, *Phys. Chem. Chem. Phys.* **17**, 14719 (2015).
- ³⁹M. Montalti, A. Credi, L. Prodi, and M. Gandolfi, *Handbook of Photochemistry*, 3rd ed. (CRC Press, Boca Raton, FL, 2006).
- ⁴⁰R. Acharya, S. Cekli, C. J. Zeman, R. M. Altamimi, and K. S. Schanze, *J. Phys. Chem. Lett.* **7**, 693 (2016).
- ⁴¹R. D. Pensack, Y. Song, T. M. McCormick, A. A. Jahnke, J. Hollinger, D. S. Seferos, and G. D. Scholes, *J. Phys. Chem. B* **118**, 2589 (2014).
- ⁴²M. Barbatti, G. Granucci, M. Ruckebauer, F. Plasser, R. Crespo-Otero, J. Pittner, M. Persico, and H. Lischka, NEWTON-X, A package for Newtonian dynamics close to the crossing seam, 2008–2013, <http://www.univie.ac.at/newtonx>.
- ⁴³M. Barbatti, G. Granucci, M. Persico, M. Ruckebauer, M. Vazdar, M. Eckert-Maksić, and H. Lischka, *J. Photochem. Photobiol., A* **190**, 228 (2007).
- ⁴⁴H.-J. Werner, P. J. Knowles, G. Knizia, F. R. Manby, M. Schütz, P. Celani, W. Györfy, D. Kats, T. Korona, R. Lindh, A. Mitrushenkov, G. Rauhut, K. R. Shamasundar, T. B. Adler, R. D. Amos, A. Bernhardsson, A. Berning, D. L. Cooper, M. J. O. Deegan, A. J. Dobbyn, F. Eckert, E. Goll, C. Hampel, A. Hesselmann, G. Hetzer, T. Hrenar, G. Jansen, C. Köppl, Y. Liu, A. W. Lloyd, R. A. Mata, A. J. May, S. J. McNicholas, W. Meyer, M. E. Mura, A. Nicklass, D. P. O'Neill, P. Palmieri, D. Peng, K. Pflüger, R. Pitzer, M. Reiher, T. Shiozaki, H. Stoll, A. J. Stone, R. Tarroni, T. Thorsteinsson, and M. Wang, MOLPRO, version 2015.1, a package of *ab initio* programs, 2015, see <http://www.molpro.net>.
- ⁴⁵A. Berning, M. Schweizer, H.-J. Werner, P. J. Knowles, and P. Palmieri, *Mol. Phys.* **98**, 1823 (2000).
- ⁴⁶G. Granucci, M. Persico, and A. Toniolo, *J. Chem. Phys.* **114**, 10608 (2001).
- ⁴⁷D. Bakowies and W. Thiel, *J. Phys. Chem.* **100**, 10580 (1996).
- ⁴⁸P. Sherwood, in *Modern Methods and Algorithms of Quantum Chemistry*, NIC Series Vol. 3 (John von Neumann Institute of Computing, Jülich, 2000), p. 285.
- ⁴⁹H. Lin and D. G. Truhlar, *Theor. Chem. Acc.* **117**, 185 (2006).
- ⁵⁰M. Ruckebauer, M. Barbatti, T. Mueller, and H. Lischka, *J. Phys. Chem. A* **114**, 6757 (2010).
- ⁵¹M. Barbatti, A. J. A. Aquino, and H. Lischka, *Phys. Chem. Chem. Phys.* **12**, 4959 (2010).
- ⁵²C. Ciminelli, G. Granucci, and M. Persico, *Chem. - Eur. J.* **10**, 2341 (2004).

- ⁵³TURBOMOLE V6.2 2010 A development of University of Karlsruhe and Forschungszentrum Karlsruhe GmbH, 1989-2007, TURBOMOLE GmbH, since, 2007, available from <http://www.turbomole.com>.
- ⁵⁴P. J. Stephens, F. J. Devlin, C. F. Chabalowski, and M. J. Frisch, *J. Phys. Chem.* **98**, 11623 (1994).
- ⁵⁵S. Mai, M. Richter, M. Ruckebauer, M. Oppel, P. Marquetand, and L. Gonzalez, SHARC: Surface hopping including arbitrary couplings - program package for non-adiabatic dynamics, 2014, sharc-md.org.
- ⁵⁶M. Ruckebauer, M. Barbatti, B. Sellner, T. Muller, and H. Lischka, *J. Phys. Chem. A* **114**, 12585 (2010).
- ⁵⁷L. Martínez, R. Andrade, E. G. Birgin, and J. M. Martínez, *J. Comput. Chem.* **30**, 2157 (2009).
- ⁵⁸J. W. Ponder, TINKER: Software Tools for Molecular Design, 5.0, Washington University School of Medicine, Saint Louis, MO, 2009.
- ⁵⁹J. Wang, R. Wolf, J. Caldwell, P. Kollman, and D. Case, *J. Comput. Chem.* **25**, 1157 (2004).
- ⁶⁰S. Pronk, S. Pall, R. Schulz, P. Larsson, P. Bjelkmar, R. Apostolov, M. R. Shirts, J. C. Smith, P. M. Kasson, D. van der Spoel, B. Hess, and E. Lindahl, *Bioinformatics* **29**, 845 (2013).
- ⁶¹C. Wittig, *J. Phys. Chem. B* **109**, 8428 (2005).



Contents lists available at ScienceDirect

Chemical Physics Letters

journal homepage: www.elsevier.com/locate/cplett

Fluorescence of PRODAN in water: A computational QM/MM MD study

Marek Pederzoli^a, Lukáš Sobek^a, Jiří Brabec^a, Karol Kowalski^b, Lukasz Cwiklik^{a,*}, Jiří Pittner^{a,*}^aJ. Heyrovský Institute of Physical Chemistry, Academy of Sciences of the Czech Republic, v.v.i., Dolejškova 3, 18223 Prague 8, Czech Republic^bWilliam R. Wiley Environmental Molecular Sciences Laboratory, Battelle, Pacific Northwest National Laboratory, K8-91, P.O. Box 999, Richland, WA 99352, USA

ARTICLE INFO

Article history:

Received 18 November 2013

In final form 17 February 2014

Available online 23 February 2014

ABSTRACT

Fluorescent properties of PRODAN (6-propionyl-2-dimethylaminonaphthalene) in water were studied by means of excited state molecular dynamics simulations employing a quantum mechanical and molecular mechanical approach with the time-dependent density functional theory (TD-DFT QM/MM MD). The influence of solvation on PRODAN emission was investigated within several computational schemes. The best correspondence with the experimental emission spectrum was achieved for the planar excited state PRODAN conformer in the environment of 300 explicit water molecules with polarization effects included. Hence, it is demonstrated that an extended solvent environment and polarization effects are responsible for the strong solvatochromic shift of PRODAN emission in water.

© 2014 Elsevier B.V. All rights reserved.

1. Introduction

Fluorescence spectroscopy is one of major experimental techniques employed for studying biophysical and biochemical phenomena in a wide spectrum of systems, ranging from lipid membranes to active sites of enzymes [1]. In a typical experiment, fluorescently active probe molecules or molecular fragments are introduced into a system under study. Due to the fact that fluorescent properties of probes depend on physicochemical properties of the environment, which is usually manifested as solvatochromic shifts, the probes report on changes in their vicinity. In biologically relevant systems, fluorescent probes are usually partially hydrated and probe–water interactions influence the emission spectra. This sensitivity to interactions with water can be effectively utilized. For instance, in the time-dependent fluorescence shift (TDFS) method, a time evolution of fluorescence due to water reorientation around a probe is used to gain information about the local dynamics in the nearest neighborhood of the probe [1,2]. In general, hydration of fluorescent probes cannot be neglected and must be accounted for in a theoretical description of emission processes.

PRODAN (6-propionyl-2-dimethylaminonaphthalene, see Figure 1A) and its derivatives are fluorescent probes which are known for a strong dependence of their emission spectra on the solvation state and thus they are often employed in time dependent solvent-relaxation studies, in particular in those focused on hydrated lipid membranes [3–5]. Despite the extensive use of PRODAN in fluorescent studies, its excited state properties are not fully resolved. In

particular, the geometry of the emitting state is still debated. Namely, either the planar (P-ICT) or twisted (T-ICT) intramolecular charge transfer state is suggested to be responsible for emission (see Figure 1 for the structures). The twisted excited state conformer was predicted to be fluorescently active by both experimental and theoretical studies [6–11]. However, experimental work by Abelt et al. suggested that the planar conformer is responsible for the PRODAN emission [12,13]. This view was further supported by the theoretical study of Mennucci et al. employing the time-dependent density functional theory (TD-DFT) and the symmetry-adapted cluster/configuration interaction method (SAC-CI). [14] Furthermore, it was suggested that the twisted excited state conformer is artificially stabilized by the TD-DFT method in combination with the B3LYP functional [14,15]. Hence, recent computational studies of PRODAN consider only the planar conformer of the excited state [15–18].

None of the previous computational studies of PRODAN fluorescence reproduces the extent of the solvatochromic shift in water. This issue was recently addressed in the studies of Marini et al. and Fukuda et al. employing either the TD-DFT/CAM-B3LYP or CAS-CI method with water accounted for with various solvation models [15,18]. It was concluded that the explicit solvation effects, formation of hydrogen bonds, as well as the dynamics of the probe must be taken into account to fully describe the influence of water on the emission spectrum of PRODAN. Nevertheless, no study which would include all these effects was completed so far. In our recent work, empirical force field molecular dynamics simulations were combined with the TD-DFT/B3LYP quantum chemical calculations to account for the influence of water on the emission of PRODAN [19]. The twisted excited state conformer was shown to be stable in both water and hydrated lipid membranes, and

* Corresponding authors.

E-mail addresses: lukasz.cwiklik@jh-inst.cas.cz (L. Cwiklik), jiri.pittner@jh-inst.cas.cz (J. Pittner).

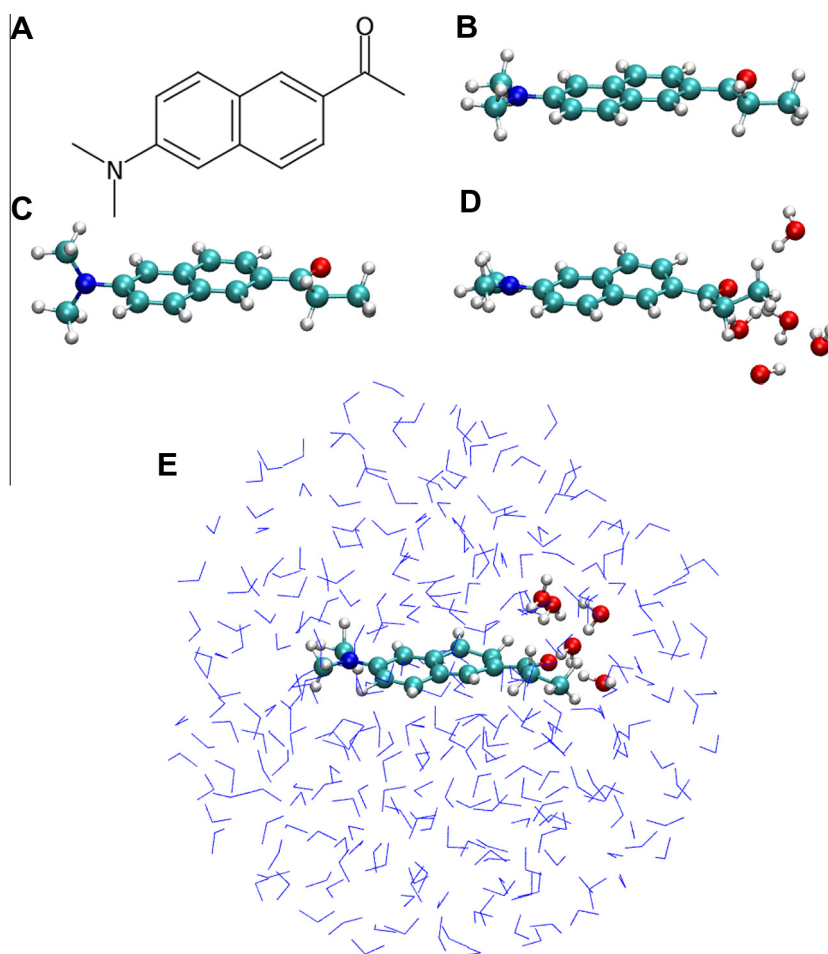


Figure 1. Molecular structure of PRODAN (A), molecule of PRODAN optimized in the S_1 state: planar conformer (B), twisted conformer (C), planar conformer with five water molecules (PRODAN + 5QM WAT) (D), planar conformer with 300 solvating water molecules (PRODAN + 300MM WAT, five water molecules which were selected for the quantum subsystem in the PRODAN + 5QM + 295 MM scheme are highlighted) (E). Color coding: carbon atoms (blue balls), hydrogen (white), oxygen (red), nitrogen (navy-blue), water molecules in MM part in (E) are depicted using a blue stick representation. (For interpretation of the references to colour in this figure legend, the reader is referred to the web version of this article.)

was suggested to contribute to the emission spectrum. The electrostatic embedding scheme that was employed in the previous study accounted for a non-continuum character of the solvent; however, both the solvent dynamics and formation of hydrogen bonds were only implicitly included.

In the present work, the influence of the water environment on PRODAN in the excited state is directly studied by means of the quantum-mechanics/molecular-mechanics scheme combined with the molecular dynamics simulations (QM/MM MD). Either PRODAN or PRODAN with several water molecules are treated by the electronic structure calculations whereas a molecular mechanics model is employed to account for an extended water environment. Molecular motion is studied by means of classical molecular dynamics with trajectories calculated based on forces from QM/MM calculations. Quantum chemistry calculations are performed employing the TD-DFT/BHLYP method [20]. To avoid the problem with artificial stabilization of the twisted charge transfer conformers, the state of the art quantum chemistry method, namely the completely renormalized equation of motion coupled cluster CR-EOM-CCSD(T), is employed to benchmark different DFT functionals [21]. The main aim of this Letter is to gain a quantitative understanding of the phenomena which are responsible for the strong solvatochromic shift in water and which seem necessary to properly interpret fluorescent spectral properties of PRODAN in biological systems.

2. Methodology

2.1. Excited state TD-DFT MD in the gas phase

Excited state molecular dynamics of PRODAN in the S_1 state was performed at the TD-DFT level of theory [20]. The BHLYP functional was employed [22]. Additionally, PBE0 and B3LYP functionals were tested [23,24]. The def2-SVP basis set was used [25], as we previously showed that this basis set combined with hybrid functionals properly accounts for absorption and emission of PRODAN [19]. Benchmark single-point calculations and geometry optimizations were performed for PRODAN in the gas phase, also the COSMO continuum solvation model was employed to approximately account for the influence of water [26].

The classical motion of nuclei in MD simulations was calculated by numerical integration of Newton's equations of motion employing the velocity Verlet algorithm with a 0.5 fs time step for the maximum simulation time of 800 fs for each conformer [27,28]. Generation of initial conditions is described in the [Supplementary Material](#). Simulations were carried out using the Newton-X software suite (version 1.2.5) [29,30]. Spectra were simulated at $T = 310$ K using the nuclear-ensemble method available in Newton-X [31]. Energies and gradients were computed on-the-fly using the Turbomole software (version 6.3) [32].

2.2. Excited state simulations in the water environment

To account for solute–solvent hydrogen bonds between carbonyl oxygen atom of PRODAN and water, TD-DFT/BHLYP MD trajectories were calculated for clusters consisting of PRODAN with five water molecules in the proximity of the carbonyl oxygen atom (in the following, we call this scheme PRODAN + 5QM WAT). The five solvent molecules were selected based on a snapshot from an equilibrated classical MD trajectory of PRODAN in water in which the PRODAN molecule was kept in the twisted geometry. The number of water molecules was chosen to be above two, which is the typical number of waters forming hydrogen bonds with the PRODAN carbonyl group (see Results). Hence, we account for a possibility of water swaps in the vicinity of carbonyl along simulated MD trajectories.

In order to take a more extended water environment into consideration, the QM/MM approach has been employed [33,34]. The system was divided into two regions: an inner quantum (QM) region containing the molecule of PRODAN and an outer classical (MM) region containing the solvent. In these calculations, 300 water molecules were considered in the classical region (which is sufficient for full solvation of PRODAN, see Figure 1E); in the following, this computational scheme is called PRODAN + 300MM WAT. Additional test calculations were performed with PRODAN and five water molecules in the proximity of the carbonyl oxygen atom of PRODAN placed the QM region, and the remaining water molecules located the MM region (PRODAN + 5QM + 295MM WAT). The QM region was treated similarly as in the gas phase calculations, i.e., the TD-DFT approach with the BHLYP functional and the def2-SVP basis set was employed for the S_1 state. To account for the presence of the solvent, the effective point charges of water molecules were included in the quantum mechanical Hamiltonian by means of the electrostatic embedding scheme [35]. Molecules of water in the MM region were described employing several sets of empirical force field parameters. The original version of the widely used SPC [36] and TIP3P [37] models are not suitable for QM/MM simulations because they were optimized for use as rigid models with fixed OH distances. Hence, in this Letter, three flexible water models are employed: SPC/Fd [38], SPC/Fw [39], and TIP3P/Fs [40]. Moreover, to include polarization effects into the QM/MM approach employed here, we developed a new computational scheme based on the polarizable AMOEBA force field [41]. Calculations were performed employing TINKER code for the classical MM region, and Turbomole software suite for the QM part of the system [32,42]. Spectra were simulated at $T = 310$ K using the nuclear-ensemble method available in Newton-X software with the in-house code added in order to account for solvent polarization effects [29,30]. Further computational details are provided in the Supplementary Material.

2.3. EOM-CC calculations

As a benchmark, vertical excitation energies for both planar and twisted PRODAN conformers optimized with the TD-DFT/BHLYP/def2-SVP method were computed using the equation-of-motion coupled cluster method with singles and doubles (EOM-CCSD) and completely renormalized EOM-CCSD with noniterative triples

(CR-EOMCCSD(T)) [21]. The basis set of Sadlej (POL1) was employed [43]. Calculations were performed with the CR-EOMCCSD(T) implementation of NWChem [44] (version 5.1) at the Chinook supercluster system at the Pacific Northwest National Laboratory.

3. Results and discussion

3.1. Comparison between DFT functionals and CR-EOM-CCSD(T)

The first singlet excited state of PRODAN (S_1) is predominantly responsible for PRODAN absorption, as shown in previous computational studies [14,15,19]. The BHLYP functional employed here also predicts the highest oscillator strength for the $S_0 \rightarrow S_1$ transition (0.25), whereas excitations to both S_2 and S_3 states are less effective (0.001 and 0.08 oscillator strengths, accordingly). The molecular conformation of PRODAN in the S_1 state is still debated and an overstabilization of the twisted conformer by various DFT functionals is the main issue. Figure 1B and C depict planar and twisted S_1 PRODAN conformers optimized in the gas phase employing the TD-DFT method with the BHLYP functional (atomic coordinates are given in the Supplementary Information). In Table 1, the relative energetic stability of the S_1 twisted conformer over the planar one calculated in the gas phase with B3LYP, PBE0, and BHLYP functionals is reported along with the results obtained with the CR-EOM-CCSD(T) method, the latter used for benchmarking the DFT functionals. In CR-EOM-CCSD(T), the planar conformer is more stable than the twisted one, with the stabilization energy equal to 14.0 kcal/mol. In both B3LYP and PBE0 the twisted conformer has a lower energy (by 7.2 and 4.5 kcal/mol, accordingly). As suggested in previous theoretical studies of PRODAN, such a stabilization of the twisted state is artificial, resulting from overstabilization of charge transfer states by some of DFT functionals [14,15]. In the case of the BHLYP functional, the planar structure of the excited state in the gas phase is significantly, by 13.0 kcal/mol, more stable than the twisted geometry, the latter being a local minimum; thus BHLYP well reproduces the relative stability of planar and twisted S_1 conformers of PRODAN and was hence chosen for examination of excited state properties of PRODAN in the present study. Note that the $S_1 \rightarrow S_0$ transition energy in the twisted state in BHLYP is relatively high, equal to 3.77 eV, and close to the $S_1 \rightarrow S_0$ energy calculated for the planar state. As an additional benchmark, we calculated $S_1 \rightarrow S_0$ energies using the three considered DFT functionals, for both twisted and planar conformers of PRODAN solvated with five water molecules; these results are presented in Table S1 in the Supplementary Material.

3.2. Emission spectra calculated in the gas phase and in the continuum solvation model

In Figure 2, emission spectra of PRODAN in the gas phase calculated with the TD-DFT/BHLYP method for the S_1 state employing molecular dynamics simulations are presented and compared with the experimental fluorescence spectrum in water. The values of vertical $S_1 \rightarrow S_0$ transition energies calculated for the optimized twisted and planar conformers are marked with bars. The twisted

Table 1

Relative stability and vertical emission energy calculated for planar and twisted conformers of PRODAN employing both TD-DFT with various functionals and the CR-EOM-CCSD(T) method. Values of oscillator strength are given in parenthesis.

	B3LYP	PBE0	BHLYP	CR-EOM-CCSD(T)
$E_{\text{twisted}} - E_{\text{planar}}$ (kcal/mol)	-7.2	-4.5	+13	+14
E (eV) $S_1 \rightarrow S_0$ planar	3.26 (0.20)	3.36 (0.20)	3.72 (0.24)	3.43
E (eV) $S_1 \rightarrow S_0$ twisted	2.35 (2.6×10^{-4})	2.51 (2.5×10^{-4})	3.77 (5.0×10^{-4})	3.58

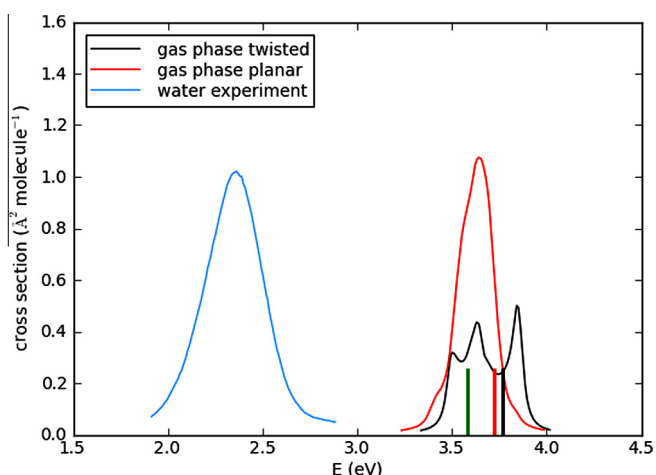


Figure 2. Fluorescence spectra of PRODAN calculated employing TD-DFT MD method in the gas phase. The experimental spectra measured in water is presented for comparison (in arbitrary units). The energy of the vertical $S_1 \rightarrow S_0$ transition calculated with the static TD-DFT method for twisted (black bar) and planar (red bar) conformers of S_1 state in the gas phase are also shown (in arbitrary units). The energy of $S_1 \rightarrow S_0$ transition calculated employing the COSMO model is shown as the green bar; in COSMO, both planar and twisted geometry have virtually the same $S_1 \rightarrow S_0$ vertical transition energy, therefore, a single bar is shown. (For interpretation of the references to colour in this figure legend, the reader is referred to the web version of this article.)

configuration of the PRODAN molecule was used as an initial structure in the MD simulation. In the initial 50 fs, the molecule stayed predominantly in the twisted configuration, then rotation of the amino group occurred and for the remaining 750 fs of the trajectory the molecule remained in the planar conformation. This process of PRODAN planarization is a consequence of the stability of the planar structure and the transient character of the twisted one. The spectra presented in Figure 2 labeled as ‘twisted’ and ‘planar’ were calculated separately for the sections of the trajectory where the PRODAN molecules was approximately twisted and planar. The emission band in both cases is located between 3.4 and 4.0 eV, with the center close to the value of 3.7 eV. No significant change in the emission energy is observed between planar and twisted configurations. Positions of both peaks corroborate with the values of vertical transitions calculated for optimized planar and twisted conformations of PRODAN (see bars in Figure 2). Regarding the intensity, the twisted spectrum is diminished with respect to the planar one; the cross section is reduced by approximately a factor of two, in accord with the reduced oscillator strength for the twisted configuration. Based on oscillation strength values along the trajectory (results not shown) we conclude that the intensity of emission is very sensitive to conformational changes, and molecular motions of the twisted conformer can enhance the $S_1 \rightarrow S_0$ transition intensity. We roughly estimate that the dynamics of PRODAN in the gas phase accounts for not more than 0.1 eV red-shift with respect to the static molecular geometry.

Gas phase spectra simulated with the BHLYP functional, for both planar and twisted conformer of PRODAN, are blue-shifted

Table 2
Properties of planar and twisted excited state conformer of PRODAN calculated both in the gas phase and using the continuum solvation COSMO model employing TD-DFT method with the BHLYP functional. In COSMO, the stabilization energy of the planar S_1 conformer over the twisted one equals to 14 kcal/mol (13 kcal/mol in the gas-phase). The $S_1 \rightarrow S_0$ transition has a $\pi \rightarrow \pi^*$ character in the planar, and an $n \rightarrow \pi^*$ character in the twisted excited state configuration.

Geometry of the S_1 state	Gas phase		COSMO	
	E $S_1 \rightarrow S_0$ (eV)	Osc. strength	E $S_1 \rightarrow S_0$ (eV)	Osc. strength
Planar	3.72	0.24	3.58	0.339
Twisted	3.77	0.0001	3.59	0.0001

by approximately 1.3 eV with respect to the experimental fluorescence spectrum measured in water (see Figure 2); similar shifts were obtained in gas phase spectra calculations employing other methods [14]. To approximately account for the influence of water, we employed the COSMO continuum solvation model. In Table 2, the results obtained with COSMO are presented (the emission energy value predicted by COSMO is also shown in Figure 2). For both planar and twisted conformers, the emission energy in COSMO is only slightly reduced with respect to that calculated in the gas phase (0.14 and 0.18 eV for the planar and the twisted case). Hence, the continuum solvation model is not able to describe the influence of the water environment on PRODAN emission. This is in accord with the previous studies where continuum solvation models are shown to reproduce about 0.2 eV of the PRODAN red shift in water [14,15].

3.3. Emission spectra calculated in explicit-water models

In the first scheme with explicit water, PRODAN + 5QM WAT, PRODAN and five water molecules were explicitly included in the electronic structure calculations. In Figure 1D, a typical snapshot of the simulated system is presented. During the 700 fs-long TD-DFT/BHLYP MD trajectory, a planarization of PRODAN occurred on the timescale below 100 fs, similar to the case of PRODAN without water. The calculated emission spectra are presented in Figure 3; the spectrum marked as ‘twisted’ was calculated in the initial section of the trajectory (the dihedral angle between the amino group and the naphthalene ring larger than 85°) while the ‘planar’ spectrum was obtained after PRODAN planarization. The emission in both cases occurs at approximately 3.5 eV. The intensity of the ‘twisted’ spectrum is reduced approximately threefold with respect to its ‘planar’ counterpart. Both spectra are red-shifted by ~ 0.2 eV while compared with the solvent-free case (see Figure 2). This red-shift is similar to that of 0.29 eV resulting from the inclusion of PRODAN–water hydrogen bonds the earlier study [15]. The presence of five water molecules in the proximity of the carbonyl oxygen atom does not, however, lead to an agreement with the experimental spectrum (~ 1.1 eV blue-shift of the calculated spectra, see the blue line in Figure 2). Note also that in the presence of explicit water molecules, the twisted S_1 state is unstable, as planarization was observed in MD simulations.

In the second computational scheme including explicit water, PRODAN + 300MM WAT, PRODAN and 300 water molecules were considered by means of the QM/MM method. In Figure 1E, a typical snapshot of the simulated system is presented. The trajectories were stable for the whole simulation time (over 1500 fs). A reduction of conformational motion of PRODAN was observed in the presence of 300 water molecules with respect to the gas phase case. Water molecules in the MM part of the system were forming up to two hydrogen bonds with the carbonyl oxygen atom of PRODAN along the trajectories. The $S_1 \rightarrow S_0$ emission spectra calculated employing the PRODAN + 300MM WAT scheme for the planar PRODAN conformer with various classical water force field employed are presented in Figure 4. The emission bands calculated employing the non-polarizable water models are located in the energy range ~ 2.6 –4.0 eV with maxima at ~ 3.35 eV, and are blue-shifted

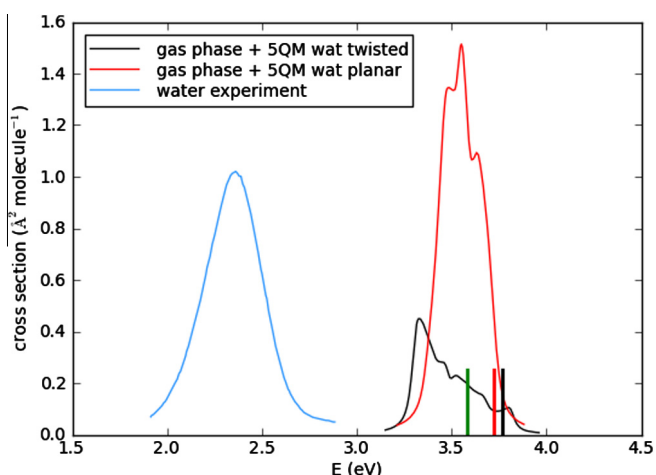


Figure 3. Fluorescence spectra of PRODAN with five water molecules in the nearest neighborhood of the carbonyl group (PRODAN + 5QM WAT) calculated employing TD-DFT MD. The experimental spectrum in water and energies of vertical transitions are shown for comparison (see the legend of Figure 2).

with respect to the experimental one by ~ 1.0 eV. To estimate the influence of implicit solvent molecules in the QM subsystem and to account for part of the polarization effects, we reassigned five waters from the MM region to the QM one in the QM/MM scheme (PRODAN + 5QM + 295MM WAT). Based on the calculated spectra (Figure S1 in the Supplementary Material), inclusion of five waters in the QM region leads to 0.1 up to 0.2 eV emission energy red shift, depending on the force field employed for MM water.

In the case of the Amoeba force field, where polarization for the whole system is included, the spectrum is located between 2.2 and 3.4 eV with the maximum at ~ 2.7 eV. Hence, polarization causes approximately 0.65 eV red-shift, and the spectrum obtained with water polarization included is blue-shifted with regard to the experimental by only ~ 0.35 eV. Note that the solvatochromic effect due to polarizability of MM water (0.65 eV) is larger than that of five QM waters (0.2 eV).

In Figure 5, emission spectra of the twisted conformer of PRODAN in water calculated employing the PRODAN + 300 MM WAT scheme with various water models are presented. The twisted PRODAN conformation was stable along the simulated trajectories suggesting that the twisted conformer is stabilized in water. The

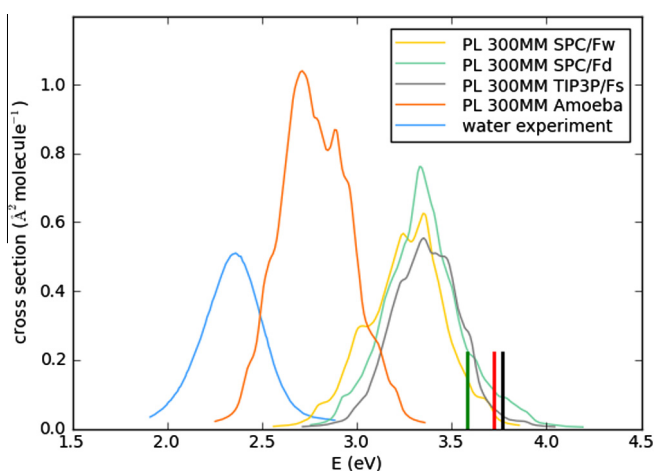


Figure 4. Fluorescence spectra of the planar conformer of PRODAN in the presence of 300 classical water molecules (PRODAN + 300MM WAT) calculated employing TD-DFT MD method in the QM/MM scheme with various classical water models. The experimental spectrum in water and energies of vertical transitions are shown for comparison (see the legend of Figure 2).

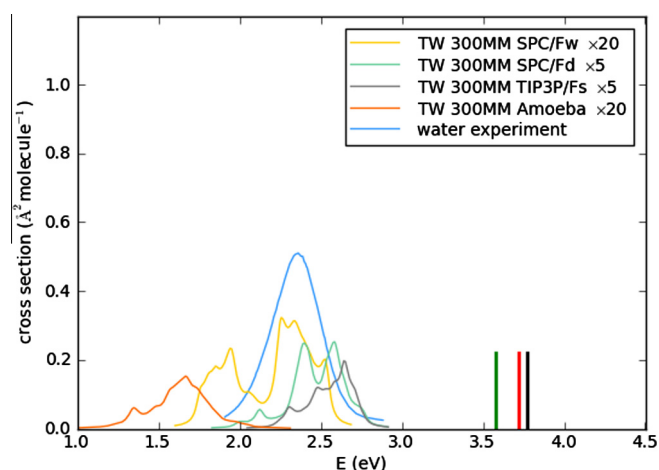


Figure 5. Fluorescence spectra of the twisted conformer of PRODAN in the presence of 300 classical water molecules (PRODAN + 300MM WAT) calculated employing TD-DFT MD method in the QM/MM scheme with various classical water models. The calculated spectra are multiplied (twentyfold or fivefold) in order to keep the same intensity scale as that in Figure 5. The experimental spectrum in water and energies of vertical transitions are shown for comparison (see the legend of Figure 2).

intensities of these spectra are significantly lower than in the case of the planar conformer. It suggests that the planar PRODAN conformation is primarily responsible for emission in water. This is further evidenced by the fact that the emission energy calculated for the twisted conformer strongly red-shifted with regard to the experiment. Namely, even though some of the spectra in Figure 5 overlap with the experimental one, it can be assumed that the one calculated employing the polarizable Amoeba model (red shifted by ~ 0.65 eV) properly accounts for solvation effects. Hence, the emission energy of the twisted conformer does not overlap with the experimental spectrum.

4. Summary and Conclusions

The influence of water on the emission spectrum of PRODAN was investigated. TD-DFT/BHLYP QM/MM simulations were employed to assess the influence of both the dynamics and explicit solvent effects on properties of the excited state of PRODAN. The state of the art CR-EOM-CCSD(T) single point calculations were used for benchmarking different DFT functionals. CR-EOM-CCSD(T) predicts that in the gas phase the planar geometry of the S_1 state of PRODAN is more stable than the twisted one. This stabilization is properly reproduced by the BHLYP functional.

Static gas phase calculations of the $S_1 \rightarrow S_0$ transition energy result in a blue-shift of ~ 1.4 eV with regard to the experiment in water for both planar and twisted S_1 conformers of PRODAN. An employment of the COSMO continuum solvation model corrects the gas phase results by only ~ 0.2 eV. Gas phase spectra calculated employing MD simulations show that the dynamics of the PRODAN molecule accounts for approximately 0.1 eV red-shift with regard to the static case, hence the gas-phase emission energies predicted by MD are blue-shifted by ~ 1.3 eV with regard to the experiment in water. In both MD and static calculations, the TD-DFT/BHLYP method predicts the twisted conformer to be unstable in the gas phase.

Earlier studies of PRODAN fluorescence suggest that in protic solvents an explicit solvation has to be considered to account for solvent effects. We demonstrate that the presence of five water molecules in the proximity of the carbonyl oxygen atom of PRODAN leads to a 0.1–0.2 eV red-shift of the emission energy with respect to the gas-phase PRODAN case with non-polarizable forcefields; but still the emission energy is 1.1 eV above the experimental one. This result was achieved by accounting for the

dynamics of both solvent and solute as well as by including the five water molecules in the quantum calculations; due to the latter, formation of solute–solvent hydrogen bonds was explicitly described at the electronic structure level. These results indicate that interactions with solvent molecules in the closest proximity of the carbonyl group do not fully explain solvent effects observed for PRODAN in water.

We accounted for an extended water environment by considering various systems consisting of a molecule of PRODAN solvated with 300 water molecules. When polarizable force-field was employed for water in these calculations, the emission band was significantly, by 1.0 eV, red-shifted with respect to the gas-phase calculations, with its maximum was located at 2.7 eV. This corroborates relatively well with the experimental value of 2.35 eV measured in water. When non-polarizable water force-field was employed, no agreement between simulated and experimental spectra was obtained. It demonstrates that solvent polarization effects are crucial for proper description of excited state PRODAN in water. We estimate that polarization effects account for ~ 0.65 eV emission blue-shift in water. Note that the importance of polarization effects in PRODAN emission was demonstrated also by Marini and co-workers but no emission spectrum was simulated in that study [15].

The strong emission red-shift observed in calculations upon inclusion of the extended explicit polarizable water environment and absent in the presence of only five water molecules or non-polarizable 300 waters can be rationalized by taking into account the changes of the electron density during the emission process. The $S_1 \rightarrow S_0$ transition alters the electron density not only in the vicinity of the carbonyl group but also in the naphthalene ring subsystem. Hence, an extended explicit and polarizable solvation environment, well above the five water molecules, is needed to fully account for the experimentally observed solvatochromic effect. It is noteworthy that the continuum solvation model is unable to account for the influence of water on PRODAN emission, in accord with previous computational studies [14,18].

The present results show that the twisted S_1 PRODAN conformer is stable in water. This confirms our earlier suggestion made for PRODAN in polar media [19]. However, the absence of direct transitions from the planar to the twisted conformation in simulated trajectories on the timescale of ~ 1500 fs suggests that such a conformational change is associated with a relatively high free-energy barrier. Moreover, the twisted conformer has low emission intensity, therefore it cannot effectively contribute to the emission spectrum in water.

Our results suggest the following photodynamic behavior of PRODAN in water. Upon excitation from the planar ground state to the planar S_1 state, the planar S_1 conformer is fluorescently active. The conformational change to the twisted state is possible as this conformation is stable in water, but such a re-configuration is relatively slow. Moreover, the intensity of the twisted state emission is relatively low. This scenario settles recent issues regarding fluorescent properties of PRODAN in water. First, it confirms that the planar S_1 conformer is predominantly active in fluorescence. Second, it supports the view that the twisted S_1 state is stable in the polar environment; however, the twisted state is fluorescently inactive. The details of PRODAN photodynamics are vital for biophysical fluorescent techniques employing PRODAN or its derivatives as fluorescent probes, as those methods are based on the influence of probe's environment on its static and dynamics spectral properties.

Acknowledgments

We acknowledge the support from Czech Science Foundation (GACR Grant No. 208/12/0559). EOMCC calculations were per-

formed using EMSL, a national scientific user facility sponsored by the Department of Energy's Office of Biological and Environmental Research and located at the Pacific Northwest National Laboratory. The Pacific Northwest National Laboratory is operated for the U.S. Department of Energy by the Battelle Memorial Institute under Contract DE-AC06.76RLO-1830.

Appendix A. Supplementary data


Supplementary data associated with this article can be found, in the online version, at <http://dx.doi.org/10.1016/j.cplett.2014.02.031>.

References

- [1] J.R. Lakowicz, *Principles of Fluorescence Spectroscopy*, Springer, New York, 2006.
- [2] P.-O. Westlund, *J. Phys. Chem. B* 104 (2000) 6059.
- [3] P. Jurkiewicz, L. Cwiklik, P. Jungwirth, M. Hof, *Biochimie* 94 (2012) 26.
- [4] G. Weber, F.J. Farris, *Biochemistry* 18 (1979) 3075.
- [5] O.A. Kucherak, P. Didier, Y. Mély, A.S. Klymchenko, *J. Phys. Chem. Lett.* 1 (2010) 616.
- [6] W. Nowak, P. Adamczak, A. Balter, A. Sygula, *J. Mol. Struct. THEOCHEM* 139 (1986) 13.
- [7] A. Balter, W. Nowak, W. Pawłkiewicz, A. Kowalczyk, *Chem. Phys. Lett.* 143 (1988) 565.
- [8] P. Ilich, F.G. Prendergast, *J. Phys. Chem.* 93 (1989) 4441.
- [9] A.B.J. Parusel, F.W. Schneider, G. Köhler, *J. Mol. Struct. THEOCHEM* 398–399 (1997) 341.
- [10] A.B.J. Parusel, W. Nowak, S. Grimme, G. Köhler, *J. Phys. Chem. A* 102 (1998) 7149.
- [11] A. Parusel, *J. Chem. Soc., Faraday Trans.* 94 (1998) 2923.
- [12] B.C. Lobo, C.J. Abelt, *J. Phys. Chem. A* 107 (2003) 10938.
- [13] B.N. Davis, C.J. Abelt, *J. Phys. Chem. A* 109 (2005) 1295.
- [14] B. Mennucci et al., *J. Phys. Chem. B* 112 (2008) 414.
- [15] A. Marini, A. Muñoz-Losa, A. Biancardi, B. Mennucci, *J. Phys. Chem. B* 114 (2010) 17128.
- [16] J. Barucha-Kraszewska, S. Kraszewski, P. Jurkiewicz, C. Ramseyer, M. Hof, *BBA-Biomembranes* 1798 (2010) 1724.
- [17] W.K. Nitschke, C.C. Vequi-Suplicy, K. Coutinho, H. Stassen, *J. Phys. Chem. B* 116 (2012) 2713.
- [18] R. Fukuda, R. Chidthong, R. Cammi, M. Ehara, *Chem. Phys. Lett.* 552 (2012) 53.
- [19] L. Cwiklik, A.J.A. Aquino, M. Vazdar, P. Jurkiewicz, J. Pittner, M. Hof, H. Lischka, *J. Phys. Chem. A* 115 (2011) 11428.
- [20] M.E. Casida, *Time-Dependent Density-Functional Response Theory for Molecules*, World Scientific, Singapore, 1995.
- [21] K. Kowalski, P. Piecuch, *J. Chem. Phys.* 120 (2004) 1715.
- [22] A.D. Becke, *J. Chem. Phys.* 98 (1993) 1372.
- [23] C. Adamo, V. Barone, *J. Chem. Phys.* 110 (1999) 6158.
- [24] A.D. Becke, *J. Chem. Phys.* 98 (1993) 5648.
- [25] A. Schäfer, H. Horn, R. Ahlrichs, *J. Chem. Phys.* 97 (1992) 2571.
- [26] A. Klamt, G. Schuurmann, *J. Chem. Soc., Perkin Trans. 2* (1993) 799.
- [27] W.C. Swope, H.C. Andersen, P.H. Berens, K.R. Wilson, *J. Chem. Phys.* 76 (1982) 637.
- [28] M. Barbatti, A.J.A. Aquino, H. Lischka, *Phys. Chem. Chem. Phys.* 12 (2010) 4959.
- [29] M. Barbatti, G. Granucci, M. Persico, M. Ruckebauer, M. Vazdar, M. Eckert-Maksić, H. Lischka, *J. Photochem. Photobiol. A* 190 (2007) 228.
- [30] M. Barbatti, G. Granucci, M. Ruckebauer, F. Plasser, J. Pittner, M. Persico, H. Lischka, *NEWTON-X: A Package for Newtonian Dynamics Close to the Crossing Seam*, Version 1.3, www.newtonx.org (2012).
- [31] R. Crespo-Otero, M. Barbatti, *Theor. Chem. Acc.* 131 (2012) 1237.
- [32] R. Ahlrichs, M. Bär, M. Häser, H. Horn, C. Kölmel, *Chem. Phys. Lett.* 162 (1989) 165.
- [33] A. Warshel, M. Levitt, *J. Mol. Biol.* 103 (1976) 227.
- [34] H.M. Senn, W. Thiel, *Angew. Chem., Int. Ed. Engl.* 48 (2009) 1198.
- [35] M. Ruckebauer, M. Barbatti, T. Müller, H. Lischka, *J. Phys. Chem. A* 114 (2010) 6757.
- [36] H.J.C. Berendsen, J.P.M. Postma, W.F. Van Gunsteren, J. Hermans, in: *Intermol. Forces*, D. Reidel Publishing Company, Dordrecht, 1981, p. 331.
- [37] W.L. Jorgensen, J. Chandrasekhar, J.D. Madura, R.W. Impey, M.L. Klein, *J. Chem. Phys.* 79 (1983) 926.
- [38] L.X. Dang, B.M. Pettitt, *J. Phys. Chem.* 91 (1987) 3349.
- [39] Y. Wu, H.L. Tepper, G.A. Voth, *J. Chem. Phys.* 124 (2006) 024503.
- [40] U.W. Schmitt, G.A. Voth, *J. Chem. Phys.* 111 (1999) 9361.
- [41] J.W. Ponder et al., *J. Chem. Phys. B* 114 (2010) 2549.
- [42] J.W. Ponder, F.M. Richards, *J. Comput. Chem.* 8 (1987) 1016.
- [43] A.J. Sadlej, *Coll. Czech CC* 53 (1988) 1995.
- [44] M. Valiev et al., *Comput. Phys. Commun.* 181 (2010) 1477.

Article

Orientation of Laurdan in Phospholipid Bilayers Influences Its Fluorescence: Quantum Mechanics and Classical Molecular Dynamics Study [†]

Mirza Wasif Baig ^{1,2} , Marek Pederzoli ^{1,2}, Piotr Jurkiewicz ¹, Lukasz Cwiklik ^{1,3} and Jiri Pittner ^{1,*}

¹ J. Heyrovský Institute of Physical Chemistry, Czech Academy of Sciences, Dolejškova 3, 18223 Prague, Czech Republic; wasifbaig.mirza@jh-inst.cas.cz (M.W.B.); marek.pederzoli@jh-inst.cas.cz (M.P.); piotr.jurkiewicz@jh-inst.cas.cz (P.J.); lukasz.cwiklik@jh-inst.cas.cz (L.C.)

² Faculty of Science, Department of Physical and Macromolecular Chemistry, Charles University in Prague, Hlavova 8, 12840 Prague, Czech Republic

³ Institute of Organic Chemistry and Biochemistry, Academy of Sciences of the Czech Republic, Flemingovonám 2, 16610 Prague, Czech Republic

* Correspondence: jiri.pittner@jh-inst.cas.cz; Tel.: +420-266052015

[†] This paper is published as part of a thematic issue of *Molecules* on “Combined Quantum Mechanical and Molecular Mechanical Methods and Simulations”.
(http://www.mdpi.com/journal/molecules/special_issues/QM)

Received: 4 June 2018; Accepted: 12 July 2018; Published: 13 July 2018



Abstract: Fluidity of lipid membranes is known to play an important role in the functioning of living organisms. The fluorescent probe Laurdan embedded in a lipid membrane is typically used to assess the fluidity state of lipid bilayers by utilizing the sensitivity of Laurdan emission to the properties of its lipid environment. In particular, Laurdan fluorescence is sensitive to gel vs liquid–crystalline phases of lipids, which is demonstrated in different emission of the dye in these two phases. Still, the exact mechanism of the environment effects on Laurdan emission is not understood. Herein, we utilize dipalmitoylphosphatidylcholine (DPPC) and dioleoylphosphatidylcholine (DOPC) lipid bilayers, which at room temperature represent gel and liquid–crystalline phases, respectively. We simulate absorption and emission spectra of Laurdan in both DOPC and DPPC bilayers with quantum chemical and classical molecular dynamics methods. We demonstrate that Laurdan is incorporated in heterogeneous fashion in both DOPC and DPPC bilayers, and that its fluorescence depends on the details of this embedding.

Keywords: fluorescence; Laurdan; DFT; TDDFT; classical molecular dynamics

1. Introduction

Fluorescence spectroscopy and fluorescence microscopy are key methods for studying phase behavior in biological lipid membranes [1]. Such a phase behavior determines mobility of membrane lipids and proteins being crucial for the functioning of living organisms. In this respect, fluorescence methods often rely on membrane fluorescent probes that report on their lipid environment. Laurdan is probably the most often used probe for the indication of lipid phase behavior [2,3]. In particular, the so-called generalized polarization method [4] is frequently used to assess the fluidity of lipid membranes based on the different behavior of Laurdan emission in dioleoylphosphatidylcholine (DOPC) and dipalmitoylphosphatidylcholine (DPPC) bilayers. Still, the details of Laurdan emission in

lipid membranes are not fully resolved. In particular, the influence of the chromophore orientation and the depth of embedding into the lipid bilayer are not understood. In contrast to the classical view, recent theoretical works suggest heterogeneous embedding of Laurdan in lipid bilayers with consequences for its spectral properties [5].

We directly address the issue of the influence of Laurdan orientation and penetration depth in DOPC and DPPC bilayers on its fluorescence. To this end we employ a combination of classical molecular dynamics (MD) and quantum chemical TD-DFT calculations. Such a multiscale approach is required to assess both the behavior of Laurdan embedded in the membrane on tens of nanosecond timescale and the emission of the excited-state dye under the influence of the membrane environment.

The manuscript is organized as follows. The methods used in both classical and quantum calculations are described and then the results are presented. First, absorption of Laurdan is analyzed in order to benchmark the computational TD-DFT methodology. Second, behavior and emission of excited state Laurdan in lipid membranes is described. All results are obtained for both DOPC (liquid-like) and DPPC (gel-like) lipid bilayers as these two systems are crucial for understanding the changes of Laurdan emission on the alteration of the state of lipid environment.

2. Results and Discussion

2.1. Ground State Absorption Spectra—Benchmarking the TD-DFT Method

Figure 1 shows the PBE0/cc-pVDZ optimized structure of Laurdan in the gas phase; the other considered methods give practically the same geometries. The molecule is planar in its ground state with the dipole moment close to 6 Debye, in agreement with earlier computational studies [6]. No significant changes of the molecular geometry employing the COSMO implicit model of solvent for water and cyclohexane with respect to the gas phase were observed. The values of the vertical absorption energies, as well as oscillator strength for Laurdan in the gas, water and cyclohexane phase computed by TD-DFT methods are presented in Tables 1–3. Overall, there is semi-quantitative agreement between all considered methods. These results are also in agreement with the values reported in earlier computational studies [6]. The magnitude of oscillatory strength demonstrates that the S_0 to S_1 transition is the most pronounced among the first four computed excitations while the excitation to the fifth state is beyond the energy range used in typical fluorescence experiments. Excited state energies computed from both functionals were compared with previously measured experimental data [7], and we found PBE0 to have the best agreement with the experiments. To additionally benchmark the performance of this functional for description of Laurdan excitation, the absorption spectra in the gas phase, cyclohexane, and water were calculated with five first excited states of Laurdan taken into account (see Figure 2) using the semiclassical method. These spectra are in good agreement with experimental absorption spectra measured at room temperature in water and cyclohexane for PRODAN which is the fluorescent probe having the same fluorophore as Laurdan [7]. Namely, the experimentally observed shoulder building up above 400 nm in the polar water environment with respect to nonpolar cyclohexane is reflected in the spectra calculated here as a shift of the spectrum toward higher wave numbers while going from gas phase through nonpolar cyclohexane to water. The results obtained from calculations with both cc-pVDZ and cc-pVTZ basis sets are appreciably similar. Hence, the cc-pVDZ basis set was chosen for further calculations.

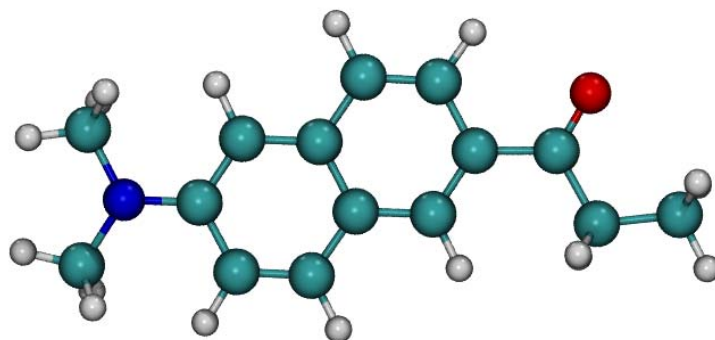


Figure 1. Optimized structure of ground state Laurdan fluorophore in the gas phase obtained using DFT PBE0/cc-pVDZ method. Color coding: Carbon–green, oxygen–red, nitrogen–blue, hydrogen–grey.

Table 1. Vertical excitation energies in eV (oscillator strengths are given in parentheses) of Laurdan in the gas phase calculated employing various TD-DFT functionals and basis sets.

Excited State	PBE0/aug-cc-pVDZ	PBE0/aug-cc-pVTZ	B3LYP/aug-cc-pVDZ	B3LYP/aug-cc-pVTZ
S ₁	3.57 (0.28)	3.57 (0.28)	3.43 (0.28)	3.44 (0.28)
S ₂	3.81 (0.48 × 10 ⁻⁴)	3.83 (0.58 × 10 ⁻⁴)	3.71 (0.33 × 10 ⁻³)	3.73 (0.52 × 10 ⁻¹)
S ₃	3.85 (0.77 × 10 ⁻¹)	3.86 (0.72 × 10 ⁻¹)	3.73 (0.55 × 10 ⁻³)	3.74 (0.56 × 10 ⁻³)
S ₄	4.47 (0.15 × 10 ⁻¹)	4.49 (0.15 × 10 ⁻¹)	4.22 (0.13 × 10 ⁻¹)	4.23 (0.13 × 10 ⁻¹)
S ₅	4.54 (0.3)	4.54 (0.31)	4.36 (0.25)	4.36 (0.26)
Excited State	PBE0/cc-pVDZ	PBE0/cc-pVTZ	B3LYP/cc-pVDZ	B3LYP/cc-pVTZ
S ₁	3.64 (0.26)	3.65 (0.27)	3.52 (0.26)	3.52 (0.27)
S ₂	3.83 (0.21 × 10 ⁻⁴)	3.86 (0.41 × 10 ⁻⁴)	3.74 (0.15 × 10 ⁻⁴)	3.78 (0.35 × 10 ⁻⁴)
S ₃	3.95 (0.62 × 10 ⁻¹)	3.94 (0.73 × 10 ⁻¹)	3.82 (0.45 × 10 ⁻¹)	3.81 (0.52 × 10 ⁻¹)
S ₄	4.65 (0.36)	4.64 (0.34)	4.48 (0.31)	4.46 (0.29)
S ₅	5.13 (0.14 × 10 ⁻³)	5.15 (0.21 × 10 ⁻³)	4.88 (0.38 × 10 ⁻⁴)	4.91 (0.26 × 10 ⁻⁴)

Table 2. Vertical excitation energies in eV (oscillator strengths are given in parentheses) of Laurdan in the water environment modeled by implicit COSMO model calculated employing various TD-DFT functionals and basis sets.

Excited State	PBE0aug-cc-pVDZ	PBE0/aug-cc-pVTZ	B3LYP/aug-cc-pVDZ	B3LYP/aug-cc-pVTZ
S ₁	3.33 (0.46)	3.34 (0.45)	3.19 (0.45)	3.21 (0.44)
S ₂	3.69 (0.89 × 10 ⁻¹)	3.70 (0.89 × 10 ⁻¹)	3.57 (0.62 × 10 ⁻¹)	3.58 (0.65 × 10 ⁻¹)
S ₃	3.96 (0.54 × 10 ⁻⁴)	3.98 (0.67 × 10 ⁻⁴)	3.88 (0.61 × 10 ⁻⁴)	3.92 (0.74 × 10 ⁻⁴)
S ₄	4.32 (0.21)	4.33 (0.23)	4.12 (0.18)	4.15 (0.20)
S ₅	4.67 (0.16 × 10 ⁻¹)	4.67 (0.15 × 10 ⁻¹)	4.43 (0.14 × 10 ⁻¹)	4.44 (0.14 × 10 ⁻¹)
Excited State	PBE0/cc-pVDZ	PBE0/cc-pVTZ	B3LYP/cc-pVDZ	B3LYP/cc-pVTZ
S ₁	3.44 (0.37)	3.44 (0.41)	3.32 (0.37)	3.31 (0.41)
S ₂	3.82 (0.10)	3.80 (0.10)	3.69 (0.73 × 10 ⁻¹)	3.68 (0.74 × 10 ⁻¹)
S ₃	3.98 (0.39 × 10 ⁻⁴)	4.04 (0.64 × 10 ⁻⁴)	3.90 (0.34 × 10 ⁻⁴)	3.97 (0.58 × 10 ⁻⁴)
S ₄	4.47 (0.29)	4.44 (0.27)	4.28 (0.24)	4.26 (0.22)
S ₅	5.11 (0.16 × 10 ⁻¹)	5.09 (0.45)	4.95 (0.27)	4.95 (0.33)

Table 3. Vertical excitation energies in eV (oscillator strengths are given in parentheses) of Laurdan in the cyclohexane environment modeled by implicit COSMO model calculated employing various TD-DFT functionals and basis sets.

Excited State	PBE0/aug-cc-pVDZ	PBE0aug-cc-pVTZ	B3LYP/aug-cc-pVDZ	B3LYP/aug-cc-pVTZ
S ₁	3.46 (0.39)	3.47 (0.39)	3.33 (0.39)	3.34 (0.39)
S ₂	3.79 (0.92 × 10 ⁻¹)	3.80 (0.88 × 10 ⁻¹)	3.67 (0.66 × 10 ⁻¹)	3.67 (0.63 × 10 ⁻¹)
S ₃	3.86 (0.58 × 10 ⁻⁴)	3.88 (0.63 × 10 ⁻⁴)	3.77 (0.52 × 10 ⁻⁴)	3.79 (0.59 × 10 ⁻⁴)
S ₄	4.44 (0.32)	4.44 (0.34)	4.26 (0.27)	4.26 (0.29)
S ₅	4.55 (0.19 × 10 ⁻¹)	4.56 (0.18 × 10 ⁻¹)	4.30 (0.16 × 10 ⁻¹)	4.32 (0.16 × 10 ⁻¹)
Excited State	PBE0/cc-pVDZ	PBE0/cc-pVTZ	B3LYP/cc-pVDZ	B3LYP/cc-pVTZ
S ₁	3.55 (0.34)	3.55 (0.36)	3.43 (0.34)	3.43 (0.37)
S ₂	3.89 (0.33 × 10 ⁻⁴)	3.89 (0.91 × 10 ⁻¹)	3.77 (0.60 × 10 ⁻¹)	3.77 (0.66 × 10 ⁻¹)
S ₃	3.90 (0.82 × 10 ⁻¹)	3.902 (0.70 × 10 ⁻⁴)	3.79 (0.52 × 10 ⁻¹)	3.84 (0.52 × 10 ⁻⁴)
S ₄	4.56 (0.40)	4.54 (0.38)	4.38 (0.34)	4.36 (0.33)
S ₅	5.15 (0.37)	5.13 (0.44)	4.95 (0.29 × 10 ⁻³)	4.98 (0.33)

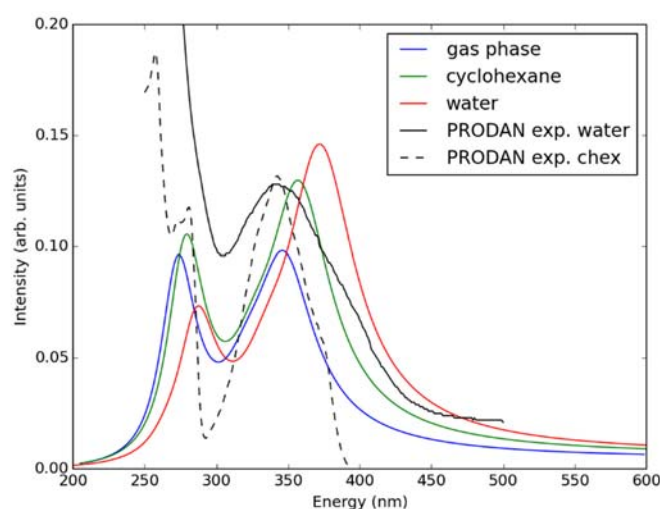


Figure 2. Simulated absorption spectra of LAURDAN in the gas phase, water, and cyclohexane using the TD-DFT/PBE0/cc-pVDZ method. Experimental spectra (taken from Ref. [7]) measured for PRODAN in water and experiment are shown for comparison.

2.2. Absorption Spectra in Lipid Bilayers

For calculation of absorption spectra, one Laurdan molecule with its complete alkyl chain incorporated in lipid bilayers was taken into account. Classical MD simulations of Laurdan in both DOPC and DPPC bilayers were performed. While the molecule of the dye stayed incorporated in the bilayers during 1000 ns-long simulations in both membranes, the details of its orientation and the depth of penetration into the lipid phase differ between DOPC and DPPC. In Figures 3 and 4, histograms of fluorophore depth and tilt angle in both bilayers are shown. The tilt angle is defined as the angle between the bilayer normal and the vector connecting carbonyl the carbon atom with the nitrogen atom in Laurdan fluorophore moiety. The tilt angle value of zero corresponds to Laurdan, the fluorophore oriented in parallel to the bilayer normal with its nitrogen atom directed toward the water phase, 90 degree corresponds to the fluorophore perpendicular to the bilayer normal, and 180 degree describes a bent fluorophore oriented parallel to bilayer normal with the nitrogen atom pointing toward membrane interior. Note that in the DPPC bilayer, which under the simulated temperature is in a gel phase, lipid tails of are on average tilted with respect to bilayer normal with the most probable value of ~15 degree (as calculated here for sn-1 acyl chains of DPPC). Penetration depth is defined as the average distance along bilayer normal between the center of mass of Laurdan and the center of mass of all phosphate atoms in lipid headgroups of the bilayer leaflet

with incorporated Laurdan molecule. The presented tilt angle and penetration results demonstrate that Laurdan penetrates significantly deeper into the gel phase DPPC bilayer and attains mostly orientations close to that of phospholipid tails (most probable tilt angle of ~ 28 degree with respect to ~ 15 degree for sn-1 chains of DPPC). This is in accord with the rigid nature of gel phase DPPC membranes where orientation of fluorophore “follows” that of lipids. In contrast, in the case of DOPC, penetration is not that deep and its distribution is wide. This can be rationalized by the less rigid nature of DOPC membrane which under the considered conditions is in the liquid disordered phase. Penetration of Laurdan and its accumulation between phospholipids is mostly the result of a competition between the overall attractive Laurdan-lipids tail–tail interactions and interactions (not necessarily attractive) between the fluorophore moiety of Laurdan and phospholipid head groups. The obtained results can be rationalized by prevalence of the tail–tail attractive forces in the case of well-ordered gel phase where Laurdan chain can easily attain conformation matching that of lipid tails. On the other hand, in the disordered phase it seems that for entropic reasons tail–tail interactions are weakened and hence Laurdan penetration is less pronounced. Notably, the fluorophore moiety in DOPC bilayer has more orientational freedom in that sense that it can more often attain orientations other than parallel to membrane normal. In particular, it can be oriented in perpendicular to the bilayer normal (90 degree tilt angle) as well as bend back toward membrane interior (tilt angle above 90 degree). This somewhat surprising reorientation of Laurdan chromophore was also observed in an earlier classical MD study [5].

In Figure 5, absorption spectra calculated using the QM/MM MD approach for Laurdan in the considered bilayers are shown together with experimental data. In the experiment, there is no significant difference between the absorption spectra measured in both lipid membranes. This is also the case in the simulated data. Note that the lower wavelength band in the calculated spectra is somewhat shifted with regard to the experiment, this is due to approximate treatment of the membrane environment. The two bands in the simulated spectra correspond to transition from $\pi \rightarrow \pi^*$ and $n \rightarrow \pi^*$ orbitals of Laurdan.

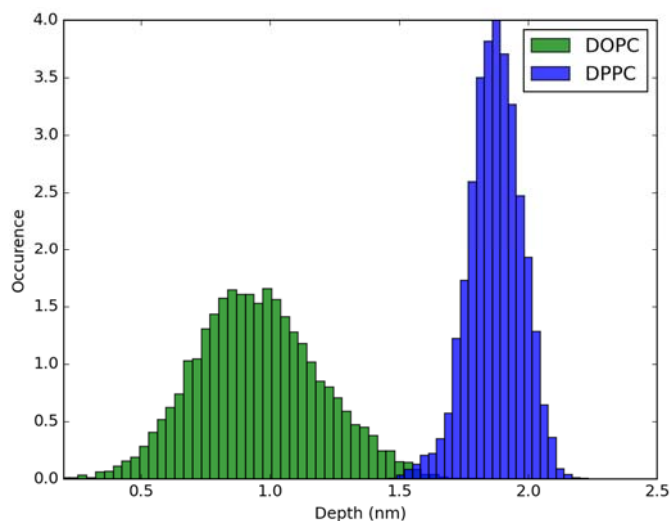


Figure 3. Histogram of penetration depth of Laurdan fluorophore in the ground state into lipid bilayers.

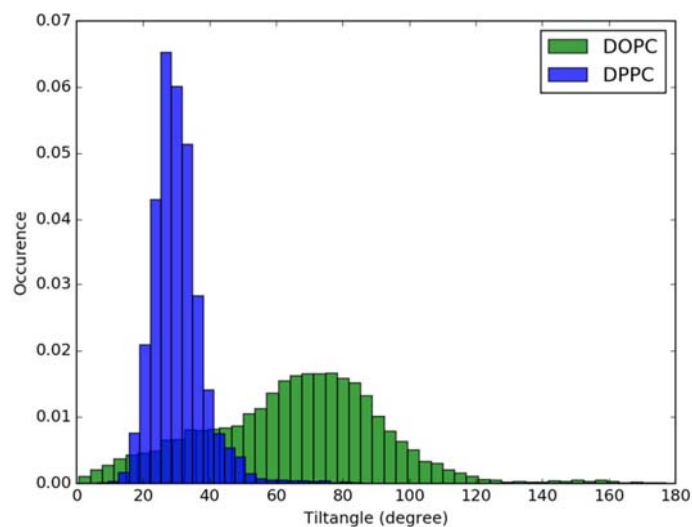


Figure 4. Histogram of tilt angle of Laurdan fluorophore in the ground state incorporated into lipid bilayers.

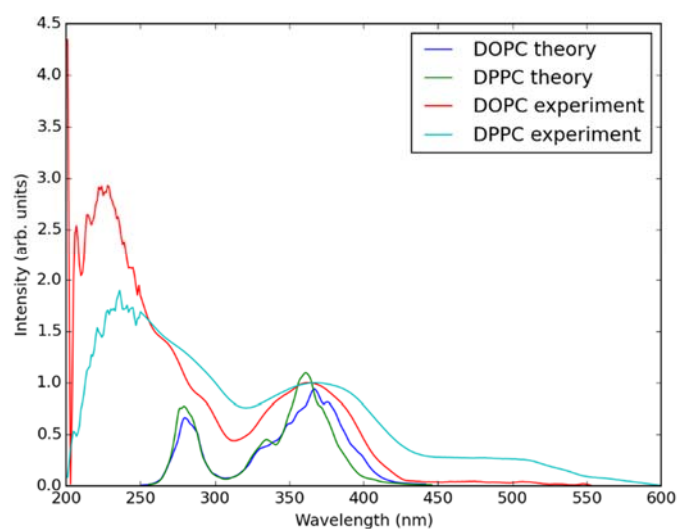


Figure 5. Simulated (using QM/MM MD approach) and experimentally measured absorption spectra of Laurdan in DOPC and DPPC bilayers.

2.3. Emission Spectra in Lipid Bilayers

Classical MD simulations of the Laurdan molecule in the S_1 state incorporated in both DOPC and DPPC bilayers were performed. While depth of membrane penetration (Figure 6) is similar to that in the ground state, the fluorophore tilt angle (Figure 7) is significantly different. Still, penetration is deeper and orientational freedom is bigger in the case of the less rigid DOPC. Notably, the tilt angle distributions, in contrast to the ground state, are bimodal for both membranes; the higher-angle orientation is however much more pronounced in the DOPC membrane. In order to simulate emission spectra in each of the membrane, short MD polarizable trajectories were calculated starting from initial points along the nonpolarizable classical MD run. Then, an electrostatic embedding approach was used taking multiple snapshots from these polarizable calculations and calculating $S_1 \rightarrow S_0$ vertical transition parameters treating Laurdan at the quantum mechanical level with water and lipids described using point charges. The resulting emission spectra, together with the experimental ones, are depicted in Figure 8. There is overall no agreement between absolute positions of experimental and calculated

spectra which can be rationalized by the lack of explicit water molecules in the electrostatic embedding approach. In our study, water was represented as point charges from classical trajectory and hence the results suffer from the lack of both explicit water polarizability and hydrogen bonding. Still, the calculated spectra allow us to make several qualitative conclusions when compared to experimental data. While calculated energy maxima overlap, there is a high-wavelength band visible in the spectrum simulated for DOPC. The occurrence of such a band can be directly related to the experimentally observed red shift of the emission spectra maxima between DPPC and DOPC. In order to assess the origin of the band, we analyzed in detail the dependence of the emission parameters on the fluorophore depth and orientation in lipid membranes. In Figures 9–12, the energy dependence on depth and tilt angle of fluorophore together with oscillator strength is shown for each of 220 single point calculations in both bilayers. Even though the high-wavelength emission components in DOPC cannot be categorically assigned to specific orientation or penetration depth, the data indicate that the high-wavelength configurations occur for deep and less tilted fluorophore. This indicates that the differences in orientation of Laurdan in the more fluid DOPC and more rigid DPPC can be responsible for differences observed in the respective emission spectra.

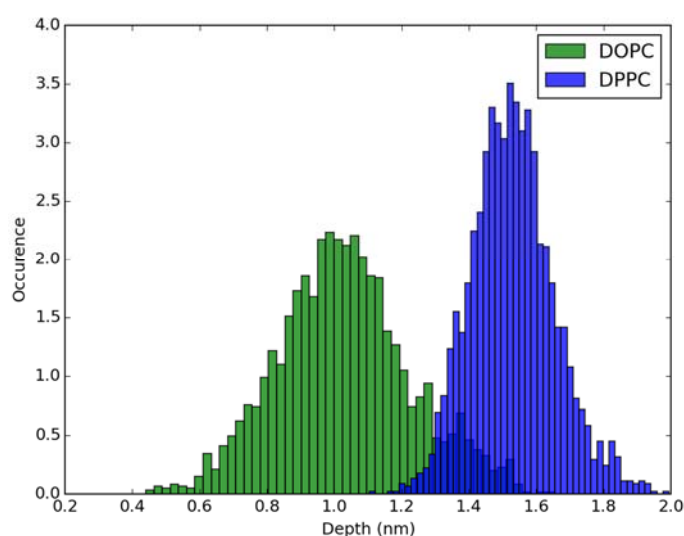


Figure 6. Histogram of penetration depth of Laurdan fluorophore in the S₁ state into lipid bilayers.

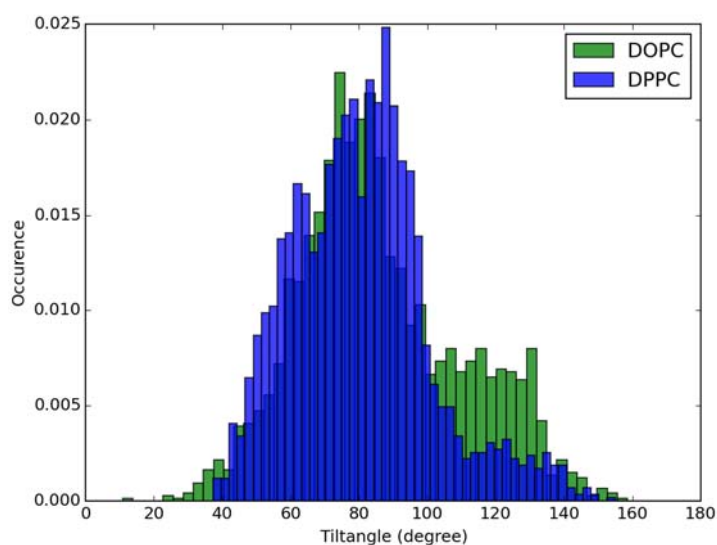


Figure 7. Histogram of tilt angle of Laurdan fluorophore in the S₁ state incorporated into lipid bilayers.

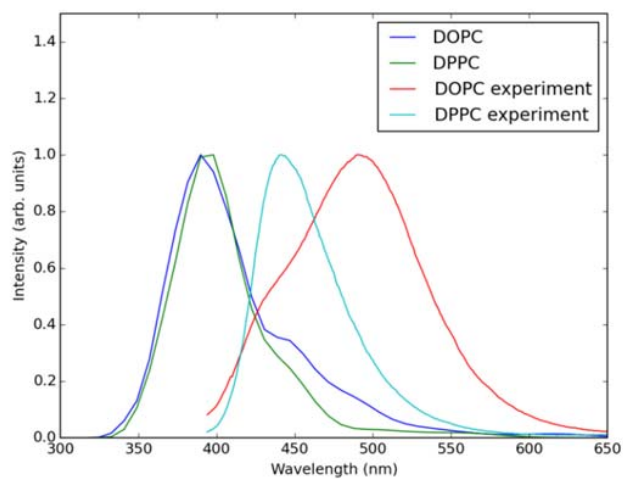


Figure 8. Simulated (using electrostatic embedding) and experimental emission spectra of S_1 to S_0 transition of Laurdan in DOPC and DPPC bilayers.

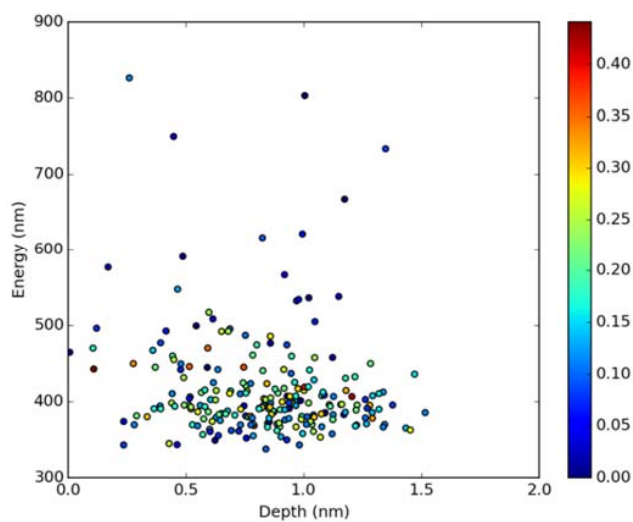


Figure 9. Emission energy vs. fluorophore depth in DOPC bilayer. Oscillatory strength is color-coded.

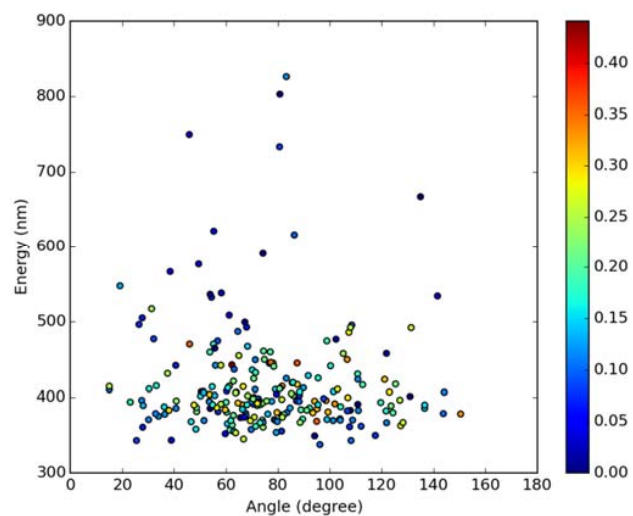


Figure 10. Emission energy vs. fluorophore tilt angle in DOPC bilayer. Oscillatory strength is color-coded.

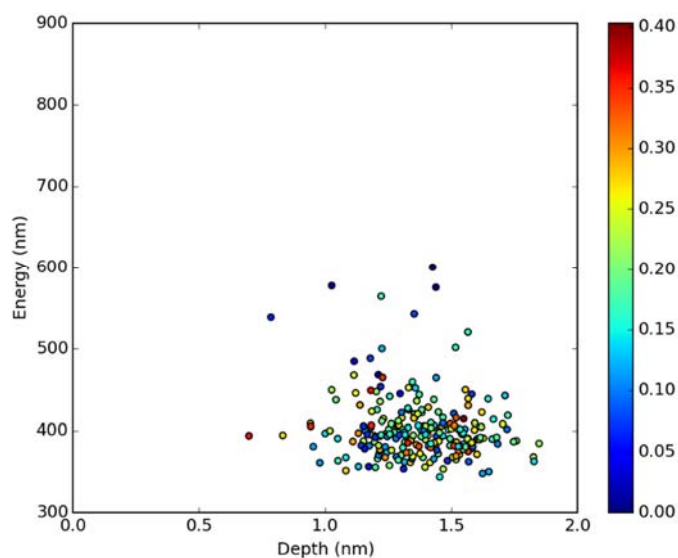


Figure 11. Emission energy vs. fluorophore depth in DPPC bilayer. Oscillatory strength is color-coded.

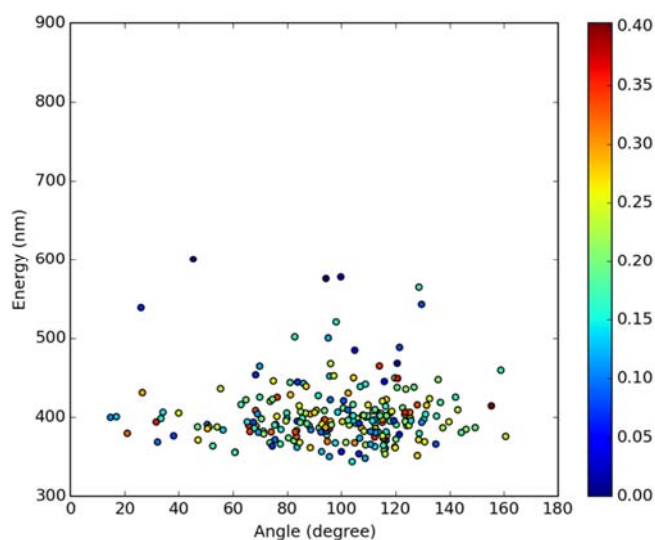


Figure 12. Emission energy vs. fluorophore tilt angle in DPPC bilayer. Oscillatory strength is color-coded.

3. Materials and Methods

3.1. Quantum Chemical Calculations

The electronic structure calculations were performed employing DFT and TD-DFT quantum chemical methods [8]. Two hybrid functionals, B3-LYP and PBE0, were chosen [9,10] with cc-pVDZ, cc-pVTZ, aug-cc-pVDZ, and aug-cc-pVTZ basis sets used [11]. Since no frontier orbitals are present on the alkyl chain of Laurdan, this chain was replaced with one methyl group to decrease computational cost. Vertical excitation energies for cc-pVDZ and cc-pVTZ basis sets are quite similar and they differ significantly with aug-cc-pVDZ and aug-cc-pVTZ only for fourth and fifth excited states. Therefore, all dynamic calculations in the manuscript are done with cc-pVDZ basis set to make them computationally cheap and feasible. Geometry of Laurdan ground and excited S_1 states in the gas phase were optimized by DFT and TD-DFT, accordingly and normal modes analysis was employed to make sure that the obtained molecular geometries are local minima. For these two structures, absorption spectra in the gas phase were computed by means of TD-DFT method using

PBE0 functional with cc-pVDZ basis set. Additionally, the COSMO continuum model of solvent was employed to model Laurdan in water and cyclohexane environments. In the continuum solvent approach, the ground state optimal structure optimized in the gas phase was used. All electronic structure calculations were performed using TURBOMOLE code [12].

3.2. Classical MD Simulations

Classical MD simulations were performed for a single Laurdan molecule incorporated in the bilayers of both DOPC and DPPC lipids. The bilayers consisted of 128 lipids (64 in each leaflet). Note that in practical biophysical applications, fluorescent dyes such as Laurdan are typically added in <1 mol% concentrations in order to minimize potential alteration of the investigated lipid bilayer. Slipids force field was used for the description of lipids together with TIP3P parameterization for water [13,14]. The empirical force field parameters for Laurdan were derived here based on the GAFF force field and employing the Antechamber code with RESP charges calculated in Gaussian software [15–17]. Overall, the force field development strategy used here for Laurdan was similar to that used for the original Slipids parameterization. The S_1 excited state force field parameters were obtained by using the ground state geometry of Laurdan with modified atomic charges. These new RESP-based charges were derived for S_1 state of Laurdan in the TD-DFT framework. Note that since the geometries of S_0 and S_1 state in Laurdan are virtually the same, the modified charge distribution using ground state geometry parameters is a reasonable approximation of force field of Laurdan in the S_1 excited state. The same approach regarding the excited state was previously used for a fluorescent dye with the same fluorophore as Laurdan [7,18]. In the case of S_1 state, water polarizability effects were additionally considered by using Drude/SWM4-NPD force field for water [19]. This is because, based on our previous study of PRODAN fluorophore, the inclusion of water polarizability is important for description of fluorescence of the moieties similar to Laurdan [7,20]. MD trajectories of 1000 nanoseconds for S_0 state of Laurdan were calculated in both DOPC and DPPC membranes with equilibration achieved within the first 50 ns and 350 ns for DOPC and DPPC respectively, as judged from stabilization of Laurdan orientation in the bilayer. For S_1 state, multiple (twenty for each membrane) trajectories of 10 ns length were calculated, starting from equidistantly chosen snapshots taken from MD trajectory of S_0 Laurdan in the corresponding lipid bilayer. Note that the lifetime of S_1 state in lipid membranes is within this timescale. Typical parameters for membrane MD simulations were employed. Namely, periodic boundary conditions were employed with semi isotropic barostat with 1 bar pressure, and thermostat with the temperature of 305 K used. The time step of 2 fs was employed for S_0 state calculation, and 1 fs for Drude model in S_1 state. The cutoff of 1.4 nm was used for van der Waals and short electrostatic interactions. Long-range electrostatics was accounted for using the PME method [21]. Calculations were performed using GROMACS software suite [22].

3.3. Simulations of Absorption and Emission Spectra in Lipid Bilayers

Absorption spectra of Laurdan in lipid DOPC and DPPC bilayers were computed by performing QM/MM MD calculations based on the classical MD trajectories. More specifically, QM/MM MD trajectories were calculated starting from individual snapshots of Laurdan embedded in the membranes obtained from classical MD simulations in equilibrium. Thirty equidistant snapshots from each bilayer MD simulation were used for further QM/MM MD calculations. These snapshots were sampling different orientations and incorporation depths of the fluorophore in the considered membranes. These classical MD snapshots served as initial coordinates for sixty QM/MM MD trajectories; from each of those trajectories several hundreds of random geometries of Laurdan molecule were generated, and for each of these a single point calculation was performed to obtain absorption cross sections using semiclassical approximation [20]. The overall absorption spectrum was then simulated assuming Lorentzian line shape with the phenomenological broadening of 0.1 eV using Newton-X software (www.newton.org). The QM/MM MD calculations were realized using an in house code which was

added to the Newton-X software suit [23] allowing for coupling quantum chemical calculations from TURBOMOLE with classical force field methods from GROMACS code [22].

Emission spectra of Laurdan in lipid bilayers were simulated employing the electrostatic embedding scheme with Laurdan treated by TD-DFT methods and the membrane and water environment accounted for by means of point charges. First, two nonpolarizable 150 ns-long classical MD simulations of S_1 Laurdan in DOPC and DPPC bilayers were performed. Each simulation was started an equilibrated snapshot taken from the previous simulation of S_0 Laurdan in the corresponding bilayer by changing the Laurdan force field from that describing S_0 state to S_1 state. Along the last 50 ns each of these two trajectories, 22 equidistant snapshots were generated, both for Laurdan in DOPC and DPPC. These snapshots served as initial geometries for 22 MD trajectories, each 2 ns-long, employing polarizable model of water; both for DOPC and DPPC. Finally, 10 snapshots were equidistantly generated between 1 and 2 ns of each polarizable trajectory; leading to 220 geometries of Laurdan embedded in the DOPC bilayer, and analogic 220 geometries for Laurdan in the DPPC bilayer. All these geometries were used for single point TD-DFT calculations of vertical $S_1 \rightarrow S_0$ transitions with Laurdan treated quantum mechanically at TD-DFT/PBE0/cc-pVDZ level, and water and lipids represented as point charges with point charges the values taken from the force field used in the classical MD trajectory. The resulting emission spectra of Laurdan in DOPC and DPPC bilayers were simulated based of vertical S_1 to S_0 transition energies and oscillator strengths assuming Lorentzian line shape with the phenomenological broadening of 0.1 eV using Newton-X software.

4. Conclusions

With all the limitations, the TD-DFT approach combined with classical MD simulations can be used for, at least, a semi-quantitative assessment of fluorescence behavior of Laurdan in the complex environment of lipid membranes. Absorption of Laurdan is not sensitive to its environment, as demonstrated in both DOPC and DPPC bilayers. This is similar to PRODAN and other similar probes, the ground state properties of which, are not influence by environment. On the other hand, emission properties of Laurdan in lipid bilayers are influenced by the fluorophore orientation and depth of membrane penetration. In contrast to a 'classical view', behavior of these two parameters for Laurdan is complex in both DOPC and DPPC. In particular, Laurdan fluorophore can not only attain conformations nearly parallel to bilayer normal but can also undergo significant conformational changes including almost complete reversal of the fluorescent moiety toward the membrane interior. Our results suggest that these heterogeneities can be responsible for the occurrence of the low-energy band of Laurdan emission in DOPC, which is crucial for understanding the methods based on Laurdan fluorescence. What is of particular importance, significant Laurdan orientational variability was demonstrated here in pure-lipid membranes. In more complicated lipid bilayers, in particular those containing cholesterol, embedded proteins and order-disorder lipid phase boundaries, orientation of Laurdan fluorophore may be further affected which suggests that the analysis of fluorescence experiments, e.g., generalized polarization, for such systems should be performed with care.

Author Contributions: M.W.B. and M.P. performed quantum calculations. P.J. supervised the project and edited the manuscript. L.C. supervised the project, performed classical simulations, and wrote the manuscript; J.P. supervised the project and edited the manuscript.

Funding: This research was funded by [Czech Science Foundation] grant number [208/12/0559] and grant number [18 26751S].

Conflicts of Interest: The authors declare no conflicts of interest.

References

1. Lakowicz, J. *Instrumentation for fluorescence spectroscopy. Principles of Fluorescence Spectroscopy*; Springer: New York, NY, USA, 1999.
2. Bagatolli, L.; Gratton, E. Two-photon fluorescence microscopy observation of shape changes at the phase transition in phospholipid giant unilamellar vesicles. *Biophys. J.* **1999**, *77*, 2090–2101. [[CrossRef](#)]

3. Simons, K.; Gerl, M.J. Revitalizing membrane rafts: New tools and insights. *Nat. Rev. Mol. Cell Biol.* **2010**, *11*, 688–699. [[CrossRef](#)] [[PubMed](#)]
4. Parasassi, T.; De Stasio, G.; Ravagnan, G.; Rusch, R.; Gratton, E. Quantitation of lipid phases in phospholipid vesicles by the generalized polarization of laurdan fluorescence. *Biophys. J.* **1991**, *60*, 179–189. [[CrossRef](#)]
5. Barucha-Kraszewska, J.; Kraszewski, S.; Ramseyer, C. Will c-laurdan dethrone laurdan in fluorescent solvent relaxation techniques for lipid membrane studies? *Langmuir* **2013**, *29*, 1174–1182. [[CrossRef](#)] [[PubMed](#)]
6. Osella, S.; Murugan, N.A.; Jena, N.K.; Knippenberg, S. Investigation into biological environments through (non) linear optics: A multiscale study of laurdan derivatives. *J. Chem. Theory Comput.* **2016**, *12*, 6169–6181. [[CrossRef](#)] [[PubMed](#)]
7. Cwiklik, L.; Aquino, A.J.A.; Vazdar, M.; Jurkiewicz, P.; Pittner, J.; Hof, M.; Lischka, H. Absorption and fluorescence of prodan in phospholipid bilayers: A combined quantum mechanics and classical molecular dynamics study. *J. Phys. Chem. A* **2011**, *115*, 11428–11437. [[CrossRef](#)] [[PubMed](#)]
8. Runge, E.; Gross, E.K. Density-functional theory for time-dependent systems. *Phys. Rev. Lett.* **1984**, *52*, 997. [[CrossRef](#)]
9. Becke, A.D. Density-functional exchange-energy approximation with correct asymptotic behavior. *Phys. Rev. A* **1988**, *38*, 3098. [[CrossRef](#)]
10. Adamo, C.; Barone, V. Toward reliable density functional methods without adjustable parameters: The pbe0 model. *J. Chem. Phys.* **1999**, *110*, 6158–6170. [[CrossRef](#)]
11. Kendall, R.A.; Dunning, T.H., Jr.; Harrison, R.J. Electron affinities of the first-row atoms revisited. Systematic basis sets and wave functions. *J. Chem. Phys.* **1992**, *96*, 6796–6806. [[CrossRef](#)]
12. Ahlrichs, R.; Bär, M.; Häser, M.; Horn, H.; Kölmel, C. Electronic structure calculations on workstation computers: The program system turbomole. *Chem. Phys. Lett.* **1989**, *162*, 165–169. [[CrossRef](#)]
13. Jambeck, J.P.; Lyubartsev, A.P. Derivation and systematic validation of a refined all-atom force field for phosphatidylcholine lipids. *J. Phys. Chem. B* **2012**, *116*, 3164–3179. [[CrossRef](#)] [[PubMed](#)]
14. Vega, C.; de Miguel, E. Surface tension of the most popular models of water by using the test-area simulation method. *J. Chem. Phys.* **2007**, *126*, 154707. [[CrossRef](#)] [[PubMed](#)]
15. Wang, J.; Wang, W.; Kollman, P.A.; Case, D.A. Antechamber: An accessory software package for molecular mechanical calculations. *J. Am. Chem. Soc.* **2001**, *222*, U403.
16. Wang, J.M.; Wolf, R.M.; Caldwell, J.W.; Kollman, P.A.; Case, D.A. Development and testing of a general amber force field (vol 25, pg 1157, 2004). *J. Comput. Chem.* **2005**, *26*, 1157–1174.
17. Frisch, M.; Trucks, G.; Schlegel, H.B.; Scuseria, G.; Robb, M.; Cheeseman, J.; Scalmani, G.; Barone, V.; Mennucci, B.; Petersson, G. *Gaussian 09, Revision A. 02*; Gaussian Inc.: Wallingford, CT, USA, 2009.
18. Barucha-Kraszewska, J.; Kraszewski, S.; Jurkiewicz, P.; Ramseyer, C.; Hof, M. Numerical studies of the membrane fluorescent dyes dynamics in ground and excited states. *Biochim. Biophys. Acta-Biomembr.* **2010**, *1798*, 1724–1734. [[CrossRef](#)] [[PubMed](#)]
19. Lamoureux, G.; Harder, E.; Vorobyov, I.V.; Roux, B.; MacKerell, A.D. A polarizable model of water for molecular dynamics simulations of biomolecules. *Chem. Phys. Lett.* **2006**, *418*, 245–249. [[CrossRef](#)]
20. Pederzoli, M.; Sobek, L.; Brabec, J.; Kowalski, K.; Cwiklik, L.; Pittner, J. Fluorescence of prodan in water: A computational qm/mm md study. *Chem. Phys. Lett.* **2014**, *597*, 57–62. [[CrossRef](#)]
21. Essmann, U.; Perera, L.; Berkowitz, M.L.; Darden, T.; Lee, H.; Pedersen, L.G. A smooth particle mesh ewald method. *J. Chem. Phys.* **1995**, *103*, 8577–8593. [[CrossRef](#)]
22. Hess, B.; Kutzner, C.; van der Spoel, D.; Lindahl, E. Gromacs 4: Algorithms for highly efficient, load-balanced, and scalable molecular simulation. *J. Chem. Theory Comput.* **2008**, *4*, 435–447. [[CrossRef](#)] [[PubMed](#)]
23. Barbatti, M.; Ruckebauer, M.; Plasser, F.; Pittner, J.; Granucci, G.; Persico, M.; Lischka, H. Newton-x: A surface-hopping program for nonadiabatic molecular dynamics. *Rev. Comput. Mol. Sci.* **2014**, *4*, 26–33. [[CrossRef](#)]

Sample Availability: Samples of the compounds are not available from the authors.



© 2018 by the authors. Licensee MDPI, Basel, Switzerland. This article is an open access article distributed under the terms and conditions of the Creative Commons Attribution (CC BY) license (<http://creativecommons.org/licenses/by/4.0/>).